

**Modeling and Sensitivity/Uncertainty Analyses of ZED-2
Benchmark Experiments Using DRAGON, DONJON & SUS3D**

MODELING AND SENSITIVITY/UNCERTAINTY ANALYSES
OF ZED-2 BENCHMARK EXPERIMENTS USING DRAGON,
DONJON & SUS3D

BY
SHAHAB DABIRAN, B.Sc

A THESIS SUBMITTED
TO THE DEPARTMENT OF ENGINEERING PHYSICS
OF McMASTER UNIVERSITY IN PARTIAL FULFILMENT OF THE
REQUIREMENTS FOR THE DEGREE OF
MASTERS OF APPLIED SCIENCE
SEPTEMBER 2011

Master of Applied Science (2011)
(Engineering Physics)

McMaster University
Hamilton, ON

TITLE: Modeling and Sensitivity/Uncertainty Analyses of
ZED-2 Benchmark Experiments Using DRAGON,
DONJON& SUS3D

AUTHOR: Shahab Dabiran
Bachelor of Science in Honor Specialization in Chemistry
University of Western Ontario, Toronto, Canada

SUPERVISOR: Dr. Adriaan Buijs

NUMBER OF PAGES: x, 103

Abstract

Due to the strong interest in thorium fuels in CANDU reactors rooting back to 1970's and 1980's [1], four experiments were done in the ZED-2 critical facility at Chalk River Laboratories to test the properties of (Th,Pu)O₂ fuel [2]. The fuel was placed in five bundles with a typical CANDU design, stacked vertically in the center of the core (K0 site) and surrounded by natural uranium fuel.

The simulation of these experiments using the transport code DRAGON coupled with the diffusion code DONJON is presented. DRAGON is initially used to model two lattices and the full cores in 2D. These models are designed to calculate direct/adjoint flux, k_{∞} and k_{eff} values using the collision probability method. Furthermore, the models determine a set of homogenized and condensed cross sections in two energy groups. Subsequently, DONJON is used to model the full core facility in three dimensions. Using the homogenized and condensed macroscopic cross section libraries obtained from the DRAGON models, DONJON is able to calculate the flux alongside with the k_{eff} values for the specific cases in two energy groups. The results are then compared to those from the experiments and will further validate the accuracy of the simulations.

Sensitivity and uncertainty results for the infinite lattices and the 2D full core model using DRAGON and SUS3D code are discussed. The direct and adjoint flux values determined by DRAGON for the lattices and the full core model are used by SUS3D to calculate the sensitivity profiles for specific reactions of the isotopes present. The sensitivity profiles are then used alongside with the covariance matrices to calculate the uncertainty contribution of nuclear data to criticality. The sensitivity and uncertainty (S/U) results of the 2D model for full core, using the DRAGON/SUS3D code coupling are then compared with the S/U results of a 3D model of the full core using the code TSUNAMI within the SCALE6 package in reference [3]. The comparisons will show an excellent degree of consistency between the two methods, while reasons for possible differences in the results are also presented.

Acknowledgements

I would first like to thank Dr. Adriaan Buijs for giving me the opportunity to work and study in this field, and providing me with support throughout the program. I would also like to express my sincere gratitude to Dr. Guy Marleau at École Polytechnique de Montréal for his tremendous technical support without which it is difficult to imagine completing this work.

I would like to thank Pouya Sabouri at LPSC de Grenoble whose technical and moral support allowed me to gain a significant amount of knowledge in reactor physics.

I would like to thank the current and former McMaster graduate students Ima Ituen, Yonni Friedlander, Azin Behdadi and Farshab Talebi for making the office a much friendlier place than it could have been. Also, I would like to express my gratitude to the graduate students at École Polytechnique de Montréal for being patient and tolerant with my inability to speak French, and so available and kind when I needed help.

I would finally like to thank my family, Igor, Dylan and April for understanding anxiety.

Table of Contents

| | |
|---|-------------|
| ABSTRACT..... | II |
| ACKNOWLEDGEMENTS | III |
| TABLE OF CONTENTS | IV |
| LIST OF FIGURES | VIII |
| INTRODUCTION..... | 1 |
| FUNDAMENTAL THEORIES OF REACTOR PHYSICS | 4 |
| 1.1 The Neutron Flux..... | 4 |
| 1.2 The Transport Equation | 5 |
| 1.2.1 The Differential Form..... | 5 |
| 1.2.2 The Characteristic Form | 7 |
| 1.2.3 The Integral Form | 7 |
| 1.2.4 The Multi-group Approach..... | 8 |
| 1.3 The Solution Methods..... | 8 |
| 1.3.1 The Collision Probability Method | 9 |
| 1.4 Fundamentals of Lattice Calculations | 10 |
| 1.4.1 Resonance Self-Shielding | 11 |
| 1.4.1.1 Generalized Stamm'ler Method..... | 12 |
| 1.4.2 Homogenization and Condensation | 14 |
| 1.5 The Diffusion Equation | 15 |
| 1.5.1 Fick's Law | 15 |
| 1.6 Sensitivity and Uncertainty Analysis | 16 |
| 1.6.1 First Order Perturbation Theory..... | 17 |

| | |
|--|-----------|
| 1.6.2 Sensitivity Coefficients Calculations | 18 |
| 1.6.3 Error Sources and Correlations | 19 |
| 1.6.4 Uncertainty Calculations | 21 |
| 1.7 Codes Used..... | 22 |
| 1.7.1 DRAGON | 22 |
| 1.7.2 SUS3D | 22 |
| 1.7.3 DONJON..... | 24 |
| | |
| ZED-2 TRANSPORT CALCULATIONS AND S/U ANALYSIS..... | 25 |
| | |
| 2.1 Calculation Scheme..... | 25 |
| | |
| 2.2 ZEEP Rod Lattice | 25 |
| 2.2.1 Physical Parameters | 26 |
| 2.2.2 Choice of Geometry | 27 |
| 2.2.3 Spatial Discretization | 29 |
| 2.2.4 Choice of Reflective Boundary Condition Type | 30 |
| 2.2.5 Resonance Self-Shielding | 31 |
| 2.2.6 Energy Condensation and Homogenization..... | 32 |
| 2.2.7 ZEEP Rod Lattice Sensitivity | 32 |
| 2.2.8 ZEEP Rod k_{∞} Uncertainty | 36 |
| | |
| 2.3 (Th, Pu)O₂ Bundle Lattice..... | 37 |
| 2.3.1 Choice of Geometries | 38 |
| 2.3.2 Water and Air Cooled Bundles | 39 |
| 2.3.3 Spatial Discretization | 42 |
| 2.3.4 Energy Condensation and Homogenization..... | 44 |
| 2.3.5 (Th,Pu)O ₂ Bundle Lattice Sensitivity | 44 |
| 2.3.6 k_{∞} Uncertainty | 50 |
| 2.3.7 Reaction Rates | 50 |
| | |
| 2.4 2D Reactor Core..... | 55 |
| 2.4.1 Self Shielding Models..... | 56 |

| | | |
|--|--|-----------|
| 2.4.1.1 | The Sub-Geometry Self-Shielding Model | 57 |
| 2.4.1.2 | The Global Self-Shielding Model | 58 |
| 2.4.2 | k_{eff} Analysis | 59 |
| 2.4.3 | Full Core Sensitivity | 61 |
| 2.4.3.1 | K0 Site – Air Cooled and Water Cooled Bundle | 61 |
| 2.4.3.2 | K0 Site – ZEEP Rod and No Fuel | 68 |
| 2.4.4 | k_{eff} Uncertainty and Code to Code Comparison | 70 |
| 2.4.5 | Air Cooled Bundle vs. Water Cooled Bundle Reaction Rates..... | 72 |
| 2.4.6 | Moderator and Graphite Homogenization | 79 |
| ZED-2 FULL CORE DIFFUSION CALCULATIONS..... | | 81 |
| 3.1 | ZED-2 Critical Facility | 81 |
| 3.2 | Macroscopic Cross Section Library | 82 |
| 3.3 | K0 Site - ZEEP Rod | 83 |
| 3.3.1 | Carcel Lattice Geometry | 83 |
| 3.3.2 | Annular Lattice Geometry | 84 |
| 3.3.3 | Self-shielding | 86 |
| 3.3.4 | Full-core Discretization | 87 |
| 3.4 | K0 Site - No Fuel | 88 |
| 3.4.1 | Full Core Discretization..... | 88 |
| 3.5 | K0 Site – Water Cooled Bundle..... | 89 |
| 3.5.1 | Carcel Lattice Geometry | 89 |
| 3.5.2 | Annular Lattice Geometry | 91 |
| 3.5.3 | Full Core Discretization..... | 92 |
| 3.6 | K0 Site – Air Cooled Bundle..... | 93 |
| 3.7 | Overview | 93 |
| CONCLUSION | | 94 |

BIBLIOGRAPHY..... 98

List of Figures

| | |
|---|----|
| Figure 1: Particle balance in a control volume | 5 |
| Figure 2: SUSD3D calculation scheme | 23 |
| Figure 3: ZEEP rod lattice | 26 |
| Figure 4: Cartesian (Carcel) geometry vs. annular geometry | 27 |
| Figure 5: Flux spectrum of the annular and Cartesian ZEEP lattices | 28 |
| Figure 6: Spatial convergence of k_{∞} in ZEEP lattice | 30 |
| Figure 7: Group-wise ^{235}U ν ($S_I=0.937$) and ^{235}U fission ($S_I=0.442$) sensitivity profiles in the ZEEP lattice | 34 |
| Figure 8: ENDF/B-VII.0 group wise microscopic cross section data for ^{235}U (n,f), ^{235}U (n, γ), ^{238}U (n, γ) | 35 |
| Figure 9: Group-wise ^{238}U (n, γ) sensitivity ($S_I= -0.409$) profile in the ZEEP lattice..... | 35 |
| Figure 10: Group-wise ^{235}U (n, γ) sensitivity ($S_I=-8.64 \times 10^{-2}$) profile in the ZEEP lattice | 36 |
| Figure 11: (Th,Pu) O_2 central bundle [7] | 37 |
| Figure 12: Cartesian (left) and annular (right) geometries of the (Th,Pu) O_2 bundle..... | 39 |
| Figure 13: Flux spectra of the cooled and voided lattices | 41 |
| Figure 14: Energy integrated flux of the bundle lattice with 0 coolant and moderator subdivisions (left), with 5 coolant and 0 moderator subdivisions (center), with 5 coolant and 5 moderator subdivisions (right) | 43 |
| Figure 15: Homogenization scheme of the (Th,Pu) O_2 bundle..... | 44 |
| Figure 16: Air cooled vs. water cooled bundle group-wise sensitivity profiles of ^{239}Pu (ν) ($S_{I,A.C.}= 0.951$, $S_{I,W.C.}=0.953$) | 47 |
| Figure 17: Air cooled vs. water cooled bundle group-wise sensitivity profile of ^{232}Th (n, γ) ($S_{I,A.C.}= -0.348$, $S_{I,W.C.}= -0.292$) | 48 |
| Figure 18: Air cooled vs. water cooled bundle group-wise sensitivity plot of ^{239}Pu (Fiss) ($S_{I,A.C.}= 0.549$, $S_{I,W.C.}= 0.549$) | 48 |
| Figure 19: Air cooled vs. water cooled bundle group-wise sensitivity plot of ^{239}Pu (n, γ) ($S_{I,A.C.}= -0.195$, $S_{I,W.C.}= -0.191$) | 49 |
| Figure 20: Air cooled vs. water cooled bundle group-wise reaction rates of ^{239}Pu (Fiss) | 52 |
| Figure 21: Air cooled vs. water cooled bundle group-wise reaction rates of ^{232}Th (n, γ) . | 53 |

| | |
|---|----|
| Figure 22: Air cooled vs. water cooled bundle group-wise reaction rates of ^{239}Pu (n, γ) | 53 |
| Figure 23: Plan view of the ZED-2 core | 56 |
| Figure 24: The 6 2x2 subgeometries present in the ZED-2 core | 57 |
| Figure 25: Energy integrated flux of water-cooled (Th,Pu) O_2 bundle case (left) and the ZEEP rod case (right)..... | 60 |
| Figure 26: The flux spectra of the center of the core (the K0 site) of the four full core cases | 61 |
| Figure 27: ^{235}U (ν) group wise sensitivity profiles of K0 site= air cooled (Th,Pu) O_2 bundle ($S_I=0.808$) and K0 site= water cooled (Th,Pu) O_2 bundle ($S_I=0.808$) | 62 |
| Figure 28: ^{235}U (Fiss) group wise sensitivity profiles of K0 site= air cooled (Th,Pu) O_2 bundle ($S_I=0.403$) and K0 site= water cooled (Th,Pu) O_2 bundle ($S_I=0.421$) | 63 |
| Figure 29: ^{235}U (n, γ) group wise sensitivity profiles of K0 site= air cooled (Th,Pu) O_2 bundle ($S_I=-0.319$) and K0 site= water cooled (Th,Pu) O_2 bundle ($S_I=-0.273$) | 64 |
| Figure 30: ^{239}Pu (fiss) group wise sensitivity profiles of K0 site= air cooled (Th,Pu) O_2 bundle ($S_I=5.70 \times 10^{-2}$) and K0 site= water cooled (Th,Pu) O_2 bundle ($S_I=5.70 \times 10^{-2}$)..... | 65 |
| Figure 31: ^{232}Th (n, γ) group wise sensitivity profiles of K0 site= air cooled (Th,Pu) O_2 bundle and K0 site= water cooled (Th,Pu) O_2 bundle | 66 |
| Figure 32: Self-shielding corrected ^{232}Th (n, γ) water-cooled and voided cross sections | 66 |
| Figure 33: ^1H (n, elas) group wise sensitivity plots of K0 site= air cooled (Th,Pu) O_2 bundle ($S_I=2.07 \times 10^{-3}$) and K0 site= water cooled (Th,Pu) O_2 bundle ($S_I=1.15 \times 10^{-3}$)..... | 67 |
| Figure 34: ^{235}U (ν) and (fiss) group wise sensitivity plots of K0 site= ZEEP rod and K0 site= no fuel | 69 |
| Figure 35: ^{238}U (n, γ) group wise sensitivity plots of K0 site= ZEEP rod and K0 site= no fuel | 70 |
| Figure 36: Full core ^{235}U fission rates of the cases where the K0 site= air cooled (Th,Pu) O_2 bundle and K0 site= water cooled (Th,Pu) O_2 bundle..... | 73 |
| Figure 37: Group wise relative differences plot of ^{235}U fission rates - where the relative difference = $(\text{RX}_{\text{void}}-\text{RX}_{\text{cooled}})/\text{RX}_{\text{cooled}}$ | 74 |
| Figure 38: Full core ^{238}U absorption rates of the cases where the K0 site= air cooled (Th,Pu) O_2 bundle and K0 site= water cooled (Th,Pu) O_2 bundle..... | 74 |

| | |
|---|----|
| Figure 39: Group wise relative differences plot of ^{238}U absorption rates - where the relative difference = $(RX_{\text{void}}-RX_{\text{cooled}})/RX_{\text{cooled}}$ | 75 |
| Figure 40: Full core ^{239}Pu fission rates of the cases where the K0 site= air cooled (Th,Pu) O_2 bundle and K0 site= water cooled (Th,Pu) O_2 bundle..... | 76 |
| Figure 41: Group wise relative differences plot of ^{239}Pu fission | 76 |
| Figure 42: Full core ^{232}Th absorption rates | 77 |
| Figure 43: Group wise relative differences plot of ^{232}Th fission | 77 |
| Figure 44: Cross section of the ZED-2 reactor | 82 |
| Figure 45: Spatial convergence of the Carcel geometry discretization | 84 |
| Figure 46: Spatial convergence of the annular geometry discretization..... | 86 |
| Figure 47: Spatial convergence in the full core | 88 |
| Figure 48: Spatial convergence in the full core | 89 |

Introduction

Thorium fuel has been a topic of extensive research due to its advantages and benefits. Having an abundance three to four times larger than uranium in nature, thorium fuel has the ability to complement uranium fuels and ensure long term sustainability of nuclear power [1]. Moreover, ^{232}Th is a stronger fertile isotope than ^{238}U , having a thermal absorption cross section of approximately 7.4 barns (three times higher than that of ^{238}U). Upon absorption the fertile ^{232}Th breeds fissile ^{233}U , which contrary to ^{235}U and ^{239}Pu , has a $\bar{\nu}$ value (average number of neutrons generated per fission) greater than 2.0 throughout the energy spectrum. Thus, the $^{232}\text{Th} - ^{233}\text{U}$ cycle can operate in all the possible spectra (fast, epithermal and thermal) [1]. Due to these advantages, Canada began to examine the application of thorium fuel in CANDU reactors [2], [3], [4], [5], [6].

Headed by AECL, one of the experiments, performed in the ZED-2 critical facility in Chalk River Laboratories, used five (Th,Pu) O_2 bundles to analyze the physical parameters of the core containing such fuel [7]. The effects of the thorium fuel were observed on the overall state of the facility by monitoring the reactivity perturbations in the reactor upon inserting the five bundles in the center of the core. Subsequently, the effects of coolant voiding were observed upon ridding the five central bundles of their coolant. The core reactivity was controlled by adjusting the moderator height, thus each of the distinct cases mentioned above was characterized by a specific critical moderator height [7]. This work focuses on using reactor physics codes and concepts to simulate the aforementioned experiments.

In a critical facility, there is a steady state of neutron population. This means that the rate of production of neutrons is equal to the total rate of loss of neutrons. Subsequently, a critical facility is determined to have a multiplication constant, k_{eff} , of 1. The k_{eff} value is thus dependent on the rate of fission, absorption and leakage in the core, all of which are dictated by the neutron flux.

The transport equation is used to calculate the neutron flux and is presented in chapter 1. There are generally two computational methods of solving this equation: deterministic and stochastic methods. The research in this thesis has been performed using deterministic codes. The main advantage of deterministic methods is their lower

computation demand and time, while stochastic techniques offer more accurate results at the expense of higher computation needs.

Calculating the transport equation for a full reactor core in three dimensions is computationally prohibitive and at times impossible given the current computing capabilities. Therefore, the flux calculations are usually divided into two steps:

1. Using the transport equation to solve the neutron flux for a lattice cell, and subsequently calculating a set of homogenized macroscopic cross sections
2. Using the diffusion equation to solve the neutron flux in the full core with the usage of the previously calculated homogenized macroscopic cross sections

In this work the first step, solving the transport equation for lattice cells, is done using the lattice code DRAGON, version 3.05 [8] while the second step, solving the diffusion equation for the full core, is done using the full core code DONJON, version 3.1 [9].

It is important to note that even though these codes have been widely used and extensively tested, an “exact” solution is still impossible to determine due to the inevitable approximations used in several steps of the calculations. Various sources of uncertainty exist, originating from the knowledge about the nuclear data, the material compositions and the geometric description of the problem. To gain more confidence about the obtained results knowledge of these uncertainties is necessary [10]. This knowledge can be gained by sensitivity and uncertainty (S/U) analysis, permitting the user to determine the importance of various computational parameters and identifying the major sources of uncertainty in the nuclear data. The analysis allows for the establishment of reliable safety margins for the calculated and measured values [10].

This thesis focuses on the uncertainty in the nuclear data by using the law of error propagation [11] to calculate the impact of nuclear data uncertainties on the criticality of lattices and cores. The code system used to perform these calculations is a modified version of SUS3D, and the approach used in this code is based on the deterministic forward/adjoint perturbation method [10], [12].

This work will first illustrate the capabilities of the open-source and Canadian IST codes DRAGON and DONJON by comparing the full core simulation results to the benchmark experimental results. Furthermore, the work will also examine the coupling of DRAGON with the modified version of SUS3D by comparing the obtained S/U results by those determined in reference [3] using the SCALE 6 package.

The necessary theoretical background of the concepts used in the thesis are presented chapter 1. This includes a thorough explanation of the transport and diffusion equations and the deterministic methods used to solve them, and an explanation of sensitivity and uncertainty analyses and how SUS3D is used to perform these calculations for different cases.

The second chapter focuses on the transport calculations done by DRAGON for various lattice cells and two dimensional full core cases. Furthermore, each case's respective sensitivities and uncertainties to the different isotopes are presented, determined by using SUS3D. The results of the sensitivity and uncertainty analyses are then compared to results obtained from TSUNAMI-3D, which is part of the SCALE 6 package. This will prove the accuracy of the results obtained by the methods presented in this paper.

Subsequently, the final chapter is dedicated to simulating the full reactor cases in 3 dimensions in DONJON, using the homogenized macroscopic cross section libraries created by solving the transport equation for the respective lattice cells. Each case is simulated using the critical moderator height which characterizes the specific case in the experiment. This will further validate the simulation of the experiment.

Chapter 1

Fundamental Theories of Reactor Physics

1.1 The Neutron Flux

The fundamental quantity representing the neutron population is first described using a statistical mechanics approach. This approach considers the neutron population n inside a control volume V , travelling in a cone of $d\hat{\Omega}$ surrounding $\hat{\Omega}$ at some location \vec{r} in space, with an energy between E and dE at time t . The position of a single neutron is thus identified by seven quantities:

- three position coordinates: $\vec{r} = x \vec{i} + y \vec{j} + z \vec{k}$
- three velocity coordinates: one velocity module $V_n \equiv |\vec{V}_n|$ where $\vec{V}_n = \frac{d\vec{r}}{dt}$ and two components of direction $\hat{\Omega} = \frac{\vec{v}}{v}$
- the time t , only used in transient situations and not applicable in steady state calculations

The neutron population in a specific phase space volume element is thus defined by $n(\vec{r}, V_n, \hat{\Omega}, t) d^3r dV_n d^2\Omega$. The fundamental quantity in reactor physics, the neutron flux ϕ , is defined as:

$$\phi(\vec{r}, V_n, \hat{\Omega}, t) = V_n n(\vec{r}, V_n, \hat{\Omega}, t) \quad (1.1)$$

Another fundamental distribution is the angular current, which physically represents the number of neutrons, d^3r , with a specific velocity V_n and direction $\vec{\Omega}$, crossing an element of surface d^2S during time dt . This number is mathematically represented as:

$$d^3n = n(\vec{r}, V_n, \vec{\Omega}, t) [d^2S (V_n dt) \vec{\Omega} \cdot \vec{N}] \quad (1.2)$$

The angular current can be presented as the following:

$$\vec{J}(\vec{r}, V_n, \vec{\Omega}, t) = \vec{\Omega} \phi(\vec{r}, V_n, \vec{\Omega}, t) \quad (1.3)$$

1.2 The Transport Equation

1.2.1 The Differential Form

The transport equation is used to balance the neutron population in a volume $d^3r dV_n d^2\Omega$ within the region $\{\vec{r}, V_n, \vec{\Omega}\}$ during Δt . As derived in reference [13], the change in the neutron population can be calculated by subtracting the balance of neutrons leaving the volume d^3r , subtracting the number of neutrons lost during collisions, and adding the number of neutrons created.

Figure 1 shows a control volume C with a surrounding surface of ∂C . The number of neutrons in this control volume can be expressed by

$$\int_C d^3r n(\vec{r}, V_n, \vec{\Omega}, t) dV_n d^2\Omega \quad (1.4)$$

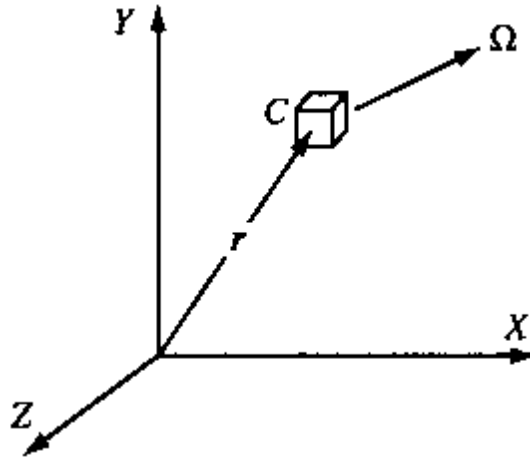


Figure 1: Particle balance in a control volume

Mathematically [13]:

- The change in the neutron population in the volume V during Δt is:

$$d^3A = \int_C d^3r [n(\vec{r}, V_n, \vec{\Omega}, t + \Delta t) - n(\vec{r}, V_n, \vec{\Omega}, t)] dV_n d^2\Omega \quad (1.5)$$

- To calculate the number of neutrons leaving the volume during Δt , the neutron current is integrated over the surface ∂C :

$$d^3B = \int_{\partial C} d^2r (\vec{\Omega} \cdot N) \phi(\vec{r}, V_n, \vec{\Omega}, t) dV_n d^2\Omega \Delta t \quad (1.6)$$

Using Gauss's theorem, equation (1.6) can be transformed into:

$$d^3B = \int_C d^3r \nabla \cdot \vec{\Omega} \phi(\vec{r}, V_n, \vec{\Omega}, t) dV_n d^2\Omega \Delta t \quad (1.7)$$

- The number of neutron collisions can be calculated using (1.8):

$$d^3C = \int_C d^3r \Sigma(\vec{r}, V_n) [V_n n(\vec{r}, V_n, \vec{\Omega}, t)] dV_n d^2\Omega \Delta t \quad (1.8)$$

- Finally, the number of new neutrons created is represented by:

$$d^3D = \int_C d^3r [Q(\vec{r}, V_n, \vec{\Omega}, t)] dV_n d^2\Omega \Delta t \quad (1.9)$$

Where $Q(\vec{r}, V_n, \vec{\Omega}, t)$ represents the source density.

The neutron balance can thus be written as:

$$d^3A = -d^3B - d^3C + d^3D \quad (1.10)$$

Upon expanding (1.10), removing the control volume integral in each term, and taking the limit as Δt approaches 0, the differential form of the transport equation is derived:

$$\begin{aligned} \frac{1}{V_n} \frac{\partial}{\partial t} \phi(\vec{r}, V_n, \vec{\Omega}, t) + \nabla \cdot \vec{\Omega} \phi(\vec{r}, V_n, \vec{\Omega}, t) + \Sigma(\vec{r}, V_n) \phi(\vec{r}, V_n, \vec{\Omega}, t) \\ = Q(\vec{r}, V_n, \vec{\Omega}, t) \end{aligned} \quad (1.11)$$

Considering a steady state problem, and substituting the energy, $E = \frac{mV_n^2}{2}$, as an independent variable instead of V_n , the equation becomes:

$$\nabla \cdot \vec{\Omega} \phi(\vec{r}, E, \vec{\Omega}) + \Sigma(\vec{r}, E) \phi(\vec{r}, E, \vec{\Omega}) = Q(\vec{r}, E, \vec{\Omega}) \quad (1.12)$$

Where $Q(\vec{r}, E, \vec{\Omega}) = Q_s(\vec{r}, E, \vec{\Omega}) + Q_f(\vec{r}, E, \vec{\Omega}) + S(\vec{r}, E, \vec{\Omega})$.

The scattering term is expanded to [14]:

$$Q_s(\vec{r}, E, \vec{\Omega}) = \int dE' \int d^2\Omega' \Sigma_s(\vec{r}, \vec{\Omega}' \cdot \vec{\Omega}, E' \rightarrow E) \phi(\vec{r}, \vec{\Omega}', E'), \quad (1.13)$$

and the fission term is expressed as:

$$Q_f(\vec{r}, E, \vec{\Omega}) = \chi(E) \int dE' \nu \Sigma_f(\vec{r}, E') \int d^2\Omega' \phi(\vec{r}, \vec{\Omega}', E'). \quad (1.14)$$

If a case is considered where the fixed source term, $S(\vec{r}, E, \vec{\Omega})$, identically vanishes, equation (1.12) becomes an eigenvalue problem and the fission term is modified to the form:

$$Q_f(\vec{r}, E, \vec{\Omega}) = \frac{\chi(E)}{k_{eff}} \int dE' \nu \Sigma_f(\vec{r}, E') \int d^2\Omega' \phi(\vec{r}, \vec{\Omega}', E') \quad (1.15)$$

Where k_{eff} is the multiplication constant.

1.2.2 The Characteristic Form

The *characteristic* of a neutron corresponds to a straight line with a specific direction $\vec{\Omega}$ describing the neutron trajectory [13]. By integrating the operator, $\nabla \cdot \vec{\Omega} \phi$ over the neutron's characteristic, while assuming that the neutron is at a distance s from the reference point \vec{r} , the forward characteristic form of the equation in steady state is derived as the following [13]:

$$-\frac{d}{ds} \phi(\vec{r} - s\vec{\Omega}, E) + \Sigma(\vec{r} - s\vec{\Omega}, E) \phi(\vec{r} - s\vec{\Omega}, E, \vec{\Omega}) = Q(\vec{r} - s\vec{\Omega}, E, \vec{\Omega}) \quad (1.16)$$

1.2.3 The Integral Form

In order to derive the integral form of the equation another fundamental concept, the optical path, must be introduced. The optical path, τ , is proportional to the exponential attenuation factor which upon multiplication by the neutron source at any point s is equal to a value proportional to the neutron flux at any point a [14]:

$$\tau(s, E) = \int_a^s ds' \Sigma(\vec{r} - s'\vec{\Omega}, E). \quad (1.17)$$

The following relation is then determined:

$$\begin{aligned} & \frac{d}{ds} [e^{-\tau(s,E)} \phi(\vec{r} - s\vec{\Omega}, E, \vec{\Omega})] \\ &= e^{-\tau(s,E)} [-\Sigma(\vec{r} - s\vec{\Omega}, E) \phi(\vec{r} - s\vec{\Omega}, E, \vec{\Omega}) + \\ & \quad \frac{d}{ds} \phi(\vec{r} - s\vec{\Omega}, E, \vec{\Omega})] \end{aligned} \quad (1.18)$$

Upon substituting the characteristic form of the transport equation, equation (1.16) into equation (1.18) and subsequently integrating it between 0 and ∞ , the integral form of the transport equation is determined:

$$\phi(r, E, \vec{\Omega}) = \int_0^\infty ds e^{-\tau(s,E)} Q(\vec{r} - s\vec{\Omega}, E, \vec{\Omega}) \quad (1.19)$$

1.2.4 The Multi-group Approach

By discretizing the continuous energy spectrum into a finite number of G energy groups, the energy-dependent quantities of a neutron can be averaged in each group, such that the neutrons behave as one-speed particles within each energy group.

$$W_g = \{E; E_g \leq E \leq E_{g-1}\}; \quad g = 1, G \quad (1.20)$$

Thus, the differential form of the transport equation, (1.12), can be expressed as:

$$\nabla \cdot \vec{\Omega} \phi_g(\vec{r}, \vec{\Omega}) + \Sigma_g(\vec{r}) \phi_g(\vec{r}, \vec{\Omega}) = Q_g(\vec{r}, \vec{\Omega}) \quad (1.21)$$

The characteristic form, (1.16), becomes:

$$-\frac{d}{ds} \phi_g(\vec{r} - s\vec{\Omega}) + \Sigma_g(\vec{r} - s\vec{\Omega}) \phi_g(\vec{r} - s\vec{\Omega}, \vec{\Omega}) = Q_g(\vec{r} - s\vec{\Omega}, \vec{\Omega}) \quad (1.22)$$

And finally, the integral form, (1.19), can be represented by:

$$\phi_g(r, \vec{\Omega}) = \int_0^\infty ds e^{-\tau_g(s)} Q_g(\vec{r} - s\vec{\Omega}, \vec{\Omega}) \quad (1.23)$$

1.3 The Solution Methods

Given all the assumptions thus far, the transport equation can still not be solved analytically for complex geometries, thus numerical methods must be used. Two general classes of methods are commonly used: deterministic methods and stochastic ones. The deterministic methods are further divided into four prominent methods:

1. Collision probability method – based on equation (1.19)
2. Method of characteristics – based on equation (1.16)
3. Discrete ordinates method – based on equation (1.12)
4. Spherical harmonics method – based on equation (1.12)

In this thesis, the only method used was the collision probability method. Some results were compared with solutions from stochastic methods.

The stochastic approach, also called Monte-Carlo methods, have proved to produce more accurate result, however this comes at a cost of increasing computational demand [15].

1.3.1 The Collision Probability Method

Assuming an isotropic source, the collision probability method solves the integral transport equation by spatially discretizing equation (1.19). In a case which contains N regions, the CP method creates an NxN matrix in each energy group [13]. In this section, the formalism of the collision probability method is shown over an infinite domain, as derived in reference [14].

The flux is initially integrated through the solid angles to determine the integrated flux:

$$\begin{aligned}\phi_g(\vec{r}) &= \int_{4\pi} d^2\Omega \phi_g(\vec{r}, \vec{\Omega}) \\ &= \frac{1}{4\pi} \int_{4\pi} d^2\Omega \int_0^\infty ds e^{-\tau_g(s)} Q_g(\vec{r} - s\vec{\Omega})\end{aligned}\quad (1.24)$$

Let $\vec{r}' = \vec{r} - s\vec{\Omega}$ with $d^3r' = s^2 d^2\Omega ds$, substituting this into (1.24) leads to:

$$\phi_g(\vec{r}) = \frac{1}{4\pi} \int_{\infty} d^3r' \frac{e^{-\tau_g(s)}}{s^2} Q_g(\vec{r}') \quad (1.25)$$

Subsequently the problem is discretized into infinite regions with specific volumes V_i , and upon integration over each region V_i and multiplication by the macroscopic cross section in the region, equation (1.25) becomes:

$$\begin{aligned}& \int_{V_j} d^3r \Sigma_g(\vec{r}) \phi_g(\vec{r}) \\ &= \frac{1}{4\pi} \int_{V_j} d^3r \Sigma_g(\vec{r}) \sum_i Q_{i,g} \int_{V_i} d^3r' \frac{e^{-\tau_g(s)}}{s^2}\end{aligned}\quad (1.26)$$

Let

$$\phi_g = \frac{1}{V_j} \int_{V_j} d^3r \phi_g(\vec{r}) \quad (1.27)$$

$$\Sigma_{j,g} = \frac{1}{V_j \phi_{j,g}} \int_{V_j} d^3r \Sigma_g(\vec{r}) \phi_g(\vec{r}) \quad (1.28)$$

$$p_{ij,g} = \frac{1}{\Sigma_{j,g} 4\pi V_i} \int_{V_i} d^3r' \int_{V_j} d^3r \frac{e^{-\tau_g(s)}}{s^2} \quad (1.29)$$

Equation (1.29) is the reduced collision probability matrix, which occurs in a case where the total cross section $\Sigma_g(\vec{r})$ is constant and equal to $\Sigma_{j,g}$ in region V_j . Thus, equation (1.26) can be re-written as:

$$V_j \phi_{j,g} = \sum_i Q_{i,g} V_i p_{ij,g} \quad (1.30)$$

Upon introducing the reciprocity property of the CPs, i.e.:

$$V_i p_{ij,g} = V_j p_{ji,g} \quad (1.31)$$

equation (1.30) can be simplified to:

$$\phi_{i,g} = \sum_j Q_{j,g} p_{ij,g} \quad (1.32)$$

The collision probability method is usually done in three steps [13]:

1. The geometry is divided into a large number of tracks (to appropriately take into account a significant number of neutron trajectories). In this paper the geometries defined are 2D geometries, thus two parameters defining the tracking are the number of azimuthal angles and the number of parallel tracking lines per cm.
2. Using the tracking information and the regional macroscopic cross sections, numerical integration is done to compute the collision probability matrices.
3. Finally, integrated flux is calculated using equation (1.32).

1.4 Fundamentals of Lattice Calculations

The transport equation, as stated previously, is not generally calculated for a full core due to its high computational demand. Lattice calculations are thus initially performed for an infinitely repeating unit cell within the core, using the operating conditions applied only to the small component in question. Using the correct boundary conditions, it is ensured that the flux that is determined for the lattice is a stationary one applied strictly to the cell. The calculations begin by accessing the cross sections corresponding to the isotopes in the problem. The cross sections are subsequently interpolated as they vary with the temperature. Subsequently, a self-shielding module is applied to calculate dilution cross sections for the applicable isotopes, and use these cross sections to interpolate the resonance integrals of the isotopes in resonance regions. Using the given data gained from tracking and the corrected nuclear data, the flux calculations are done using the CP method described in the previous section. Finally, homogenization and condensation of the reaction rates are done using either a flux-volume weighting method, for cases where

the output geometry is homogenous, or *superhomogenization* method for cases where the output geometry is heterogeneous.

The data obtained from the final homogenization and condensation of the lattice cell are then used for full core calculations.

1.4.1 Resonance Self-Shielding

Scattering reactions between the neutrons and the various nuclides present in a reactor are the main cause of high energy neutrons slowing down. Inelastic scattering reactions can lead to a loss of a large fraction of neutron energy, however these reactions only occur at high neutron energies (50 keV for light nuclides and 1 MeV for heavy ones) with relatively small cross sections [13]. Thus, the main cause of the thermalization of neutrons is elastic scattering.

When considering neutrons with energies higher than a few eV, the scattering reactions only lead to a slowing down effect and thus equation (1.12) can be rewritten as:

$$\nabla \cdot \vec{\Omega} \phi(\vec{r}, u, \vec{\Omega}) + \Sigma(\vec{r}, u) \phi(\vec{r}, u, \vec{\Omega}) = \frac{1}{4\pi} [S_f(\vec{r}, u) + \sum_{j=1}^J R_j\{\phi(\vec{r}, u)\}] \quad (1.33)$$

Here u is called the lethargy of the neutron. This value is the fraction of the kinetic energy lost by a neutron upon an elastic scattering reaction and it is represented as

$$u = \ln \frac{E_0}{E}.$$

$S_f(\vec{r}, u)$ is the fission source and $R_j\{\phi(\vec{r}, u)\}$ is the elastic slowing down operator, defined as:

$$R_j\{\phi(\vec{r}, u)\} = \int_0^u du' \Sigma_{s0,j}(\vec{r}, u \leftarrow u') \phi(\vec{r}, u') \quad (1.34)$$

However, as discussed in the previous section, this equation is solved using a multigroup approximation, which assumes a constant cross section within each energy group. Yet, many heavy nuclides are resonant with small resonance widths, and the multigroup discretization of each of these resonances would require an impractically large number of energy groups. The flux in these resonant regions is very low, and neglecting this effect by using average cross section will lead to an over estimation of the reaction rates.

Thus, the objective of a self-shielding model is to determine the microscopic self-shielded cross section for a specific reaction y in an energy group g , $\bar{\sigma}_y(g)$, expressed as [16]:

$$\bar{\sigma}_y(g) = \frac{\int_{u_{g-1}}^{u_g} du \sigma_y(u) \phi(u)}{\int_{u_{g-1}}^{u_g} du \phi(u)} \quad (1.35)$$

where

u_{g-1} , u_g = lethargy limits of group g

$\sigma_y(u)$ = the microscopic cross section of reaction y .

However, to solve the equation the value of flux is needed, and the value of flux needs to be calculated using the self-shielded cross sections. Thus further approximations are applied in a process called the generalized Stamm'ler method.

1.4.1.1 Generalized Stamm'ler Method

The goal of the Stamm'ler method is to solve equation (1.35) for a heterogeneous multi-group problem, using specific approximations. The first approximation involves the assumption that the neutron flux is factorized as the product of a resonant fine-structure function $\phi_i(u)$ with a regular distribution $\psi_i(u)$ such that [16]:

$$\phi_i(u) = \phi_i(u) \psi_i(u) \quad (1.36)$$

$\psi_i(u)$ is called the macroscopic flux which is used to describe the asymptotic behavior of the neutron flux. The fine-structure function is then used to describe the effective resonance integral $I_y(g)$ for nuclear reaction y . The calculation of this integral is an imperative part of the method, which ultimately leads to the final self-shielded cross section value:

$$I_y(g) = \frac{1}{U_g} \int_{u_{g-1}}^{u_g} du \sigma_y(u) \phi(u) \quad (1.37)$$

While the average fine-structure function can be represented as follows:

$$I_y(g) = \frac{1}{U_g} \int_{u_{g-1}}^{u_g} du \phi(u) \quad (1.38)$$

where $U_g = u_g - u_{g-1}$.

Using equations (1.37) and (1.38), equation (1.35) can be re-written as:

$$\bar{\sigma}_y(g) = \frac{1}{\bar{\varphi}(g)} I_y(g) \quad (1.39)$$

The goals of the method are then to calculate the values of $I_y(g)$ and $\bar{\varphi}(g)$. Both these values, however, depend on the averaged microscopic dilution cross section, $\bar{\sigma}_e$, whose calculation is beyond the scope of this thesis and details of its calculation can be found in [16].

Subsequent to the determination of $\bar{\sigma}_e$, the averaged fine-structure function can be calculated using the following equation:

$$\bar{\varphi}(g) = 1 - \frac{1}{\bar{\Sigma}_e(g)} [I(g) - \sum_h \frac{U_h}{U_g} I_s(g \leftarrow h)] \quad (1.40)$$

where $I(g)$ is the total effective resonance integral and $I_s(g \leftarrow h)$ is the transfer effective resonance integral, both of which are interpolated from the cross-section library at the specific $\bar{\sigma}_e(g)$.

However, Livolant and Jeanpierre found that this approach produces an error in some heterogeneous problems [17]. This was due to the fact that the average macroscopic dilution cross section differed from the escape function evaluated at an average cross section, $E[\bar{\Sigma}_x^*(g)]$. Thus, a procedure known as the Livolant-Jeanpierre normalization was proposed, where $\bar{\Sigma}_e(g)$ is replaced with $E[\bar{\Sigma}_x^*(g)] = \frac{1}{p_{xx}\Sigma_x^*} - \Sigma_x^*$ in equation (1.40):

$$\bar{\varphi}(g) = 1 - \frac{1}{E[\bar{\Sigma}_x^*(g)]} [I(g) - \sum_h \frac{U_h}{U_g} I_s(g \leftarrow h)] \quad (1.41)$$

Furthermore, the relationship between the heterogeneous resonant integral for reaction y, and the pre-tabulated homogeneous resonant integral for reaction y, I_y^H , can be defined as the following:

$$I_y(g) = I_y^H[g, \bar{\sigma}_e(g)] \quad (1.41)$$

Upon the calculation of the average resonant cross sections and subsequently the flux, a homogenization and condensation step is followed; where condensation leads to a few group energy discretization and homogenization is used to calculate a set of nuclear data corresponding to a macro-geometry.

1.4.2 Homogenization and Condensation

To perform full core calculations using exact geometries, the properties calculated in the lattice using the transport equation must be homogenized over macro-regions and condensed over the energy groups. Two methods of homogenization and condensation will be discussed and used in this paper, the traditional flux-volume weighting (FVW) method and *superhomogenization* (SPH) method.

In the FVW method, the original quantities which were stored in a $N \times G$ matrix (N = number of regions, G = number of groups) are condensed and homogenized into an $M \times K$ matrix, such that for every index $m \in [1, M]$ there exists a set of indices $n \in [1, N]$: N_m ; and for every index $k \in [1, K]$ there exists a set of indices $G \in [1, G]$: G_k .

The average homogenized cross section in region m and group k is calculated by [18]:

$$\Sigma_{m,k}^{ave} = \sum_{i \in N_m} \sum_{g \in G_k} \frac{V_i \Sigma_{i,g} \phi_{i,g}}{V_i \phi_{i,g}} \quad (1.42)$$

The FVW method can be accurately used in all cases where the final output geometry is homogeneous. In cases where heterogeneity exists in the output geometry, the FVW does not ensure the preservation of reaction rates [13]. In these specific cases, the SPH method is used.

The SPH method calculates the homogenized cross section using $\mu_{m,k}$, the SPH factor [18].

$$\tilde{\Sigma}_{m,k}^{ave} = \mu_{m,k} \Sigma_{m,k}^{ave} \quad (1.43)$$

where $\tilde{\Sigma}_{m,k}^{ave}$ is the SPH corrected homogenized cross section and $\Sigma_{m,k}^{ave}$ is the FVW homogenized cross section.

$\mu_{m,k}$ is calculated using the following relation:

$$\mu_{m,k} = \frac{\bar{\phi}_{m,k}^{het}}{\phi_{m,k}^{hom}} = \frac{\left[\sum_{i \in N_m} \sum_{g \in G_k} \frac{V_i \phi_{i,g}}{V_i} \right]}{\phi_{m,k}^{hom}} \quad (1.44)$$

where,

$\bar{\phi}_{m,k}^{het}$: average neutron flux over a coarse (homogenized) region k in energy group m , obtained by cell-heterogeneous calculations

$\phi_{m,k}^{hom}$: average neutron flux over a coarse (homogenized) region k in energy group m , obtained by SPH corrected cross sections

$\phi_{i,g}$: neutron flux in heterogeneous region i obtained by cell-heterogeneous calculations
It is important to note that in equation (1.44), the SPH factor depends on the average flux enumerated by SPH corrected cross sections, hence an iterative strategy is used to calculate $\mu_{m,k}$, starting from an initial guess of the factor (usually 1).
Upon the calculation of homogenized and condensed nuclear data, the diffusion equation can be solved for the exact geometry in 3 dimensions.

1.5 The Diffusion Equation

Writing the neutron balance over the full core domain in energy group g will have the form [13]:

$$\text{Leakage rate} + \text{Collision rate} = \text{Sources}$$

which symbolically is:

$$\nabla \cdot \vec{J}_g(\vec{r}) + \Sigma_g(\vec{r})\phi_g(\vec{r}) = Q_g(\vec{r}) \quad (1.45)$$

where $\vec{J}_g(\vec{r})$ is the integrated current, calculated by directional integration over equation (1.3):

$$\vec{J}_g(\vec{r}) = \int_{4\pi} d^2\Omega \vec{J}(\vec{r}, \vec{\Omega}) = \int_{4\pi} d^2\Omega \vec{\Omega} \phi(\vec{r}, \vec{\Omega}) \quad (1.46)$$

However, solving this equation over a complex full core geometry can prove to be computationally prohibitive. Thus, simplifications are made to solve equation (1.45) using an approximation that relates the integrated current to the integrated flux. This relationship is called Fick's law.

1.5.1 Fick's Law

Fick's law formulates the fact that neutrons have a tendency to migrate from areas of higher neutron concentration to areas of lower neutron concentration. Using this fact, Fick's law relates the neutron current to the gradient of the neutron flux:

$$\vec{J}_g(\vec{r}) = -D_g(\vec{r})\vec{\nabla}\phi_g(\vec{r}) \quad (1.47)$$

where D is the diffusion coefficient. The derivation of the directional diffusion coefficient tensor is beyond the scope of this paper, and it is presented fully in [13]. It is

important to note that Fick's law is acceptable on the scale of a full reactor, but it breaks down at the level of lattice calculations [13].

Substituting equation (1.47) in to (1.45) leads to the multi-group diffusion equation:

$$\begin{aligned} \vec{\nabla} \cdot D_g(\vec{r}) \vec{\nabla} \phi_g(\vec{r}) + \Sigma_g(\vec{r}) \phi_g(\vec{r}) &= Q_g(\vec{r}) \\ &= \sum_{h=1}^G \Sigma_{s,g \leftarrow h}(\vec{r}) \phi_h(\vec{r}) + \lambda \chi_g(\vec{r}) \sum_{h=1}^G \nu \Sigma_{f,h}(\vec{r}) \phi_h(\vec{r}) \end{aligned} \quad (1.48)$$

where $\lambda = 1/k_{\text{eff}}$, is the eigenvalue of the problem.

The solution of the eigenproblem (1.48) behaves in a typical way such that only the fundamental solution of the problem, which corresponds to the largest absolute value of the eigenvalue, is equal to the inverse of the effective multiplication constant K_{eff} [13].

This is the only solution that has a physical meaning and leads to positive neutron flux over the full reactor domain.

1.6 Sensitivity and Uncertainty Analysis

“In practice, the results of experiments seldom coincide with the computational results obtained from the mathematical models of the respective experiments. Discrepancies between the results are due to both experimental and computational uncertainties.” [19]

Uncertainties in computer models can arise from various sources and can be categorized as [19]:

1. Modeling uncertainties arising from the inadequacy of mathematical equations to represent the specific phenomena
2. Modeling uncertainties arising from the numerical methods used to solve the model's equations
3. Parameter uncertainties arising from uncertainty in the data and parameters in the problem (e.g. cross sections)

This thesis focuses on nuclear data uncertainties, specifically uncertainty in the isotopic cross sections. Using sensitivity analysis, these uncertainties are propagated to k_{eff} values. However, at this point the information of data uncertainties is very limited and varies significantly between different libraries [20].

A modified version of SUS3D was used to perform the sensitivity and uncertainty analysis. This code uses the direct and adjoint flux values provided by DRAGON calculations to perform first order perturbation theory which ultimately leads to the determination of sensitivity coefficients. Subsequently, with the usage of covariance matrices, the uncertainty worth of specific cross sections are calculated.

1.6.1 First Order Perturbation Theory

Using operator notation, the transport equation can be re-written as the following:

$$\mathbf{A}\vec{\phi} = \lambda\mathbf{F}\vec{\phi} \quad (1.49)$$

where

$$\mathbf{A}\vec{\phi} = (\hat{\Omega} \cdot \nabla)\vec{\phi} + \Sigma_t\vec{\phi} - \Sigma_s\vec{\phi} \quad (1.50)$$

and

$$\mathbf{F}\vec{\phi} = \lambda\chi(\nu\Sigma_f)^T \quad (1.51)$$

Assuming that there is a lattice cross section perturbation by $\delta\Sigma_x$ due to changes in the local parameters, the transport operators will also change to:

$$\mathbf{A}_p = \mathbf{A} + \delta\mathbf{A} \quad (1.52)$$

and

$$\mathbf{F}_p = \mathbf{F} + \delta\mathbf{F} \quad (1.53)$$

Thus, equation (1.49) becomes

$$(\mathbf{A} + \delta\mathbf{A})(\vec{\phi} + \delta\vec{\phi}) = (\lambda + \delta\lambda)(\mathbf{F} + \delta\mathbf{F})(\vec{\phi} + \delta\vec{\phi}) \quad (1.54)$$

Ignoring the higher order perturbations and simplifying the above equation leads to:

$$\mathbf{A}\delta\vec{\phi} + \delta\mathbf{A}\vec{\phi} = \lambda\delta\mathbf{F}\vec{\phi} + \lambda\mathbf{F}\delta\vec{\phi} + \delta\lambda\mathbf{F}\vec{\phi} \quad (1.55)$$

An adjoint, ϕ^* , is then defined which satisfies the following relation:

$$\mathbf{A}^*\vec{\phi}^* = \lambda\mathbf{F}^*\vec{\phi}^* \quad (1.56)$$

where

$$\langle \vec{\phi}^*, \mathbf{A}\vec{\phi} \rangle = \langle \mathbf{A}^*\vec{\phi}^*, \vec{\phi} \rangle \quad (1.57)$$

The \langle , \rangle notation indicates an integration over the continuous independent variables or a sum over the discrete independent variables (in this case, energy, volume and solid angle):

$$\langle f(\vec{r}, \vec{\Omega}, E), h(\vec{r}, \vec{\Omega}, E) \rangle = \int d^3r \int dE \int d^2\Omega f(\vec{r}, \vec{\Omega}, E) h(\vec{r}, \vec{\Omega}, E)$$

Taking the inner product of equation (1.55) with $\vec{\phi}^*$ leads to:

$$\begin{aligned} \langle \phi^*, \mathbf{A}\delta\vec{\phi} \rangle + \langle \phi^*, \delta\mathbf{A}\vec{\phi} \rangle = \lambda \langle \phi^*, \delta\mathbf{F}\vec{\phi} \rangle + \lambda \langle \phi^*, \mathbf{F}\delta\vec{\phi} \rangle + \\ \delta\lambda \langle \phi^*, \mathbf{F}\vec{\phi} \rangle \end{aligned} \quad (1.58)$$

Upon applying the property shown in (1.57) and simplifying based on equation (1.56), the final equation expressed in terms of $\delta\lambda$ is:

$$\delta\lambda = - \frac{\langle \vec{\phi}^*, (\lambda\delta\mathbf{F} - \delta\mathbf{A})\vec{\phi} \rangle}{\langle \vec{\phi}^*, \mathbf{F}\vec{\phi} \rangle} \quad (1.59)$$

Thus, only the knowledge of the flux and the adjoint flux for a reference case is necessary to determine the first-order alteration in the eigenvalue of the perturbed problem, provided that $\delta\mathbf{A}$ and $\delta\mathbf{F}$ are determined explicitly [21]. Reference [22] illustrates that the error found in $\delta\lambda$ is first order with respect to $\delta\vec{\phi}$.

The adjoint flux is also calculated in DRAGON using the multi-group collision probability method, and with the application of a pseudo adjoint flux, a similar algorithm required for the calculation of direct flux is applied to the calculation of adjoint flux. The details of the calculations are found in reference [23].

1.6.2 Sensitivity Coefficients Calculations

In recent times, sensitivity and uncertainty analysis has played a significant role in discussions of target accuracies, criticality safety assessment evaluation of methods to reduce uncertainty in a system [24]. Changes in the cross sections can have both direct and indirect effects. For example, changes in the hydrogen isotope will have a direct effect on k_{eff} of the reactor, however it will also play a role in the resonance escape probabilities of heavier isotopes, thus affecting k_{eff} indirectly [21]. In this thesis only direct effects will be examined, and upon comparison with other results the relevance of implicit effects will be determined.

The explicit sensitivity is defined as [20]:

$$S_{\lambda}^{\sigma_x} = \frac{\partial\lambda}{\partial\sigma_x} \cdot \frac{\sigma_x}{\lambda} \quad (1.60)$$

where σ_x is the microscopic cross section for reaction x. Substituting (1.60) into (1.59) yields the equation for the energy, volume and solid angle integrated sensitivity coefficient:

$$S_{\lambda}^{\sigma_x} = -\frac{\sigma_x}{\lambda} \left[\frac{\langle \vec{\phi}^*, \left(\lambda \frac{\partial \mathbf{F}}{\partial \sigma_x} - \frac{\partial \mathbf{A}}{\partial \sigma_x} \right) \vec{\phi} \rangle}{\langle \vec{\phi}^*, \mathbf{F} \vec{\phi} \rangle} \right] \quad (1.61)$$

The complete process to calculate the group-wise volume integrated sensitivity coefficients is found in reference [10], with the final equation being:

$$S_{\lambda,g}^{\sigma_x^i} = \frac{1}{k_{eff}} \sum_n V_i [\rho_n^i (-\sigma_{t,g,n}^{x,i} \sum_m \Phi_{g,n,m} \Phi_{g,n,m}^* \Delta\Omega_m + \sum_{g'} \sum_{l=0}^L \sigma_{l,g \rightarrow g'}^{x,i} \sum_{n=-l}^l M_{g,n}^{l,n} M_{g',n}^{*l,n})] \quad (1.62)$$

where

V_i : the volume of region i

ρ_n^i : the number density of isotope i in region n

$\sigma_{t,g,n}^{x,i}$: the total microscopic cross section of isotope i, reaction x, in group g and region n

$\Phi_{g,n,m}, \Phi_{g,n,m}^*$: the direct and adjoint flux values respectively in group g, region n and solid angle m

$\sigma_{l,g \rightarrow g'}^x$: l^{th} legendre coefficient of the scattering microscopic cross section from group g to g'

$M_{g,i}^{l,n}, M_{g',i}^{*l,n}$: direct and adjoint angular flux moments respectively

The sources of error in the nuclear data and their correlations alongside with the sensitivity profiles are subsequently used to determine the nuclear data uncertainty propagation.

1.6.3 Error Sources and Correlations

Often cross section experiments employ very similar geometric configurations which allows for the determination of broad categories of error sources. These errors are then categorized into two general groups, random errors and systematic ones. A random error only affects one data point, while systematic ones affect two or more data points in a

correlated manner [11]. A paper by D.L. Smith et al. [11] lists the various sources of error and their correlations when determining activation and fission ratios data.

A major source of error is event statistics which include all errors which occur due to statistical errors of measure counts (e.g. activity decay counts). These errors are only correlated under specific contexts. For example, if more than one activation cross section is determined from a single irradiation, then the statistical error during that irradiation affects all the data points and thus is fully correlated between all the data points.

Another significant contributor is the method used in determination of corrected cross sections from the raw data. An example of such procedures is the fission extrapolation. Some fission events produce very low signals and are unavoidably lost in noise distribution. If every fission event is extrapolated and corrected individually, then this problem becomes a random source of error. However, if fission events are grouped and extrapolated together, then the sources of error are correlated and thus systematic [11].

If values of cross sections are to be determined, as opposed to their ratios, then the neutron flux needs to be determined for a standard reaction. In order to do this, a well-known cross section (such as ^{235}U fission) is used to determine the flux, which in turn is used to determine the cross section in question. However, this introduces another source of error, generally systematic in nature, due to the uncertainty in the standard cross section used to determine the flux.

A more complete list of sources of errors is listed in reference [11].

The fundamental physical quantities measured in an experiment (e.g. count rates, masses, etc.) can be represented by x_k ($k=1..L$) while the results computed from each of these fundamental quantities (e.g. cross sections) can be represented by P_i ($i=1,n$). To calculate individual components of the covariance matrix, $(D)_{ij}$, knowledge of the values of errors present in each measurement, alongside with their correlation to other errors are necessary [11]:

$$(D)_{ij} = \sum_{l=1}^L S_{i,j,l} e_{i,l} e_{j,l} \quad (1.63)$$

where l represents the specific measurement, $e_{i,l}$ is the partial error of measurement l corresponding to P_i , and $e_{j,l}$ is the partial error of measurement l corresponding to P_j , and $S_{i,j,l}$ represents the “micro correlation” coefficient which represents the correlation

between the partial errors $e_{i,l}$ and $e_{j,l}$. The partial errors are recorded throughout the experiment, and thus accessing these values is not difficult. However, the micro correlation coefficients, $-1 \leq S_{i,j,l} \leq 1$, prove to be much more tedious to determine. These values can be obtained analytically, see reference [11] for details, or subjectively by the experimenter.

Hence, the difference between covariance matrices of different libraries can be quite significant, due to their differences in experimental design and estimations [12].

1.6.4 Uncertainty Calculations

The sensitivity coefficients form a $1 \times M$ vector, in which $M = I$ number of isotopes multiplied by X number of reactions and G number of energy groups. This vector, alongside with the $M \times M$ covariance matrix are used together to calculate the uncertainties of the reactions in each energy group:

$$\sigma_{k_{xy}}^2 = S_{\lambda,g}^{\sigma_x^i} D_{\sigma_x^i, \sigma_y^j} \left(S_{\lambda,g'}^{\sigma_y^j} \right)^T \quad (1.64)$$

where $D_{\sigma_x^i, \sigma_y^j}$ is the covariance matrix associated with reaction x in isotope i and reaction y in isotope y . Covariance data provide a quantification of the strength of correlation between two nuclear data. The covariance matrix is a representation of the covariance data in such a way that the element in the i and j position is the covariance between the i^{th} and j^{th} reaction. The matrix is set up in such a way that the relative variances, $(\sigma_x^i)^2$, are along the matrix diagonal and represent the experimental variance of a specific reaction of an individual isotope. The off-diagonal terms in the matrix represent the covariance of one reaction, σ_x^i , with respect to another, σ_y^j .

Due to the complex understanding of statistical work required to produce these covariance matrices, the job is found to be a tedious, time consuming and non-trivial work [11]. This is the reason why different covariance matrices derived from different libraries, can often lead to different results. This fact will be exemplified later in the thesis, when results obtained using different libraries are compared.

1.7 Codes Used

1.7.1 DRAGON

DRAGON version 3.05 was used in this paper to solve the transport equation for various lattices. Developed at École Polytechnique de Montréal, DRAGON contains a collection of models that simulate the behavior of the neutron within a unit cell or an assembly [8]. The code is divided into various modules which perform different calculations, and are all linked together using the GAN generalized driver.

Listed below are the DRAGON modules used in this paper:

- The LIB: module was used to read the 69-group library with a WIMS-D format [25]. DRAGON also has its own DRAGLIB libraries, with the further options to use MATXS [26], WIMS-AECL [27], and APOLLO [28] formatted libraries
- Modules were used to define the geometry and generate tracking files containing regional volumes and track lengths, two of them were used in this paper:
 - EXCELT:, which creates integration lines for full cell calculations and
 - NXT:, which is similar to EXCELT but allows for more usage of block geometries
- The SHI: module was used to calculate the resonance self-shielded cross sections using the generalized Stamm'ler method with the option of Livolant- Jeanpierre normalization (option LJ) or not (NOLJ)
- The ASM: module was used to determine the multi-group complete collision probability matrices
- The FLU: module was used to solve the multi-group transport equation for the flux, the adjoint flux and the multiplication constant, k_{eff}
- The EDI: module was used to edit the output and at the same time perform FVW or SPH method homogenization and condensation
- The COMPO: module was used to save the homogenized and condensed nuclear data in a readable format for later use in DONJON

1.7.2 SUS3D

SUS3D development started from the code SUSD, which was created in the late 1980's

[29]. Maintained by the OECD/NEA, this code uses first-order perturbation theory to obtain multi-group, multi-dimensional sensitivity coefficients. A modified version of the code is used that allows coupling with DRAGON to obtain direct and adjoint flux values [12]. Cross sections of specific reactions were obtained by the nuclear data processing system NJOY. NJOY is a modular computer code that is used to read evaluated nuclear data in an ENDF format, transform the library, and output the library with specific formats [30]. In this case the GROUPT module of the code was used to obtain 69-group cross section libraries from the ENDF/B-VII library.

The covariance matrices were taken from the SCALE 6 44-group covariance matrix library and converted into a 69-group format using ANGELO/LAMBDA. The matrices were used alongside with the sensitivity profiles to calculate the variances and the standard deviations in the integral response of interest, k_{eff} .

The program is divided into three “overlays”. Overlay 1 calculates the matrices based on the products of $\phi_{g,i} \cdot \phi_{g,i}^*$ and $\phi_{g',i} \cdot \phi_{g,i}^*$. Overlay 2 calculates the group-wise and integral sensitivity coefficients based on the results of overlay 1, and cross sections obtained from NJOY. Finally, overlay 3 uses the results from overlay 2 and the covariance matrices taken from the SCALE 6 44-group library and processed by ANGELO/LAMBDA codes to fit the 69-group format [12].

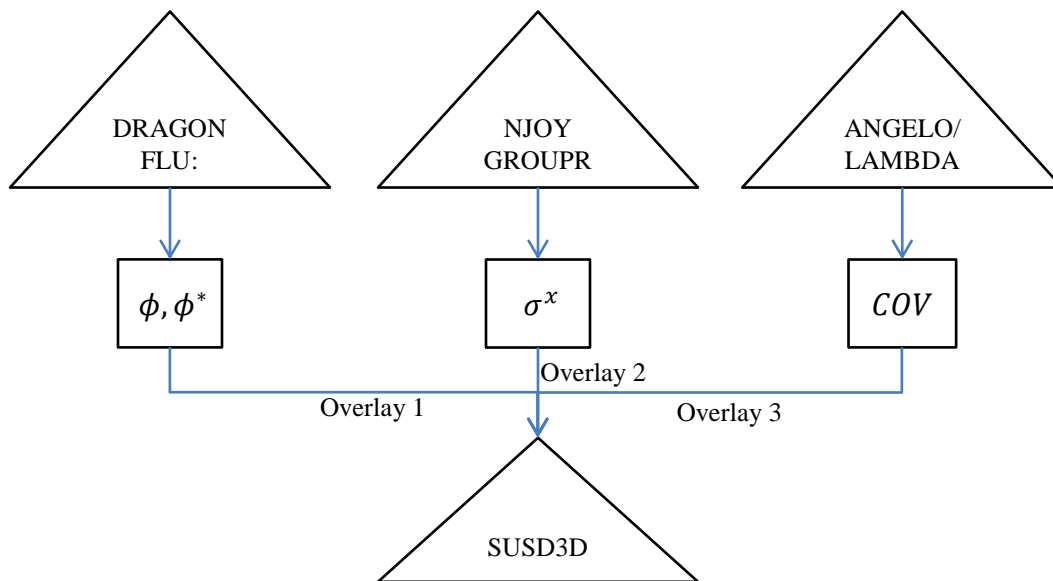


Figure 2: SUS3D calculation scheme

1.7.3 DONJON

The full core code DONJON (version 3.02 in this paper), also developed at École Polytechnique de Montréal, contains various models and numerical methods to solve the neutron multi-group diffusion equation [9]. This code, much like DRAGON, is also modular and uses the GAN generalized driver to link the modules together.

DONJON has the ability to import the properly formatted homogenized and condensed nuclear data files created by DRAGON, and use these data to solve for multi-group direct flux, adjoint flux and reactor multiplication constant, k_{eff} .

The geometry is initially tracked using the TRIVAT: module. Subsequently the TRIVAA: module is used to compute the finite element system matrices corresponding to the previously calculated tracking data. Finally the FLUD: module is used to calculate the solution to the eigenvalue problem [9], demonstrated in equation (1.48).

Chapter 2

ZED-2 Transport Calculations and S/U Analysis

2.1 Calculation Scheme

To keep within a sensible time frame, this model is completed in several stages. Each stage is computed with reasonable assumptions to cut down computation demand and time.

The ZEEP rod lattice was initially modeled in DRAGON (section 2.2). Using transport calculations the k_{∞} , direct/adjoint flux, and the homogenized cross sections were determined. The direct and adjoint flux values were then used in SUS3D to calculate the sensitivity coefficients of the isotopes and their reactions in the lattice, and further their uncertainty on the infinite lattice k_{∞} was determined.

The same calculations were subsequently performed for the (Th,Pu)O₂ bundle infinite lattice (section 2.3). Subsequent to the S/U analysis, the reaction rates of the most sensitive reactions were calculated and examined to illustrate the effects of voiding the coolant in the bundle infinite lattice.

Finally, the full ZED-2 core was modeled in DRAGON in 2D (section 2.4). Using similar calculation methods the sensitivity and uncertainty worth of the isotopes in the core were determined for four different full core cases.

2.2 ZEEP Rod Lattice

Figure 3 represents the ZEEP rod lattice composed of a single fuel pin containing natural uranium fuel and its surrounding moderator.

The DRAGON code operates by using various modules, each designed to perform a specific task. The material composition of the lattice and subsequently its geometry are the physical parameters initially defined in DRAGON.

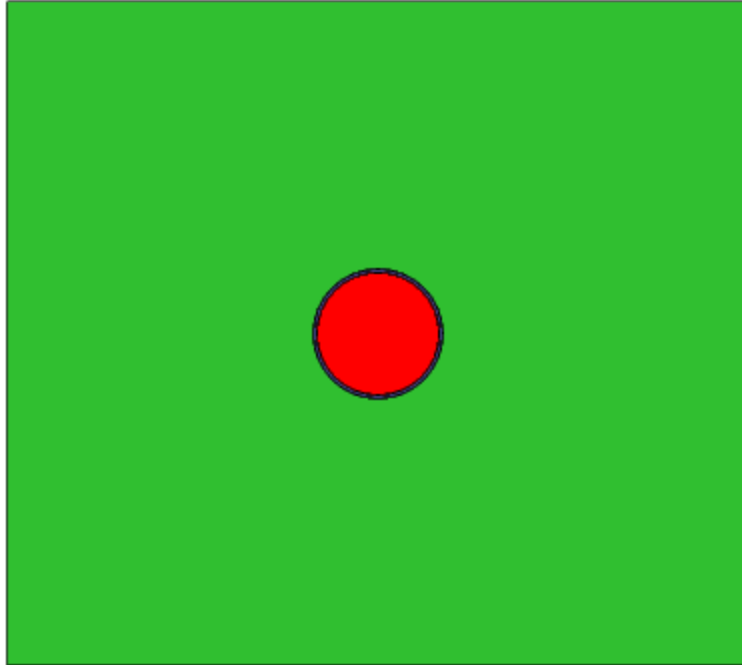


Figure 3: ZEEP rod lattice

2.2.1 Physical Parameters

The mixtures in the lattice are defined using the **LIB:** module. The module allows for a declaration of the library from which the cross-sections are to be chosen. Furthermore, the module presents various ways to use a transport correction to modify the cross-sections in the lattice. The effect of the transport correction on the total and isotropic scattering cross-sections will further be examined by comparing a case without transport correction with a case which uses transport correction.

The geometry of the lattice is defined using the **GEO:** module. To portray the results of an infinite lattice, the boundary conditions around the ZEEP rod lattice were chosen to be reflective. Two lattice geometries will be modeled and compared: a Cartesian lattice cell containing a circular fuel pin (Carcel geometry) within, and an annular type lattice.

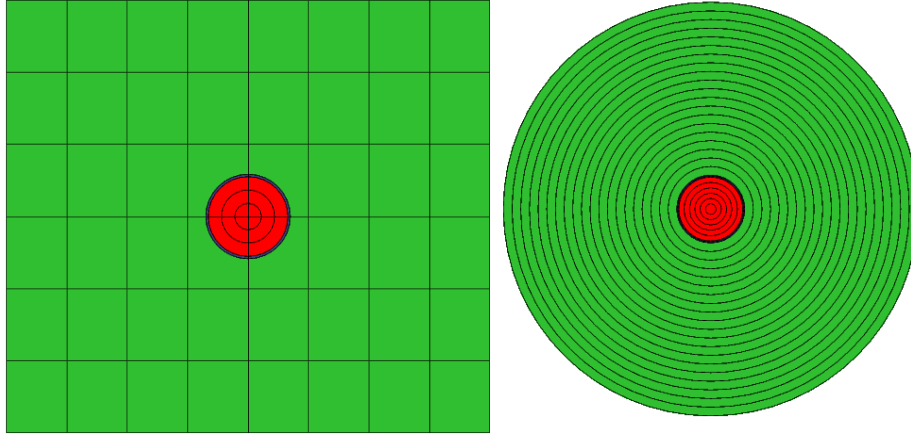


Figure 4: Cartesian (Carcel) geometry vs. annular geometry

2.2.2 Choice of Geometry

An Annular and Carcel geometry were modeled to observe the difference between their computation time and their results. To examine the two lattices the area between them must be conserved, hence the radius of the annular model was calculated using:

$$R_{annular} = \sqrt{\frac{A_{carcel}}{\pi}} \quad (2.64)$$

Both geometries used the same number of tracking lines with an equal density and both had the same meshing. With a very coarse meshing scheme, the Cartesian geometry calculates a k_{∞} of 1.2084 in 2 minutes while the annular geometry determines a k_{∞} of 1.2063 in less than 30 seconds.

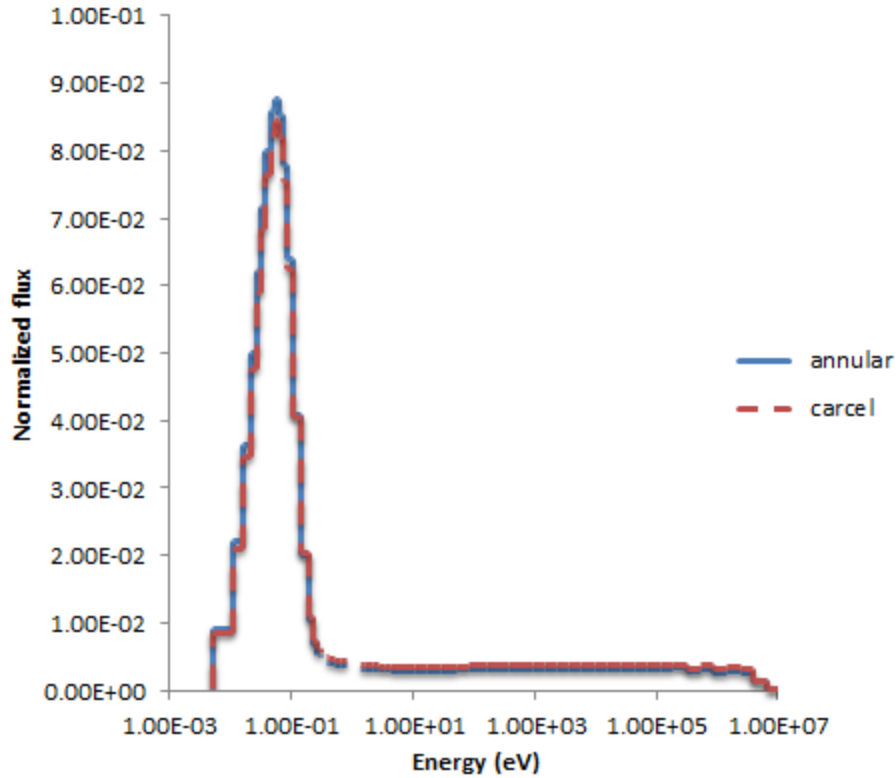


Figure 5: Flux spectrum of the annular and Cartesian ZEEP lattices

The difference between the two coarse geometries is approximately 3 mk and the computation times do not differ significantly. The annular case has a slightly lower computation time for two main reasons: The high symmetry present in the ring structure, and the reduction of variables in the collision probability calculations (reduces the spatial dimensions from 2D to 1).

As observed, the annular geometry shows a greater flux in the thermal region and a lower one in the fast region. This is expected as the annular geometry has a higher flux in the outer regions of the lattice due to the nature of its reflective boundary. Upon the strike of a neutron against the lattice boundary, a perpendicular collision with the tangent of the circular boundary will lead to the neutron bouncing back directly towards the center of the lattice; however a collision with a smaller angle can lead to the neutron traveling in an unrealistic polygon path around the circle, thus leading to a higher flux in the outer regions. Furthermore, the outer regions of the lattice are dominated by thermal neutrons due to the presence of the moderator, while the center, the fuel region, is dominated by fast neutrons. Hence, the integrated thermal flux is higher in the annular model.

As observed, there exist some physical differences between the two geometries. However, the advantage of a faster computation time becomes more pronounced as the spatial meshing of the models become finer. Thus, the annular geometry is advised if high degrees of spatial discretization is required, however the Cartesian geometry offers more accurate results.

2.2.3 Spatial Discretization

The spatial meshing used in the lattice is of great importance and requires, much like other parameters, an optimization between computation time and accuracy. To illustrate the method used to determine the optimal meshing, the effects of radial meshing on the fuel rod are first observed. Subsequently, the effects of Cartesian meshing of the moderator are analyzed.

| Radial subdivisions | k_{∞} | Calculation time |
|---------------------|--------------|------------------|
| 0 | 1.218515 | 1 minute |
| 2 | 1.218016 | 1 minute |
| 5 | 1.217555 | 1 minute |
| 9 | 1.217422 | 2 minutes |

Table 1: Effects of radial meshing on k_{∞} and computation time

The fuel's radial meshing is observed to have a small impact on the computation time and the k_{∞} of the lattice. As a result, the calculations were carried out using the five radial subdivisions model.

The moderator in the lattice has a much larger volume than the fuel rod, thus it is expected that the Cartesian meshing will have a more significant impact on the lattice multiplication constant. Though the higher number of subdivisions had very long computation times, the spatial meshing was brought to even smaller volumes to observe whether a spatial convergence can be reached in the lattice.

As observed the Cartesian meshing of the ZEEP rod lattice has a significant effect on the lattice k_{∞} and the computation time. Spatial convergence is observed to be reached at a 30x 30 discretization.

| J | Cartesian subdivisions | k_∞ |
|---|------------------------|------------|
| 1 | 0 | 1.217555 |
| 2 | 10x10 | 1.208477 |
| 3 | 15x15 | 1.207128 |
| 4 | 20x20 | 1.206517 |
| 5 | 25x25 | 1.206193 |
| 6 | 30x30 | 1.205981 |
| 7 | 35x35 | 1.20584 |
| 8 | 50x50 | 1.205651 |

Table 2: Effect of subdivisions on k_∞

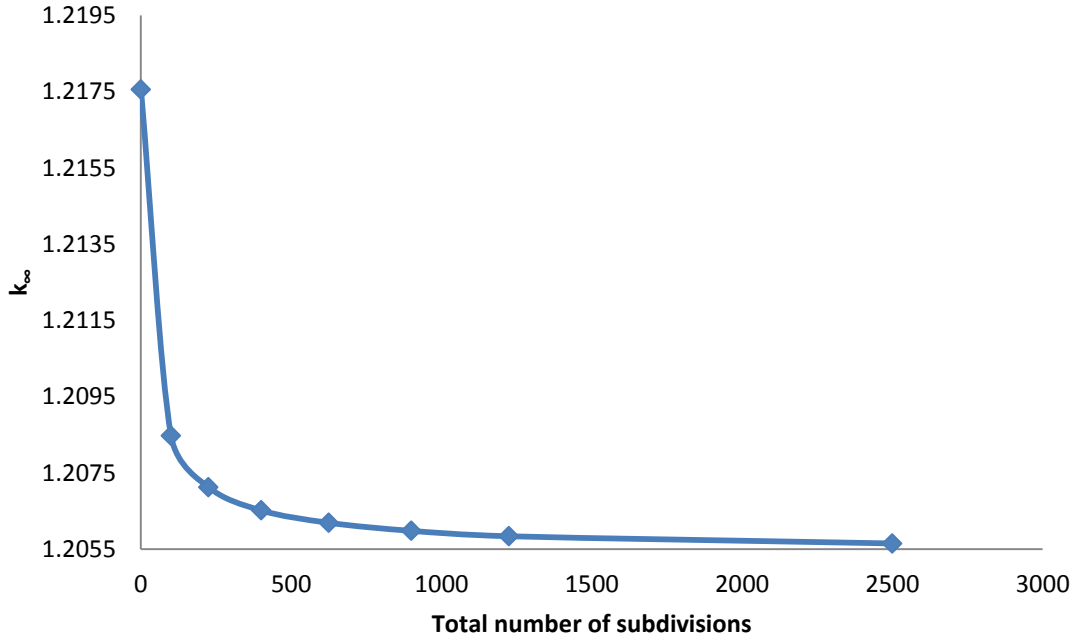


Figure 6: Spatial convergence of k_∞ in ZEEP lattice

2.2.4 Choice of Reflective Boundary Condition Type

DRAGON allows two types of reflective boundary conditions, white (isotropic) boundary conditions and specular (mirror-like) boundary conditions. The specular condition considers the boundary as a plane of symmetry, where the out-going flux is equal to the returning flux: $\phi(\vec{r}, E, \hat{\Omega}) = \phi(\vec{r}, E, \hat{\Omega}')$. The white boundary condition considers the returning flux to have an isotropic angular distribution. This approximation can be used

in the case of a symmetric plane, and while the condition leads to less demanding calculations, it is nevertheless an approximation. Both these options were analyzed for a ZEEP lattice case with very coarse meshing to preserve time.

| Boundary condition | k_{∞} | CPU time (minutes) |
|--------------------|--------------|--------------------|
| White (isotropic) | 1.21851 | 1 |
| Specular (mirror) | 1.21858 | 45 |

Table 3: Reflective boundary choice

As observed from table 4, even with a geometry containing no additional subdivisions, the specular boundary condition demands a high computation time. Although specular boundary conditions are the physically correct conditions, the large size of the moderator around the lattice leads to a large portion of the flux behaving isotropically in the outer regions of the lattice. It is for this reason that choosing between isotropic or mirror-like boundary conditions only affects the multiplication constant by 0.07 mk. However, the white boundary condition has a significantly shorter computation time and even though it is not the physically correct condition, it is a good approximation which leads to results that are very close to the physically correct, specular, boundary condition. Hence, the white boundary conditions were chosen for the lattice.

2.2.5 Resonance Self-Shielding

The effects of self-shielding were analyzed on the exact non-discretized geometry. DRAGON 3.05 uses the **SHI:** module to study the effects of self-shielding of resonant isotopes within a specific geometry. The module uses the generalized Stamm'ler method presented in 1.4.1.1. Two different methods of self-shielding calculations were applied to observe their differences on the lattice multiplication constant.

The option LJ commands the code to use the Livolant-Jeanpierre normalization scheme (also presented in 1.4.1.1). DRAGON disables this command by default since the NOLJ option, the opposite of the LJ option, is found to give more accurate results for CANDU cores [30]. The following table illustrates the effects of this option on the ZEEP rod lattice.

The difference between the two self-shielding calculation options is not negligible, and is proved to have a large impact on the multiplication constant of the ZEEP rod lattice.

| Normalization option | k_{∞} |
|----------------------|--------------|
| LJ | 1.228325 |
| NOLJ | 1.218515 |
| $\Delta\rho$ | 9.81 mk |

Table 4: Effect of Livolant-Jeanpierre normalization

Furthermore, since a large portion of the full core is composed of these ZEEP lattices, this large effect is also expected to be observed upon the 3D full core calculations. Therefore, the effect and accuracy of the Livolant- Jeanpierre normalization scheme will further be analyzed upon examining the results from DONJON in chapter 3.

2.2.6 Energy Condensation and Homogenization

To produce reasonable macroscopic cross section libraries for further use in DONJON, it is important to select an accurate method of condensing the energy groups and the regions within the lattice.

Two-group condensation was done by splitting the energy groups into thermal and fast regions. Energy groups were stored in one group below 0.625 eV and the other above it. Furthermore, using FVW calculations the homogenized macroscopic cross sections were calculated. As discussed in the introduction, each specific case ran in the ZED-2 reactor was characterized by a specific moderator height. Therefore, while a large portion of the ZEEP rods were submerged in the moderator, parts of them were not. To simulate this effect, two different libraries were created from the ZEEP rod lattice: One library which homogenized the fuel, cladding and moderator and the other which homogenized only the fuel and the cladding, excluding the moderator to simulate the ZEEP rods which were not submerged in the moderator.

2.2.7 ZEEP Rod Lattice Sensitivity

The modified version of SUSD3D code was used to perform sensitivity/uncertainty

analysis based on the first-order perturbation theory, where the sensitivity coefficients were derived from the direct and adjoint flux moments calculated by the **FLU:** module in DRAGON.

The sensitivity coefficients presented in table 5 represent the change in k_{∞} resulting from a 1% change in the corresponding cross section. A positive sensitivity coefficient leads to an increase in the k_{∞} when changes in Σ_{rx} are positive. Inversely, a negative sensitivity coefficient leads to a decrease in k_{∞} when changes in Σ_{rx} are positive.

SUSD3D calculated the sensitivity coefficient of various reactions in various isotopes in 69 groups. Energy integrated sensitivity coefficients were calculated as well. The following table illustrates the energy integrated sensitivity coefficients in a decreasing order. Energy Group-wise sensitivity coefficients were also plotted for some of the reactions with the highest integrated sensitivity coefficients.

| Nuclide Reaction | S_I |
|---------------------------------|-----------|
| $^{235}\text{U} (\bar{\nu})$ | 9.37E-01 |
| ^{235}U (Fission) | 4.42E-01 |
| ^{238}U (n, γ) | -4.09E-01 |
| ^{235}U (n, γ) | -8.64E-02 |
| $^{238}\text{U} (\bar{\nu})$ | 6.35E-02 |
| ^{238}U (Fission) | 3.54E-02 |
| ^1H (n, γ) | -2.31E-02 |
| ^{16}O (n,elas) | 7.78E-03 |
| ^{16}O (n, α) | -3.05E-03 |
| ^1H (n,elas) | 2.88E-03 |
| ^{16}O (n, γ) | -1.19E-03 |
| ^{238}U (n,elas) | 1.26E-04 |
| ^{235}U (n,elas) | 2.18E-06 |

Table 5: Energy integrated sensitivity coefficients

As expected, $^{235}\text{U} (\bar{\nu})$ has the highest integrated sensitivity coefficient. This is to be expected as $(\bar{\nu})$ is directly proportional to k_{∞} and is used as a normalization factor. [11], [12]

To justify the descending order of the subsequent three reactions, ^{235}U (fission), ^{238}U (n, γ) and ^{235}U (n, γ), three parameters must be analyzed: ϕ , ϕ^* , and Σ_{RX}^g , where RX is a specific reaction in energy group g . The three isotopes are all within the fuel, and have their highest sensitivity coefficients occurring in the same, thermal, region of the energy spectrum. Therefore, all three reactions will be affected by equal values of ϕ and ϕ^* , leaving Σ_{RX}^g as the only parameter differing between the three reactions.

Figure 7 illustrates the difference between the three microscopic cross sections, where the ^{235}U - $\sigma(n, f)$ is observed to be two orders of magnitude higher than ^{238}U - $\sigma(n, \gamma)$ in the thermal region. However, the absolute integrated sensitivity coefficients are observed to have the same magnitude. This is justified by the fact that the density of ^{238}U is two orders of magnitude higher than the density of ^{235}U in the fuel, thus the macroscopic cross sections of the two isotopes have equal magnitudes in the fuel. Moreover, while ^{235}U - $\sigma(n, \gamma)$ is one order of magnitude higher than ^{238}U - $\sigma(n, \gamma)$, $\Sigma(n, \gamma)$ of ^{235}U is one order of magnitude lower than the $\Sigma(n, \gamma)$ of ^{238}U ; thus the integrated sensitivity coefficient of ^{238}U (n, γ) is one order of magnitude higher than ^{235}U (n, γ).

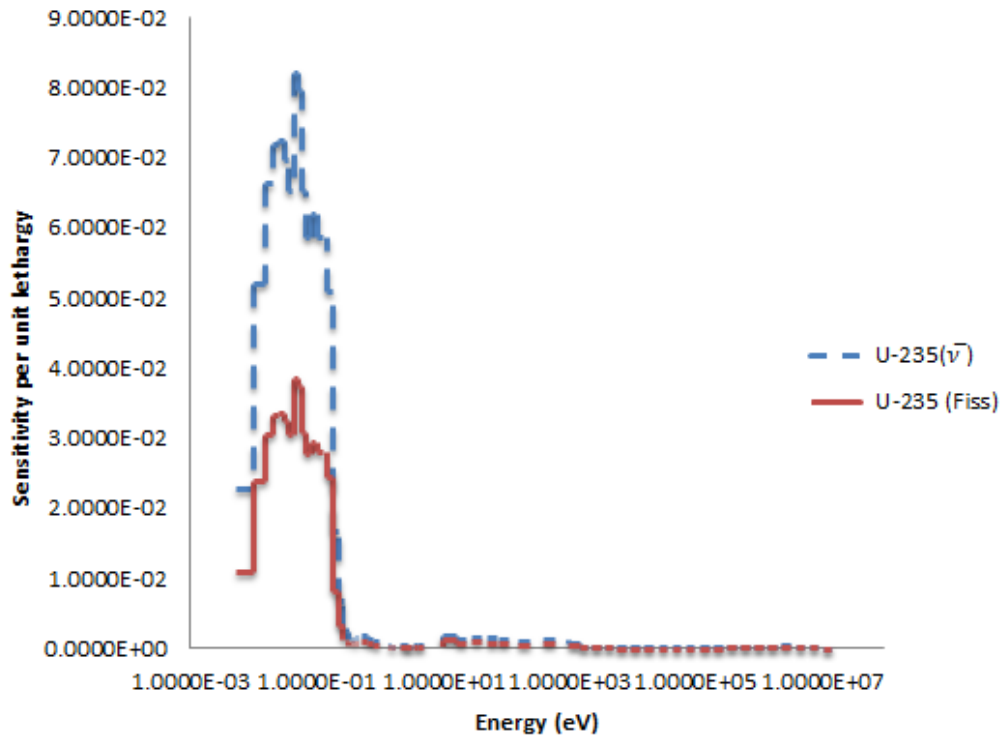


Figure 7: Group-wise ^{235}U $\bar{\nu}$ ($S_I=0.937$) and ^{235}U fission ($S_I=0.442$) sensitivity profiles in the ZEEP lattice

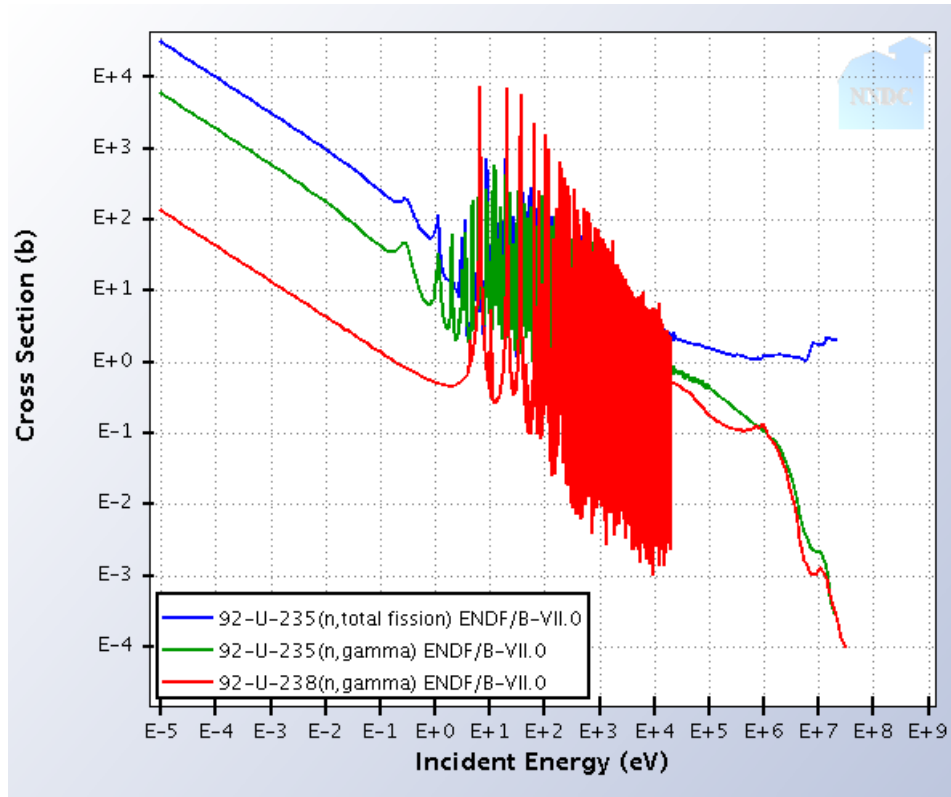


Figure 8: ENDF/B-VII.0 group wise microscopic cross section data for ^{235}U (n,f), ^{235}U (n, γ), ^{238}U (n, γ)

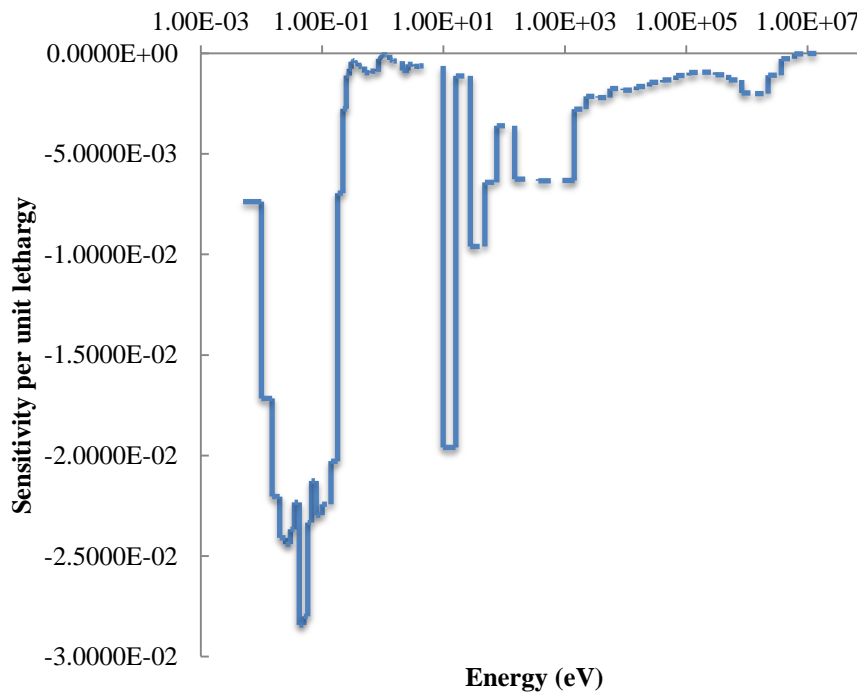


Figure 9: Group-wise ^{238}U (n, γ) sensitivity ($S_I = -0.409$) profile in the ZEEP lattice

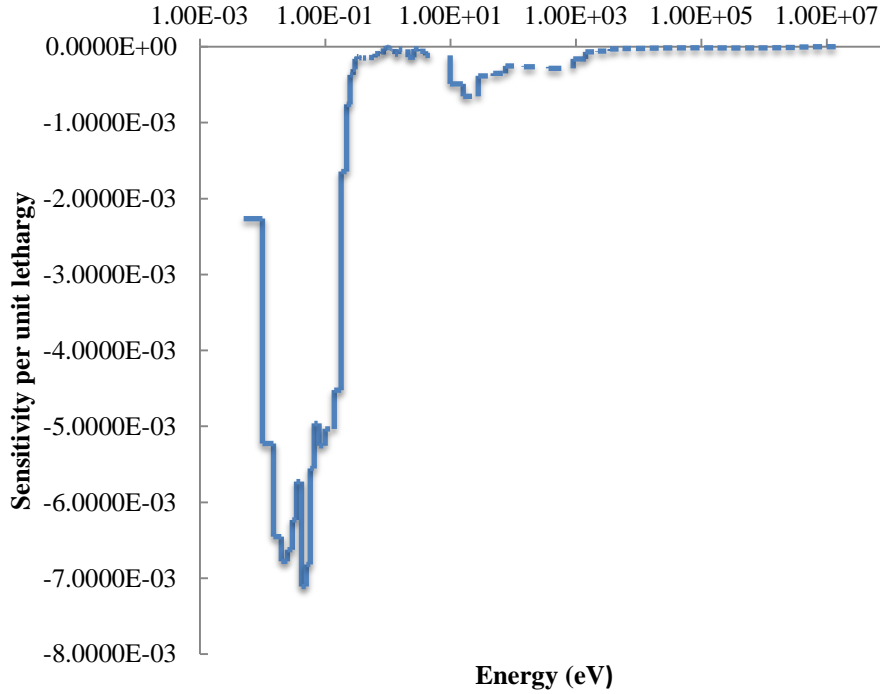


Figure 10: Group-wise ^{235}U (n, γ) sensitivity ($S_I = -8.64 \times 10^{-2}$) profile in the ZEEP lattice

2.2.8 ZEEP Rod k_∞ Uncertainty

ANGELO/LAMBDA was used to create 69-group covariance matrices from the 44-group covariance matrices of SCALE 6 [12], and the uncertainty in k_∞ due to uncertainties in the nuclear data was calculated using equation (1.64). It is important to note the two factors playing a role in k_∞ uncertainty: the sensitivity of the specific reaction in question, and its respective covariance. Table 6 presents the 5 highest contributors to k_∞ uncertainty with their corresponding standard deviations in mk and their percentage contributions to the total variance in the lattice cell.

| Nuclide Reaction | $\sigma_k(\text{mk})$ | V% | S_I |
|-----------------------------------|-----------------------|------|-----------|
| ^{238}U (n, γ) | 7.62 | 83.7 | -4.09E-01 |
| ^{235}U ($\bar{\nu}$) | 2.88 | 11.9 | 9.37E-01 |
| ^{16}O (n, α) | 1.01 | 1.9 | -3.05E-03 |
| ^{235}U (Fission) | 0.87 | 1.1 | 4.42E-01 |
| ^{235}U (n, γ) | 0.71 | 0.68 | -8.67E-02 |
| Total k_∞ uncertainty (mk) | | 8.36 | |

Table 6: Reaction uncertainties in the ZEEP rod, where S_I represents the integrated sensitivity and V% represents the percentage contribution to total variance

^{238}U (n,γ) displays the highest uncertainty on k_∞ in the lattice, even though it has a lower integrated sensitivity than ^{235}U ($\bar{\nu}$) and ^{235}U (Fission). This proves that the uncertainty lies chiefly in the ^{238}U (n,γ) cross section data. Furthermore, even though ^{235}U ($\bar{\nu}$) and ^{235}U (Fission) have the two highest integrated sensitivities in the lattice, they only contribute a total of 13.0% to the k_∞ uncertainty. This illustrates that the two reactions have better known nuclear data. The ^{16}O (n,α) reaction is observed to have a slightly higher contribution to k_∞ uncertainty than ^{235}U (Fission) even though its integrated sensitivity is approximately two orders of magnitude lower. This illustrates that, similar to ^{238}U (n,γ), the main portion of this reaction's uncertainty contribution comes from the uncertainty in its cross section data.

2.3 (Th, Pu)O₂ Bundle Lattice

The second DRAGON model created simulates the central (Th, Pu)O₂ bundle. Having the same lattice dimensions as the ZEEP rod lattice, the (Th, Pu)O₂ lattice consisted of a Bruce-designed 36 element bundle, supported by an aluminum central tube.

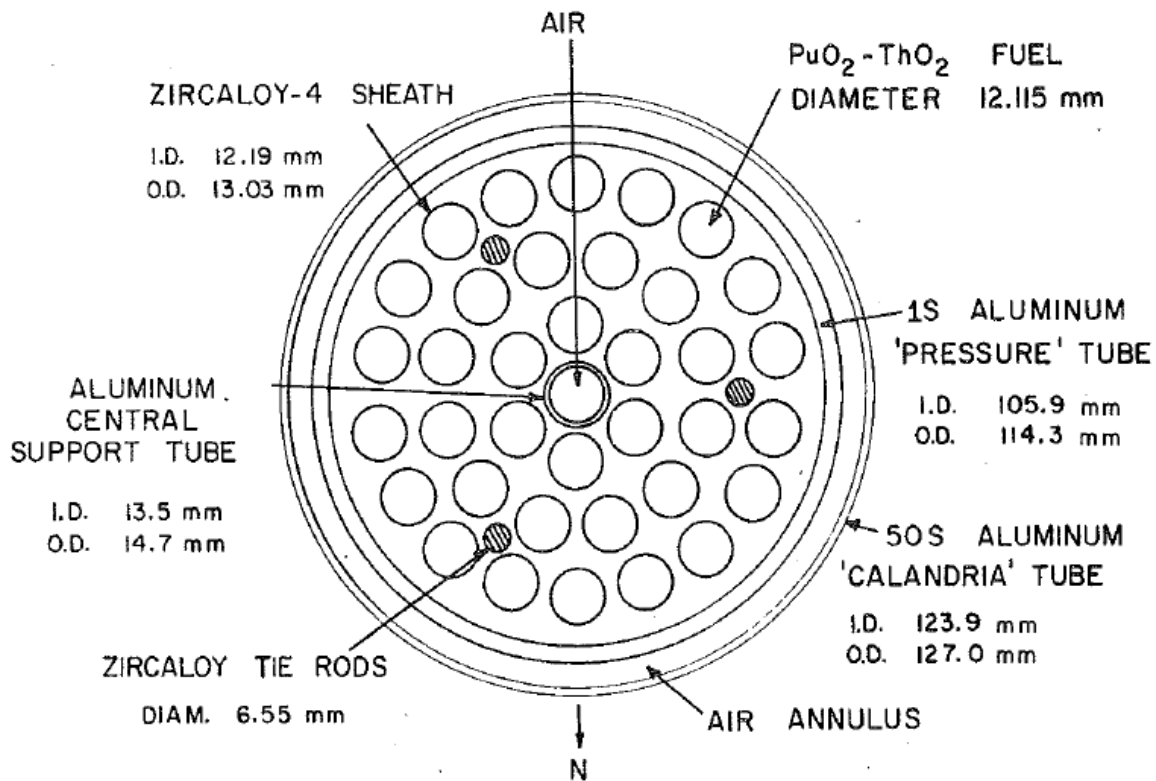


Figure 11: (Th,Pu)O₂ central bundle [7]

Using a similar process as the ZEEP lattice in the previous section, the **LIB:** module was first used to declare the mixtures in the lattice while the **GEO:** module was used to describe its geometry.

Subsequently the collision probability matrices were determined, and using these matrices the direct and adjoint flux values, and the lattice multiplication constant were calculated. The direct and adjoint flux values were used as inputs for the SUS3D code to calculate the sensitivity coefficients using first order perturbation theory. Furthermore, using the ENDF/B-VII library as an input for NJOY, the covariance matrices were calculated and fed into the SUS3D code for uncertainty calculations. The modeling, however, began with the analysis of two potential geometries for the bundle.

2.3.1 Choice of Geometries

Two geometry options, Cartesian and annular, were modeled to determine the most accurate and timely efficient choice. As mentioned in the previous chapter, the Cartesian model is indeed the model which is physically closest to reality. However due to its lower order of symmetry and its higher number of variables (two Cartesian variables x and y relative to 1 radial variable, r , in the annular geometry) the Cartesian model is expected to have a much longer computation time.

Using equation (2.64) the radius of the annular model is calculated such that the areas between the two geometries were conserved. Furthermore, it is important to pick a fine meshing for the integration lines, so that they cross every region in the lattice. As observed from figure 12 the annular geometry has a 6-fold rotational symmetry, thus the number of angles for the integration lines, n_{angle} , was chosen to be 8 with a density, d_{lines} , of 200 cm^{-1} . The Cartesian geometry does not have the 6-fold rotational geometry and thus 48 angles are needed to create a fine meshing for its integration lines.

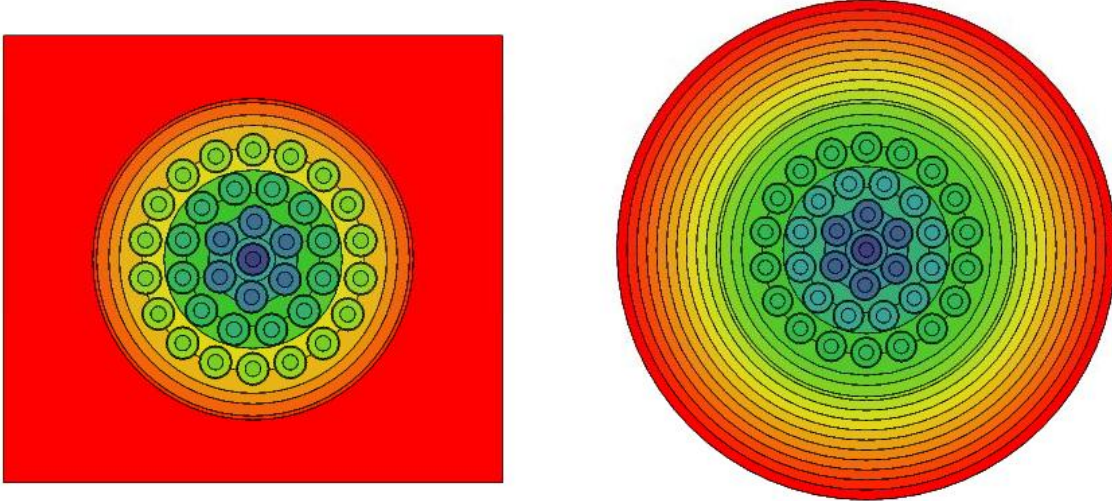


Figure 12: Cartesian (left) and annular (right) geometries of the (Th,Pu)O₂ bundle

| | N_{angle} | d_{lines} (cm ⁻¹) | k_{∞} | Computation time (minutes) |
|--|-------------|---------------------------------|--------------|----------------------------|
| Carcel | 48 | 200 | 1.03716 | 8 |
| Annular | 8 | 200 | 1.03739 | 2 |
| $\Delta\rho$ 0.23 mk | | | | |

Table 7: k_{∞} and computation times of Annular vs. Cartesian bundle geometries

As observed the differences between the two cases in terms of computation time and k_{∞} is very small with a coarse meshing. Thus, the Cartesian geometry was chosen due to the fact that it has a more physically accurate representation of the lattice and does not have a much larger computation time than the annular geometry given a coarse meshing.

2.3.2 Water and Air Cooled Bundles

Two individual experiments were performed in the ZED-2 reactor, one where the central (Th, Pu)O₂ bundles were cooled, and the other where the bundles were voided. Therefore, an air cooled bundle was also modeled in DRAGON to simulate the coolant voided cases. By comparing the two types of lattices, one should be able to calculate the Coolant Void Reactivity (CVR) worth of the lattice. However, it should be noted that the CVR worth of the infinite lattice will not necessarily dictate the CVR worth of the full core, due to the added dimension in the DONJON model, along with the ZEEP rods and a more

heterogeneous surrounding. The table below represents the respective k_{∞} values of the two cases, along with the CVR worth of the lattice, calculated using:

$$\rho_{1 \rightarrow 2} = \frac{1}{k_{cooled}} - \frac{1}{k_{voided}}$$

| | k_{∞} |
|--|--------------|
| Cooled (Th, Pu)O₂ bundle | 1.03716 |
| Voided (Th, Pu)O₂ bundle | 1.004680 |
| CVR | -31.17 mk |

Table 8: Coolant Void Reactivity of (Th,Pu)O₂ infinite lattice

Contrary to a typical CANDU lattice, it is observed that the (Th, Pu)O₂ bundle has a large negative CVR. This is explained by observing the flux spectra of the cooled and voided lattices. The voided lattice is observed to have a far lower concentration of neutrons in the thermal region, and a larger amount of neutrons in the fast region. This illustrates the fact that the coolant was also acting as an effective moderator in the lattice. The lower number of thermal neutrons will affect the fission rates within the lattice, whose major contributor is ²³⁹Pu. The ²³⁹Pu fission cross section shows a slight increase followed by sharp decrease at approximately 0.1 – 1 eV. Without moderated thermal neutrons, the fission rate in the lattice is greatly reduced. Therefore, the reactivity of the lattice is decreased as the coolant is removed.

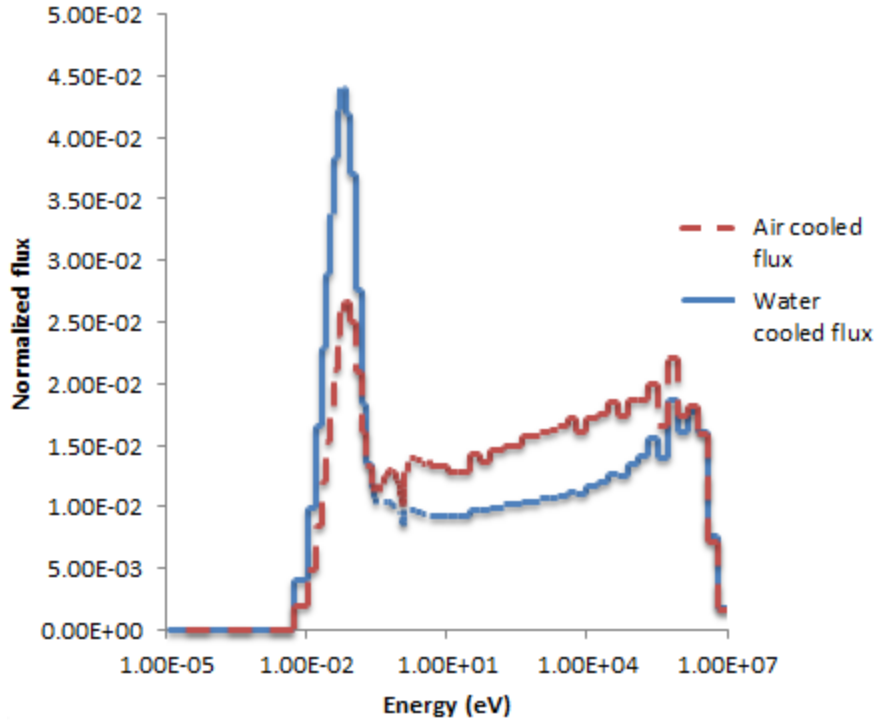


Figure 13: Flux spectra of the cooled and voided lattices

It is also interesting to note the differences between the (Th, Pu)O₂ lattice energy spectrum, figure 13, and the ZEEP lattice energy spectrum, figure 5. As observed from table 9, the fissile isotopes in the (Th,Pu)O₂ bundle lattice fuel all have strong σ_f values in the thermal region of the spectrum; furthermore, the strongest contributor to fission in the bundle lattice, ²³⁹Pu, has a higher neutron fission yield, $\bar{\nu}$, than the strongest fission contributor in the ZEEP lattice, ²³⁵U. Thus there is a higher concentration of fast neutrons from the fissile isotopes in the bundle lattice.

Due to the presence of a strong absorber in the thermal region, ²³²Th, the bundle lattice has high absorption in the thermal region; therefore its energy spectrum in the thermal region is observed to be half the value of the ZEEP lattice's thermal spectrum. Moreover, the bundle lattice is relatively under-moderated due to its lower fuel to moderator volume ratio relative to the ZEEP rod lattice. This leads to a higher concentration of fast neutrons and a lower concentration of thermal neutrons.

| Fuel composition | (Th, Pu)O ₂ lattice | ZEEP lattice |
|---|--------------------------------|--------------|
| ¹⁶ O | 12.41% | - |
| ²³² Th | 86.051% | - |
| ²³⁸ Pu | 0.002% | - |
| ²³⁹ Pu | 1.181% | - |
| ²⁴⁰ Pu | 0.303% | - |
| ²⁴¹ Pu | 0.045% | - |
| ²⁴² Pu | 0.008% | - |
| ²³⁴ U | - | 0.005% |
| ²³⁵ U | - | 0.711% |
| ²³⁸ U | - | 99.284% |
| Fuel density [g/ cm³] | 9.46 | 19.05 |

Table 9: Isotopic concentrations of (Th, Pu)O₂ bundle lattice and the ZEEP rod lattice

2.3.3 Spatial Discretization

To choose the correct spatial meshing, one structure of the bundle was spatially subdivided while the other elements (coolant, moderator, fuel elements and etc...) were fixed. It was found that the optimal choice for the meshing in each rod is splitting each fuel rod into two annular regions. In this section, the optimal choice for coolant and moderator spatial meshing within the bundle lattice is studied.

Subdividing the coolant region is expected to have a significant impact on the lattice multiplication constant. As observed in figure 14, DRAGON treats each individual region as a homogenous volume with a constant flux. Thus, having no subdivisions in the coolant region dictates a constant flux throughout the coolant, which is an assumption that leads to a higher integrated flux value than the various flux values within the coolant. Having no subdivisions, though computationally quicker in this case, results in a multiplication constant that is higher than the true k_{∞} of the bundle lattice. Subsequently, the effect of subdividing the moderator was analyzed as well. However, its effect on the bundle lattice k_{∞} was observed to be too low to sacrifice the added computation time.

| Using a constant moderator subdivision of 0 | | |
|---|------------------------|--------------|
| Coolant subdivisions: | Number of subdivisions | k_{∞} |
| | 1 | 1.055567 |
| | 2 | 1.051951 |
| | 3 | 1.042425 |
| | 4 | 1.038933 |
| | 5 | 1.037104 |
| Using a constant coolant subdivision of 5 | | |
| Moderator subdivisions: | Number of subdivisions | k_{∞} |
| | 1 | 1.037233 |
| | 2 | 1.037438 |
| | 3 | 1.037521 |
| | 4 | 1.037560 |
| | 5 | 1.037580 |

Table 10: Effects of moderator and coolant spatial subdivisions

As observed, spatial subdivisions of the moderator had a very small impact, $< 1\text{mk}$, on the lattice while the coolant subdivisions decreased the reactivity by 18.4 mk. Thus, the final bundle lattice contained two subdivisions in the fuel elements, five subdivisions in the coolant and no subdivisions in the moderator region.

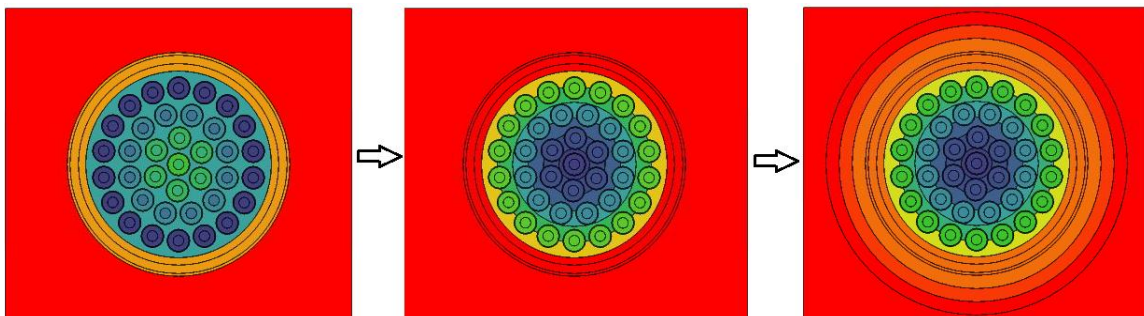


Figure 14: Energy integrated flux of the bundle lattice with 0 coolant and moderator subdivisions (left), with 5 coolant and 0 moderator subdivisions (center), with 5 coolant and 5 moderator subdivisions (right)

2.3.4 Energy Condensation and Homogenization

Simulating the full core in 3D using DONJON requires that all the homogenized macroscopic cross section libraries have the same energy meshing. Therefore, the bundle lattice was condensed using the same energy subdivisions as the ZEEP lattice; where three individual libraries containing 2-group cross sections were computed.

Due to the finer nature of the bundle, it was determined that a finer homogenized structure was needed than the ZEEP lattice. Using the Super Homogenization technique, each bundle was transformed into a 4x 4 Cartesian cell, where the central 4 cells contain the homogenized fuel and cladding structure cross sections, and the outer 4 cells contain the homogenized moderator cross sections. This scheme allows for a finer meshing, as well as allowing the user to remove the outer moderator to simulate the bundles that are above the critical moderator height in the 3D model. Both the air cooled and water cooled bundles were homogenized using the aforementioned method.

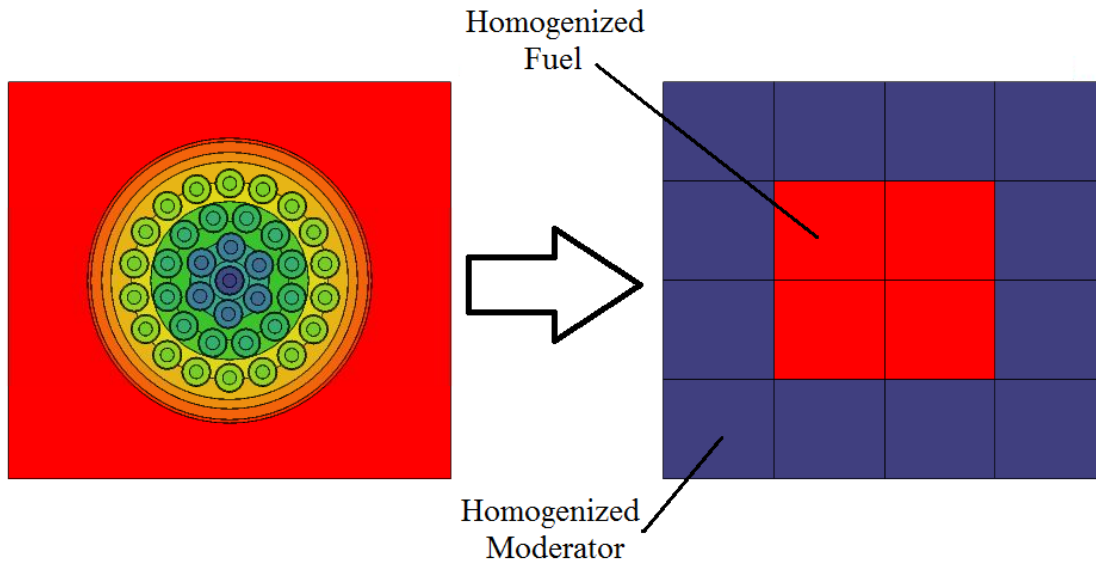


Figure 15: Homogenization scheme of the (Th,Pu)O₂ bundle

2.3.5 (Th,Pu)O₂ Bundle Lattice Sensitivity

k_{∞} sensitivity and uncertainty analysis with respect to cross section data for isotopes present in the bundle was performed. Using the same methodology as the ZEEP lattice sensitivity/uncertainty analysis, the forward and adjoint flux vectors were computed by

DRAGON in 69 groups, and subsequently used by SUS3D to generate sensitivity coefficients using first order perturbation theory.

The integrated sensitivity (S_i) coefficients of the air-cooled and the water-cooled bundles are presented in the table below in descending significance. Furthermore, the sensitivity coefficients corresponding to each energy group and associated with a specific reaction of an isotope are used to examine the integrated sensitivity coefficients.

Finally, using the law of error propagation the uncertainty worth of each reaction is examined and the total uncertainty on the lattice k_∞ is calculated.

As observed from table 9, the top 5 most sensitive reactions in the air-cooled and water-cooled bundles correspond to the isotopes in the (Th,Pu) O_2 fuel and furthermore, 3 of these 5 reactions are ^{239}Pu reactions: $^{239}\text{Pu}(\bar{\nu})$, ^{239}Pu (fission) and $^{239}\text{Pu}(n,\gamma)$. ^{239}Pu has the highest relative weight percentage and is the largest contributor to fission. Therefore, its average neutron yield has the most direct effect on the bundle multiplication constant.

As observed the integrated sensitivity coefficients differ between the two types of bundles. An increase is observed in all the capture reaction integrated sensitivity coefficients in the fuel isotopes except ^{238}Pu , while fission reactions sensitivity coefficients all increase, without an exception, upon voiding the bundle. As observed from figure 13, the flux spectra of both bundles show that the air-cooled bundle has a lower concentration of thermal neutrons due to the fact that the coolant was also acting as a moderator. Due to the lower amount of thermal neutrons available in the air-cooled bundle, the $^{239}\text{Pu}(\bar{\nu})$ has a lower integrated sensitivity coefficient than the water-cooled bundle.

^{232}Th capture is observed to play a more significant role in the air-cooled bundle than the water-cooled bundle. ^{232}Th has a notable (n,γ) cross-section in the fast region of the spectrum, and as already mentioned, without the coolant also acting as a moderator, there is a significant amount of fast neutrons available in the air-cooled bundle, and thus the integrated sensitivity of $^{232}\text{Th}(n,\gamma)$ is observed to be higher in the air cooled bundle.

As expected, the water-cooled bundle is more sensitive to ^1H reactions and this is due to the fact that there is a higher concentration of ^1H in the water-cooled bundle, thus leading to a larger macroscopic cross section for both elastic scattering and capture. It is also interesting to note that ^1H elastic scattering plays a more important role in the bundles

| Water-cooled bundle | | Air-cooled bundle | |
|------------------------------------|-----------|------------------------------------|-----------|
| Isotopes and reactions | S_I | Isotopes and reactions | S_I |
| $^{239}\text{Pu} (\bar{\nu})$ | 9.53E-01 | $^{239}\text{Pu} (\bar{\nu})$ | 9.51E-01 |
| ^{239}Pu (Fission) | 5.49E-01 | ^{239}Pu (Fission) | 5.49E-01 |
| $^{232}\text{Th}(n, \gamma)$ | -2.92E-01 | $^{232}\text{Th} (n, \gamma)$ | -3.48E-01 |
| $^{239}\text{Pu} (n, \gamma)$ | -1.91E-01 | $^{239}\text{Pu} (n, \gamma)$ | -1.95E-01 |
| $^{240}\text{Pu} (n, \gamma)$ | -6.02E-02 | $^{240}\text{Pu} (n, \gamma)$ | -6.13E-02 |
| $^1\text{H} (n, \text{elas})$ | 5.21E-02 | $^{241}\text{Pu} (\bar{\nu})$ | 4.69E-02 |
| $^{241}\text{Pu} (\bar{\nu})$ | 4.53E-02 | ^{241}Pu (Fission) | 2.73E-02 |
| $^1\text{H} (n, \gamma)$ | -4.53E-02 | $^{16}\text{O}(n, \text{elas})$ | 9.34E-02 |
| ^{241}Pu (Fission) | 2.65E-02 | ^{232}Th (Fission) | -6.55E-03 |
| $^{241}\text{Pu} (n, \gamma)$ | -6.47E-03 | $^{241}\text{Pu} (n, \gamma)$ | -6.53E-03 |
| ^{232}Th (Fission) | -5.30E-03 | $^1\text{H}(n, \text{elas})$ | 3.17E-03 |
| $^{16}\text{O} (n, \text{elas})$ | -3.98E-03 | $^{232}\text{Th} (n, \text{elas})$ | 2.04E-03 |
| $^{240}\text{Pu} (\bar{\nu})$ | 1.21E-03 | $^{240}\text{Pu} (\bar{\nu})$ | 1.68E-03 |
| ^{240}Pu (Fission) | 8.21E-04 | $^1\text{H}(n, \gamma)$ | -1.29E-03 |
| $^{238}\text{Pu} (n, \gamma)$ | -3.16E-04 | ^{240}Pu (Fission) | 1.16E-03 |
| $^{16}\text{O} (n, \gamma)$ | -1.59E-04 | $^{238}\text{Pu} (n, \gamma)$ | -2.88E-04 |
| $^{242}\text{Pu} (n, \gamma)$ | -1.08E-04 | $^{242}\text{Pu} (n, \gamma)$ | -1.62E-04 |
| $^{232}\text{Th}(n, \text{elas})$ | -6.85E-05 | $^{16}\text{O}(n, \gamma)$ | -1.45E-04 |
| $^{238}\text{Pu} (\bar{\nu})$ | 4.91E-05 | $^{238}\text{Pu} (\bar{\nu})$ | 6.54E-05 |
| ^{238}Pu (Fission) | 3.23E-05 | ^{238}Pu (Fission) | 4.54E-05 |
| $^{242}\text{Pu} (\bar{\nu})$ | 2.47E-05 | $^{242}\text{Pu} (\bar{\nu})$ | 3.34E-05 |
| ^{242}Pu (Fission) | 1.69E-05 | $^{240}\text{Pu} (n, \text{elas})$ | 2.48E-05 |
| $^{240}\text{Pu} (n, \text{elas})$ | 2.75E-06 | ^{242}Pu (Fission) | 1.77E-05 |
| $^{239}\text{Pu} (n, \text{elas})$ | -1.57E-06 | $^{238}\text{Pu} (n, \text{elas})$ | -1.74E-05 |
| $^{241}\text{Pu} (n, \text{elas})$ | -8.89E-09 | $^{239}\text{Pu}(n, \text{elas})$ | -9.36E-06 |
| $^{238}\text{Pu} (n, \text{elas})$ | -2.61E-09 | $^{241}\text{Pu} (n, \text{elas})$ | -1.18E-07 |
| $^{242}\text{Pu} (n, \text{elas})$ | -2.10E-09 | $^{242}\text{Pu} (n, \text{elas})$ | -2.50E-08 |

Table 11: Air cooled and water cooled (Th,Pu)O₂ bundle integrated sensitivity coefficients

than ^1H capture, which further emphasizes the moderating role of the coolant, and explaining the largely negative CVR.

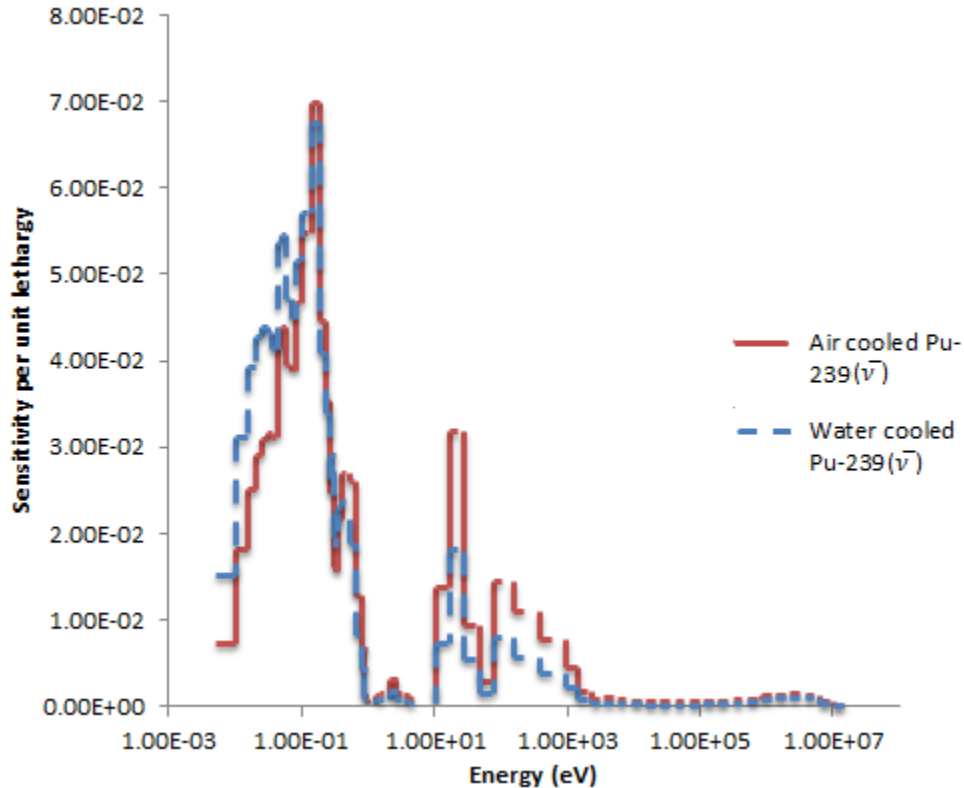


Figure 16: Air cooled vs. water cooled bundle group-wise sensitivity profiles of $^{239}\text{Pu} (\bar{\nu})$ ($S_{I,A.C.}= 0.951, S_{I,W.C.}=0.953$)

As observed from figure 16 the group-wise sensitivity of $^{239}\text{Pu} (\bar{\nu})$ is lower in the energy groups below 0.14 eV in the air-cooled bundle, while higher in the faster groups. This is due to the fact that though the value of $(\bar{\nu})$ does not change significantly between the two cases, in the air-cooled case most of the occurring fission reactions are in the fast region thus leading to a heightened sensitivity to average fission yield, $(\bar{\nu})$, in that energy range. The sensitivity of $^{232}\text{Th} (n, \gamma)$ in the water-cooled bundle is observed to have a lower sensitivity than the air-cooled bundle in energy regions greater than approximately 0.02 eV. The increase in sensitivity of $^{232}\text{Th} (n, \gamma)$ upon voiding the bundle is due to the fact that the direct average flux in the fuel pins is higher in energy regions above 0.02 eV in the voided case, while the adjoint flux remains similar between the two cases.

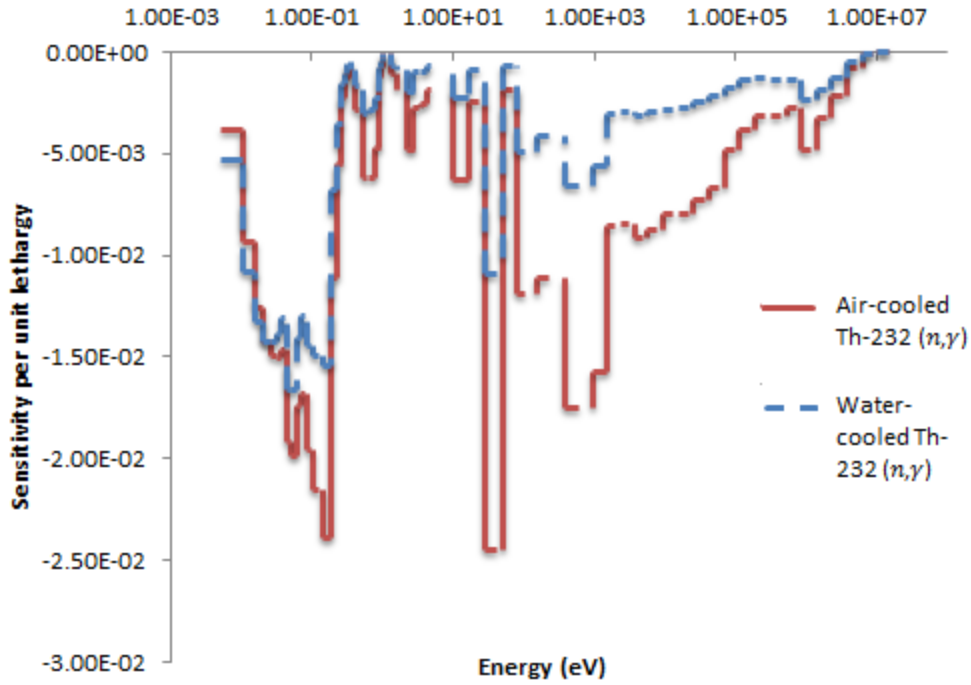


Figure 17: Air cooled vs. water cooled bundle group-wise sensitivity profile of ^{232}Th (n, γ) ($S_{I,A.C.} = -0.348$, $S_{I,W.C.} = -0.292$)

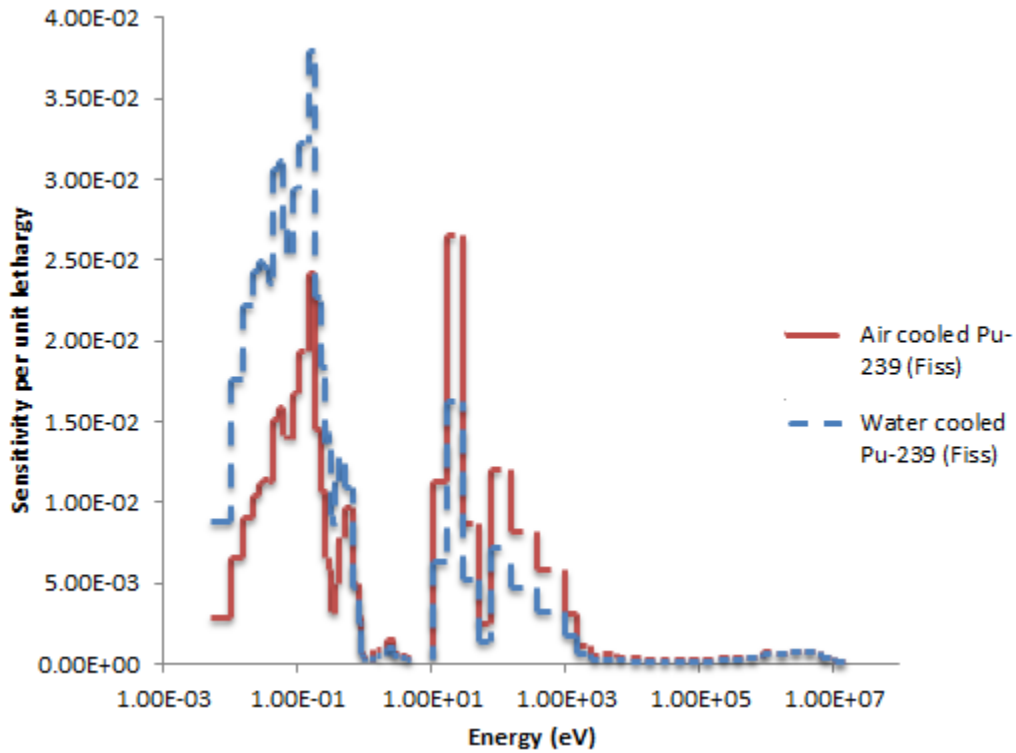


Figure 18: Air cooled vs. water cooled bundle group-wise sensitivity plot of ^{239}Pu (Fiss) ($S_{I,A.C.} = 0.549$, $S_{I,W.C.} = 0.549$)

The sensitivity to ^{239}Pu (Fission) is observed to be greater in energy regions above 0.5 eV in the air-cooled bundle. Due to the small lattice pitch of the bundle, the coolant also acts as a moderator and thus voiding the coolant leads to a lack of moderation and subsequently a lower number of thermal neutrons. Therefore, the air-cooled bundle will have less fission in the thermal region than the air cooled bundle. Inversely, due to the lack of moderation there will be a higher number of fast neutrons, and ^{239}Pu (Fission) is more sensitive in the fast region of the air-cooled bundle than the water-cooled bundle.

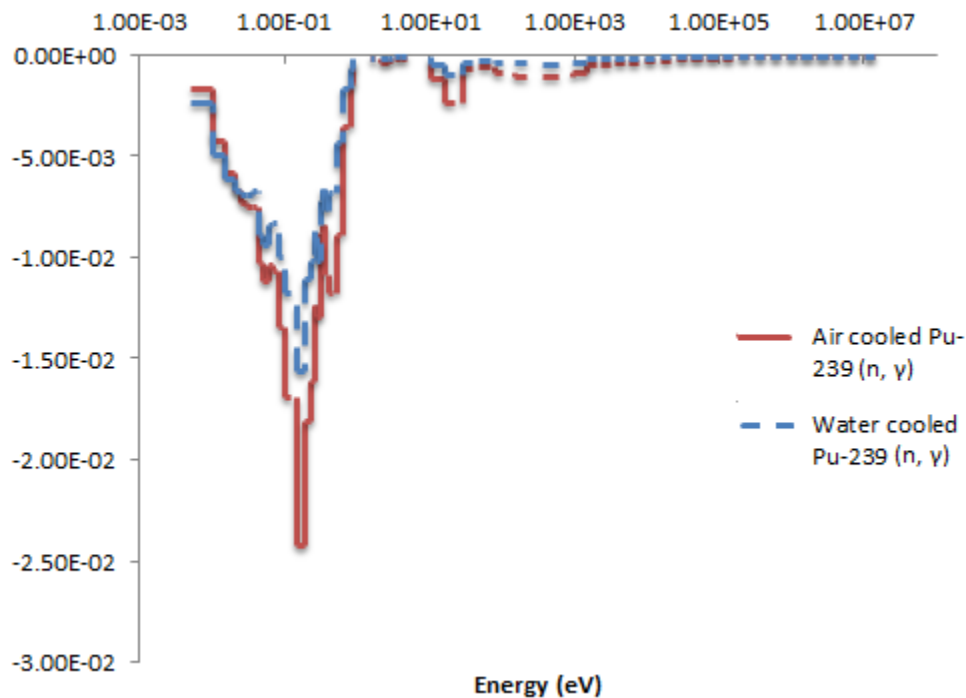


Figure 19: Air cooled vs. water cooled bundle group-wise sensitivity plot of ^{239}Pu (n, γ)
 $(S_{I,A.C.} = -0.195, S_{I,W.C.} = -0.191)$

It is observed that much like $^{232}\text{Th}(n, \gamma)$, $^{239}\text{Pu}(n, \gamma)$ also increases in all energy groups above approximately 0.02 eV when the bundle is voided. Although the adjoint flux is approximately equal between the water-cooled bundle and the voided one, the direct flux differs slightly. In groups with energies below 0.02 eV, the direct flux in the fuel is slightly higher in the water-cooled case and in the higher energy groups the flux is higher in the air-cooled case. Hence, the water-cooled case is observed to be more sensitive to $^{232}\text{Th}(n, \gamma)$ and $^{239}\text{Pu}(n, \gamma)$ in the first 2 groups, and in the subsequent energy groups, it is the air-cooled bundle case which becomes more sensitive to the two reactions.

2.3.6 k_∞ Uncertainty

The infinite (Th,Pu)O₂ bundle lattice uncertainties were calculated using the same method as the ZEEP lattice, explained in the previous section and are presented in table 12.

| Air cooled (Th, Pu)O₂ bundle | | | | |
|--|-------------------|------|----------------|-----------------|
| Nuclide Reaction | σ_k^i (mk) | V% | S _I | σ_k (mk) |
| ²³⁹ Pu ($\bar{\nu}$) | 9.84 | 63.9 | 9.51E-01 | |
| ²³⁹ Pu (Fission) | 5.90 | 23.0 | 5.49E-01 | |
| ²³⁹ Pu (n, γ) | 4.29 | 12.2 | -1.95E-01 | 12.31 |
| ²⁴⁰ Pu (n, γ) | 1.02 | 0.69 | -6.13E-02 | |
| ¹⁶ O (n, α) | 0.23 | 0.03 | -3.51E-03 | |
| Water cooled (Th, Pu)O₂ bundle | | | | |
| ²³⁹ Pu ($\bar{\nu}$) | 9.86 | 64.3 | 9.53E-01 | |
| ²³⁹ Pu (Fission) | 5.91 | 23.1 | 5.49E-01 | |
| ²³⁹ Pu (n, γ) | 4.18 | 11.6 | -1.91E-01 | 12.29 |
| ²⁴⁰ Pu (n, γ) | 1.02 | 0.76 | -6.02E-02 | |
| ¹⁶ O (n, α) | 0.38 | 0.10 | -3.52E-03 | |

Table 12: Water cooled and air cooled (Th,Pu)O₂ bundle lattice isotopic and total uncertainties

With the exception of the ¹⁶O (n, α) reaction, the uncertainties in the (Th,Pu)O₂ infinite lattice follow the same order as its integrated sensitivities. Similar to the ZEEP case ¹⁶O (n, α) is concluded to have a relatively high uncertainty in its nuclear data since its integrated sensitivity is approximately an order of magnitude less than the 5 most sensitive reactions in the lattice, while its contribution to uncertainty in k_∞ is amongst the top 5.

2.3.7 Reaction Rates

The largely negative CVR can be justified by noting the most sensitive isotopes and their various reaction rate perturbations upon voiding the bundle. Table 9 illustrates the fact that the capture and fission reactions in the fuel have a strong impact on the lattice

criticality, thus by comparing the capture and fission rates in both the bundle cases the CVR could be better understood.

Using the flux values generated by DRAGON along with the macroscopic cross-sections of the isotopes, the reaction rates per unit lethargy were initially integrated through volumes of interest and normalized to the total integrated flux in the bundle.

$$RX Rate_g = \sum_{i=1}^m \frac{\phi_{i,g} \Sigma_{RX,i,g} V_i}{\ln\left(\frac{E_g}{E_{g-1}}\right)} \frac{1}{\Phi} \quad (2.65)$$

where RX= Specific reaction (i.e.: fission, capture,...)

g= Energy group number

i = Region number

m= Maximum number regions

Φ = Total integrated flux in the bundle

As observed in figure 20, the voided bundle has lower ²³⁹Pu fission rates in the thermal energy regions, while having higher rates in the fast regions. Due to the lack of moderation a flux shift towards the fast spectrum is expected in the voided case and thus fast fission is observed to have increased in the bundle. However, as shown in the sensitivity per unit lethargy of ²³⁹Pu (Fission) (figure 18), the bundle is most sensitive to thermal fission and thus even though there is an increase in the fast fission rate upon voiding, the decrease in the thermal fission rate is expected to have the greater impact on bundle reactivity.

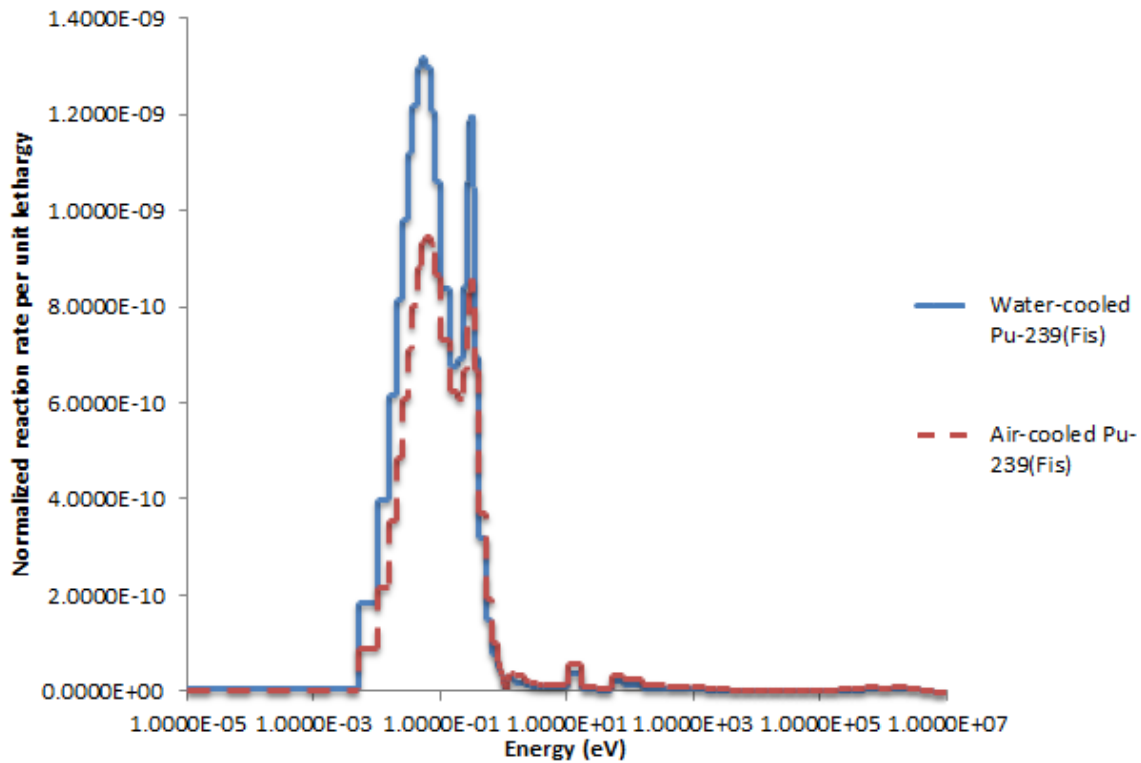


Figure 20: Air cooled vs. water cooled bundle group-wise reaction rates of ^{239}Pu (Fiss) $^{232}\text{Th}(n, \gamma)$ is another reaction which is expected to have a significant impact on the bundle reactivity due to its high concentration and integrated sensitivity. Figure 21 shows that much like the ^{239}Pu (Fission) rate, upon voiding the thermal $^{232}\text{Th}(n, \gamma)$ rate also decreases while the fast $^{232}\text{Th}(n, \gamma)$ rate increases. However, the $^{232}\text{Th}(n, \gamma)$ sensitivity plot shows that the bundle is more sensitive to ^{232}Th capture in the fast region than ^{239}Pu (Fission). Hence, the increase in the fast region of the ^{232}Th absorption rate due to voiding will have a more significant impact on bundle reactivity than the decrease in the fast region of the ^{239}Pu fission.

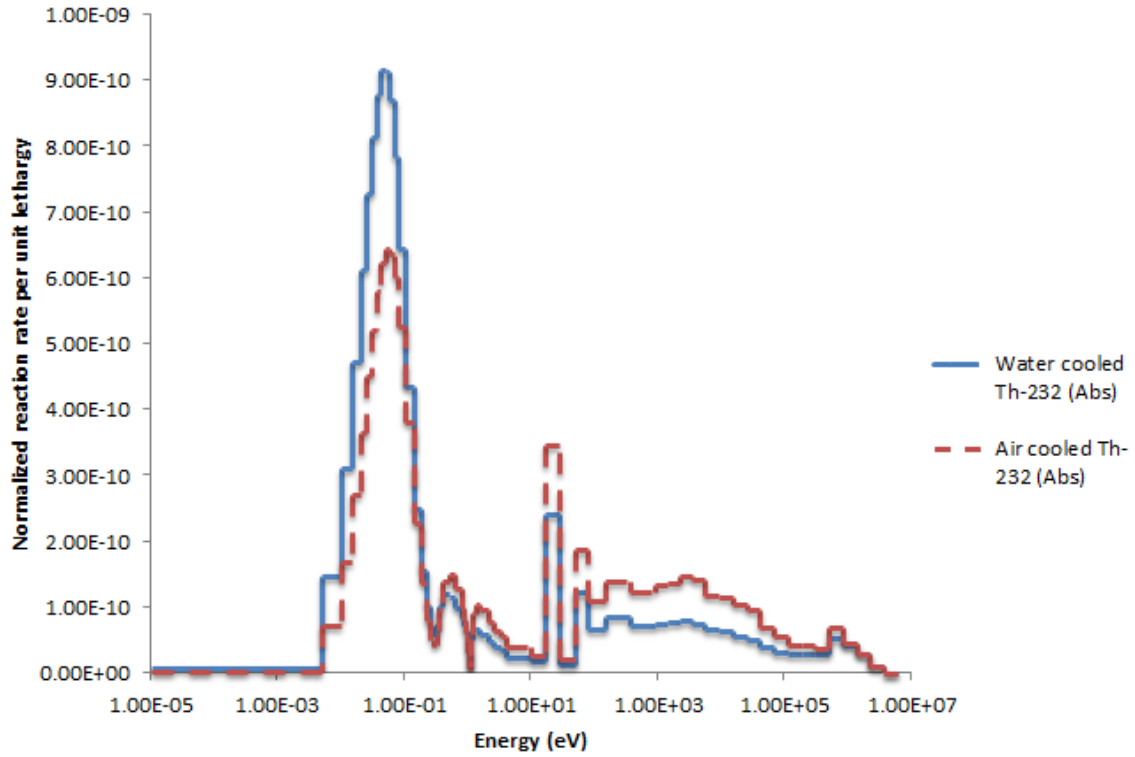


Figure 21: Air cooled vs. water cooled bundle group-wise reaction rates of ^{232}Th (n, γ)

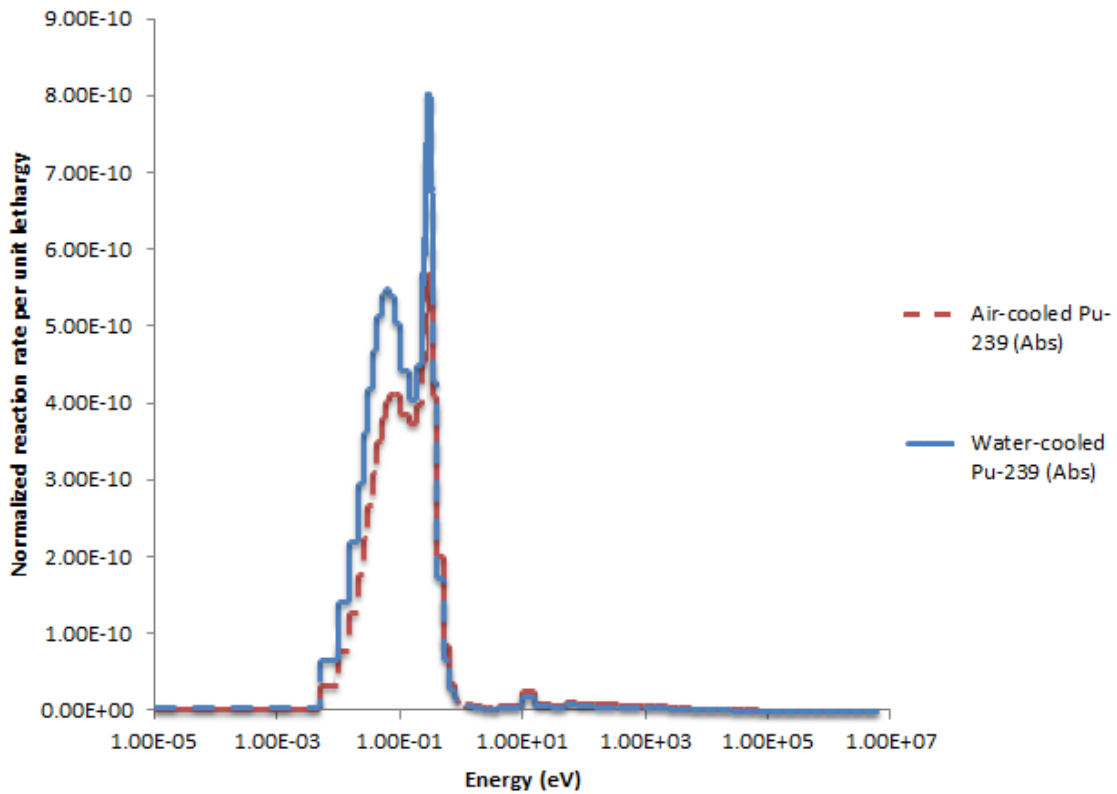


Figure 22: Air cooled vs. water cooled bundle group-wise reaction rates of ^{239}Pu (n, γ)

The trend observed thus far is seen in the ^{239}Pu (n, γ) reaction rate as well, where due to higher levels of moderation in the water-cooled bundle, the thermal region contains a higher ^{239}Pu (n, γ) reaction rate while the fast region has a lower rate. Furthermore, the bundle is observed to be more sensitive to ^{239}Pu (n, γ) in the thermal region and thus, similar to the previous two reactions. The rate decrease in the thermal region upon voiding is expected to be more significant than its increase in the fast region, due to the higher sensitivity observed in the thermal region.

To evaluate the total rates, the group-wise rates were integrated through the energy regions of interest. The following equation was used to calculate total reaction rates:

$$\text{Total RX rate} = \sum_{g=1}^n \sum_{i=1}^m \frac{\Sigma_{RX,i,g} \phi_{i,g} V_i}{\Phi} \quad (2.66)$$

| Reaction | Total Rate(s ⁻¹) cooled | Total rate(s ⁻¹) void | Relative diff. | Thermal rate(s ⁻¹) cooled | Thermal rate(s ⁻¹) void | Relative diff. |
|------------------------------------|--|--------------------------------------|-------------------|---|---|-------------------|
| $^{239}\text{Pu}(\text{Fis})$ | 2.06E-05 | 2.16E-05 | 4.79E-02 | 7.47E-11 | 6.61E-11 | -1.15E-01 |
| $^{239}\text{Pu}(\text{n},\gamma)$ | 3.75E-07 | 4.70E-07 | 2.53E-01 | 3.99E-11 | 3.52E-11 | -1.17E-01 |
| $^{232}\text{Th}(\text{Fis})$ | 1.02E-04 | 1.01E-04 | -8.12E-03 | 0.00E+00 | 0.00E+00 | 0.00E+00 |
| $^{232}\text{Th}(\text{n},\gamma)$ | 4.99E-05 | 5.80E-05 | 1.62E-01 | 3.41E-11 | 3.10E-11 | -9.05E-02 |
| $^{238}\text{Pu}(\text{Fis})$ | 4.08E-08 | 4.23E-08 | 3.63E-02 | 1.17E-15 | 9.45E-16 | -1.91E-01 |
| $^{238}\text{Pu}(\text{n},\gamma)$ | 1.23E-09 | 1.47E-09 | 1.92E-01 | 3.48E-14 | 2.81E-14 | -1.94E-01 |
| $^{240}\text{Pu}(\text{Fis})$ | 4.41E-06 | 4.52E-06 | 2.30E-02 | 2.68E-15 | 3.02E-15 | 1.24E-01 |
| $^{240}\text{Pu}(\text{n},\gamma)$ | 1.42E-07 | 1.76E-07 | 2.34E-01 | 1.12E-11 | 1.24E-11 | 1.02E-01 |
| $^{241}\text{Pu}(\text{Fis})$ | 6.94E-07 | 7.36E-07 | 5.94E-02 | 2.61E-12 | 2.16E-12 | -1.71E-01 |
| $^{241}\text{Pu}(\text{n},\gamma)$ | 3.28E-08 | 3.89E-08 | 1.84E-01 | 9.55E-13 | 7.99E-13 | -1.63E-01 |
| $^{242}\text{Pu}(\text{Fis})$ | 9.87E-08 | 1.01E-07 | 2.27E-02 | 1.24E-18 | 1.18E-18 | -4.72E-02 |
| $^{242}\text{Pu}(\text{n},\gamma)$ | 4.45E-09 | 5.23E-09 | 1.76E-01 | 9.83E-15 | 9.52E-15 | -3.15E-02 |
| Fuel fission | 1.28E-04 | 1.28E-04 | 2.39E-03 | 7.73E-11 | 6.83E-11 | -1.17E-01 |
| Fuel absorption | 5.05E-05 | 5.88E-05 | 1.63E-01 | 8.61E-11 | 7.94E-11 | -7.86E-02 |

Table 13: Integrated (Th,Pu)O₂ bundle fuel reaction rates; Relative diff= (RX_{void}-RX_{cooled})/ RX_{cooled}

As observed from table 11, the total fission rate of the fuel increases by approximately 0.2% upon voiding the bundle. However, this increase is found to be caused by the increased amount of fast fission, since the total thermal fission rate decreases by 11.7% upon voiding. It is important to note that according to the sensitivity analysis, perturbations in the thermal region of the bundle lead to the greatest impact on the bundle reactivity. Hence, the 11.7% decrease in the thermal fission rate is expected to have a more significant impact on the bundle reactivity than the approximately 0.2% increase in the fast fission rate (fast fission dominates total fission rate).

Furthermore, the thermal absorption rate in the fuel is observed to decrease by 7.9% upon voiding. However, due to the thermal fission rate decreasing by a larger value than the thermal absorption rate, a total decrease in the reactivity is expected upon voiding.

Moreover, the fast absorption rate in the fuel is observed to increase by approximately 16%, a much larger increase than the 0.2% fast fission rate increase upon voiding.

Overall, it is observed that due to the relatively small lattice pitch the coolant also acts as a strong moderator. The loss of coolant subsequently leads to a decrease in the thermal neutron population of the bundle which follows a decrease in the thermal fission and absorption rates. However, by calculating the integrated reaction rates in the fuel it was observed that the thermal fission rate decreases more than the thermal absorption rate. Moreover, the increase in the total absorption rate (thermal and fast) was determined to be 2 orders of magnitude higher than the increase in the total fission rate. It is thus determined that the moderating effects of the coolants were much more dominant than its ^1H absorption and hence the CVR is justifiably negative.

2.4 2D Reactor Core

DRAGON was further used to model the full ZED-2 core in 2 dimensions and 69 energy groups. The four experiments done in the ZED-2 were then simulated, and the k_{eff} , direct/adjoint flux and sensitivity/uncertainties in the core were analyzed. The S/U results were then compared with the results of the SCALE 6 package. Subsequently, two libraries were generated for each case for further use in DONJON:

1. The moderator in the outer regions of the core
2. The graphite reflector surrounding the core

The differences between an infinite ZEEP lattice, infinite (Th, Pu)O₂ bundle lattice and the full core were examined and the Coolant Void Reactivity (CVR) of the full core in 2 dimensions was calculated.

Similar to the ZEEP and bundle models, the full core was studied using two geometries, annular geometry (circular model) and Cartesian geometry (square model).

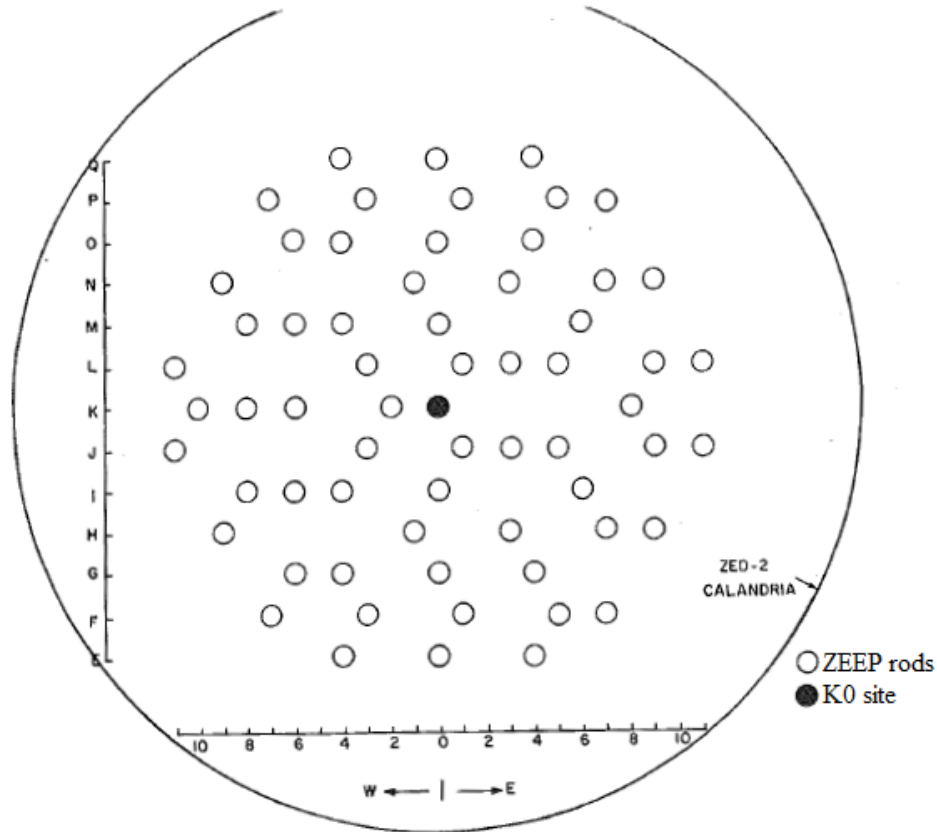


Figure 23: Plan view of the ZED-2 core

2.4.1 Self Shielding Models

The problem with self-shielding calculations for the full core in 2 dimensions is immediately presented as the boundary conditions of the full core (void conditions) contradict those necessary for self-shielding calculations (reflective conditions).

There are two different methods of solving this problem. One can calculate self-shielded cross sections based on the full core geometry using reflective boundary conditions, and

subsequently apply those cross sections to the full core geometry again using void boundary conditions. This method will be the most accurate, yet the most computationally expensive. This is due to the fact that tracking of the geometry will be performed twice: once for the full core with reflective conditions for self-shielding calculations, and once for the full core with voided conditions for flux, k_{eff} and homogenization calculations.

Another method is defining small 2x2 sub-geometries to simulate the various configurations of the ZEEP rods and the (Th,Pu)O₂ bundle within the core, where each 2x2 configuration is modeled using reflective boundary conditions. The cross section library is thus corrected for self-shielding upon the calculations performed for each of the 2x2 sub-geometries and ultimately used for the final full core calculations.

2.4.1.1 The Sub-Geometry Self-Shielding Model

The ZED-2 core contains 6 distinct 2x2 sub-geometries where there is a bundle present in the center of the core, and 4 distinct 2x2 sub-geometries where there is either a ZEEP rod or no fuel in the center of the core. Tracking and subsequently self-shielding calculations were done for all the distinct cases shown in figure 24 and the library was updated upon the completion of each configuration.

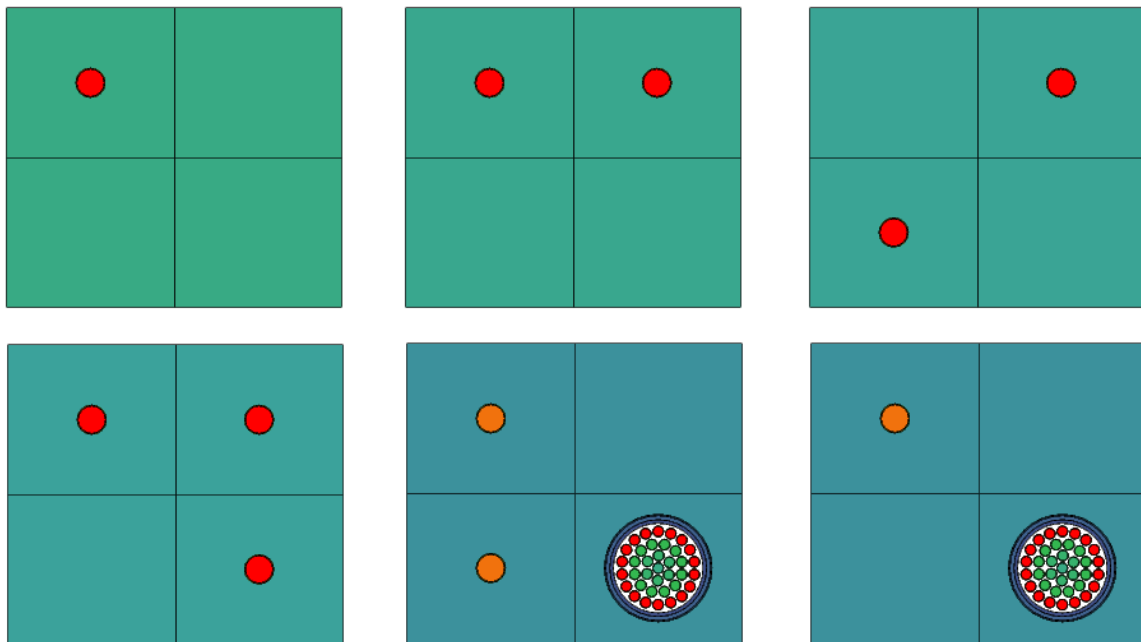


Figure 24: The 6 2x2 sub-geometries present in the ZED-2 core

The sub-geometries modeled portray an approximate image of all the possible 2x2 configurations in the core. However, it should be noted that these sub-geometries are not exact and due to the triangular pitch of the core, Cartesian modeling of these configurations leads to inaccuracy in the results. Furthermore, more error is introduced into the calculations as the sub-geometry method only concerns itself with the immediate surroundings of the ZEEP rods and bundle, yet effects from rods farther away also impact the self-shielding calculations and thus the final k_{eff} of the full core. Yet, alongside with all the sources of error in this method of calculating self-shielding, the great advantage of this method is cutting the calculation time almost in half; hence the results were gathered and compared to the most accurate self-shielding calculations using the global geometry models.

The full core geometry used was the annular geometry, which allowed the exact placement of the ZEEP rods. The following table contains the k_{eff} values for each specific case using the sub-geometry self-shielding method.

| K0 site | k_{eff} |
|---------------------|------------------|
| Water-cooled bundle | 1.048437 |
| Air-cooled bundle | 1.054189 |
| ZEEP rod | 1.054945 |
| No fuel | 1.050344 |

Table 14: The full core k_{eff} calculated for the four cases using the sub-geometry self-shielding method

2.4.1.2 The Global Self-Shielding Model

In this model the full core geometry is initially defined as having reflective boundary conditions. The reflective geometry is further tracked, the self-shielding calculations are completed and the cross section library is corrected. Subsequently, the same geometry is defined again; however the boundary conditions are changed to VOID (representing the vacuum outside the core and thus allowing leakage). This geometry is also tracked and using the previously updated library, the flux, k_{eff} and homogenized cross sections for the

graphite and moderator are determined. Table 15 presents the k_{eff} values calculated using the same geometry as the sub-geometry self-shielding model.

Upon comparing table 14 and table 15 it is observed that the global self-shielding model can differ from the quicker, less accurate sub-geometry model by approximately ± 3 mk. In cases where computation time is an imperative factor, the sub-geometry modeling of the self-shielding is advised, however the global self-shielding model is proved to have a notable difference in the criticality.

| K0 site | k_{eff} |
|---------------------|------------------|
| Water-cooled bundle | 1.047586 |
| Air-cooled bundle | 1.056441 |
| ZEEP rod | 1.051454 |
| No fuel | 1.049985 |

Table 15: The full core k_{eff} calculated for the four cases using the global-geometry self-shielding method

Furthermore, in cases with a less complex geometry, where Cartesian sub-geometries have a more accurate representation of the local geometries in the core, and in cases where larger local geometries, such as 3x3 or even 4x4 Cartesian cells can be defined, the sub-geometry self-shielding model will have a large improvement in its accuracy and will still be the less computationally demanding option.

2.4.2 k_{eff} Analysis

As observed from table 15, the cases containing water-cooled (Th,Pu)O₂ bundles have the lowest k_{eff} values. This is due to the fact that in the thermal region, ²³²Th is a strong and non-fissile neutron absorber, and thus both the light-water and air cooled bundles are observed to have a dip in the flux in the center of the core. Figure 25 illustrates the difference between the lower energy integrated flux in the center of the light-water cooled bundle case compared to the ZEEP rod case.

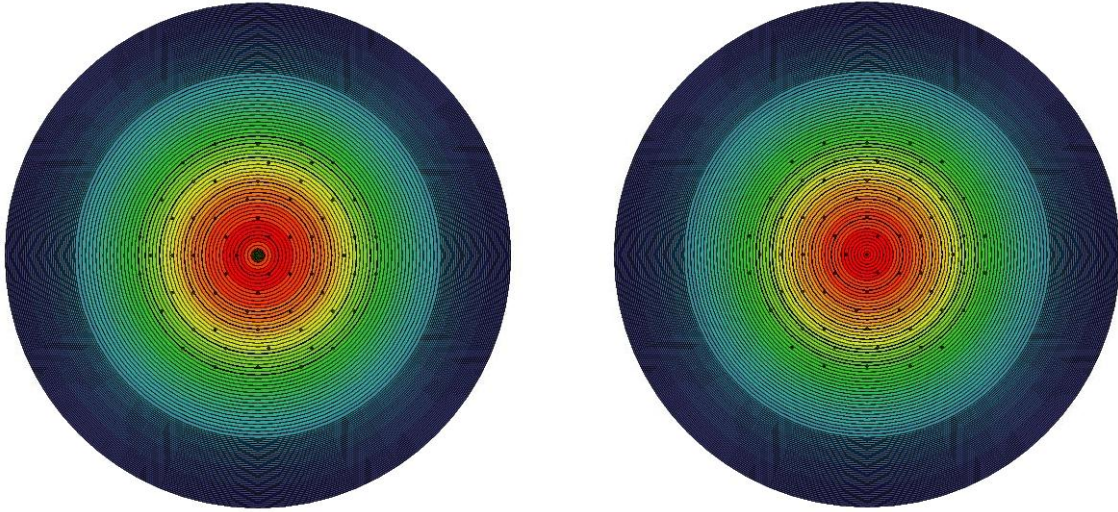


Figure 25: Energy integrated flux of water-cooled (Th,Pu)O₂ bundle case (left) and the ZEEP rod case (right)

Figure 26 represents the flux spectrum in the center of the core of the four individual cases. As observed the case where the center of the core contains no fuel has the highest concentration of thermal neutrons and the lowest concentration of fast neutrons. This is due to the fact that there are no fissile isotopes to absorb thermal neutrons and subsequently produce fast ones. Furthermore the ZEEP rod case is observed to have a slightly lower concentration of thermal neutrons, and a slightly higher concentration of fast ones due to the presence of fissile isotopes in the ZEEP fuel.

The major difference is observed when the bundle is inserted in the center of the core.

The thermal concentration of neutrons decreases by approximately half while the concentration of fast neutrons increases. Thermal neutron absorption is much higher in the bundle than in the ZEEP rod; this is due to the presence of ²³²Th which acts as a strong and non-fissile neutron absorber in the thermal region of the spectrum.

Furthermore, the presence of ²³⁸Pu, ²³⁹Pu, ²⁴⁰Pu, ²⁴¹Pu, and ²⁴²Pu isotopes adds to the absorption and fission rates in the bundle. The plutonium isotopes are observed to have a higher average neutron yield than ²³⁵U and thus the concentration of fast neutrons in the bundle case are observed to be higher.

It is imperative to note that the neutron spectrum of the case where the center bundle is voided does not differ significantly from the case where the center bundle is cooled with light water. The similarity illustrates that the coolant did not have a significant moderating role in the bundle within the full core. This contrasts the earlier observation

of the neutron spectrum of an infinite (Th,Pu)O₂ lattice, where voiding the light water coolant led to a significant decline in the concentration of thermal neutrons, and an increase in the concentration of fast neutrons (figure 13) and thus proving that the coolant was acting as a strong moderator in the infinite lattice. Therefore, while the coolant's moderating power played the dominant role in the infinite (Th,Pu)O₂ bundle lattice leading to a CVR of -31.17 mk, its role was minimized in one bundle placed in the center of the core.

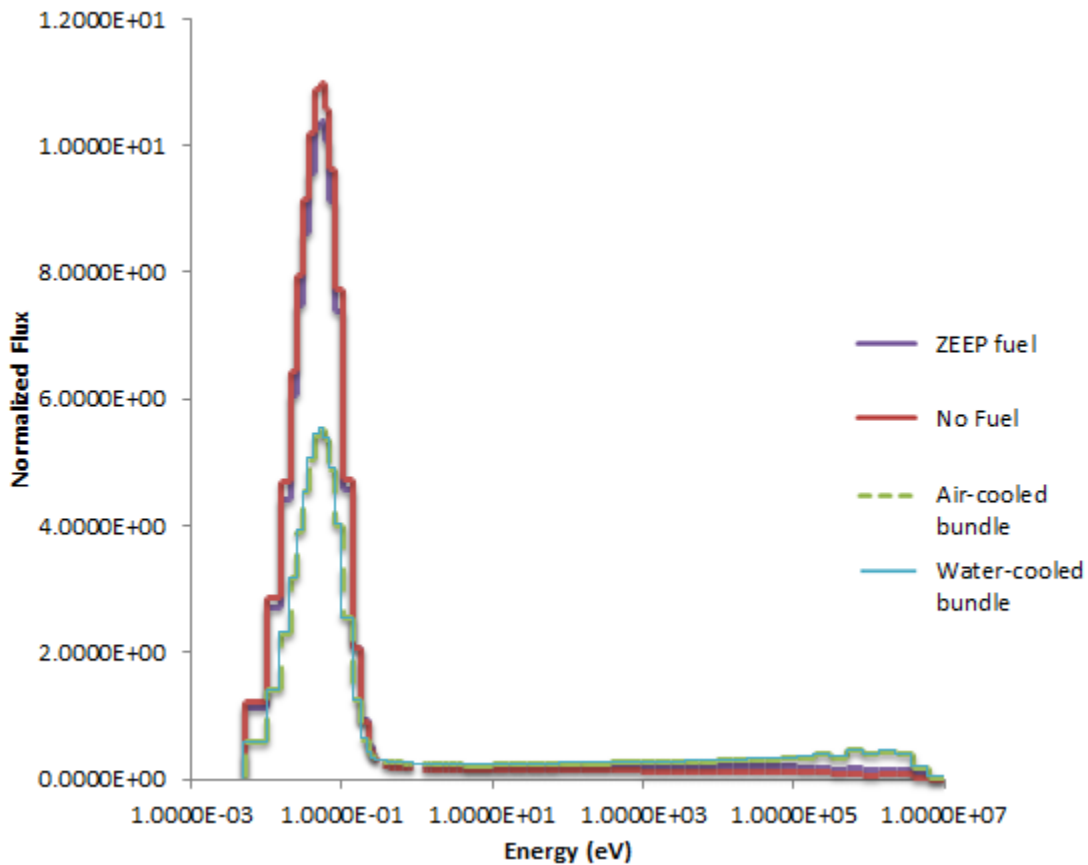


Figure 26: The flux spectra of the center of the core (the K0 site) of the four full core cases

2.4.3 Full Core Sensitivity

2.4.3.1 K0 Site – Air Cooled and Water Cooled Bundle

Using the same aforementioned methodology, the adjoint and direct fluxes were calculated using DRAGON and subsequently fed to SUS3D for sensitivity calculations. The integrated sensitivities of the case with the air-cooled (Th,Pu)O₂ bundle in the K0

site of the core and the case with the water-cooled (Th,Pu)O₂ bundle in the K0 site of the core are listed in table 16.

The sensitivities of the two cases are observed to be similar. The fissile isotopes in both cases show the same integrated sensitivity to $\bar{\nu}$. It is thus determined that the values of $\bar{\nu}$ have not been altered significantly in any of the fissile isotopes in the core upon voiding the central bundle. The ²³⁵U ($\bar{\nu}$) value has the highest integrated sensitivity coefficient amongst the listed reactions. This is due to the abundance of ZEEP rods, containing natural uranium fuel, in the core. As observed from figure 27, the group-wise sensitivity plots of ²³⁵U($\bar{\nu}$) in both cases, air cooled bundle and water cooled bundle in the K0 site, are almost identical. This was expected as both cases shared the same ²³⁵U($\bar{\nu}$) integrated sensitivity coefficient.

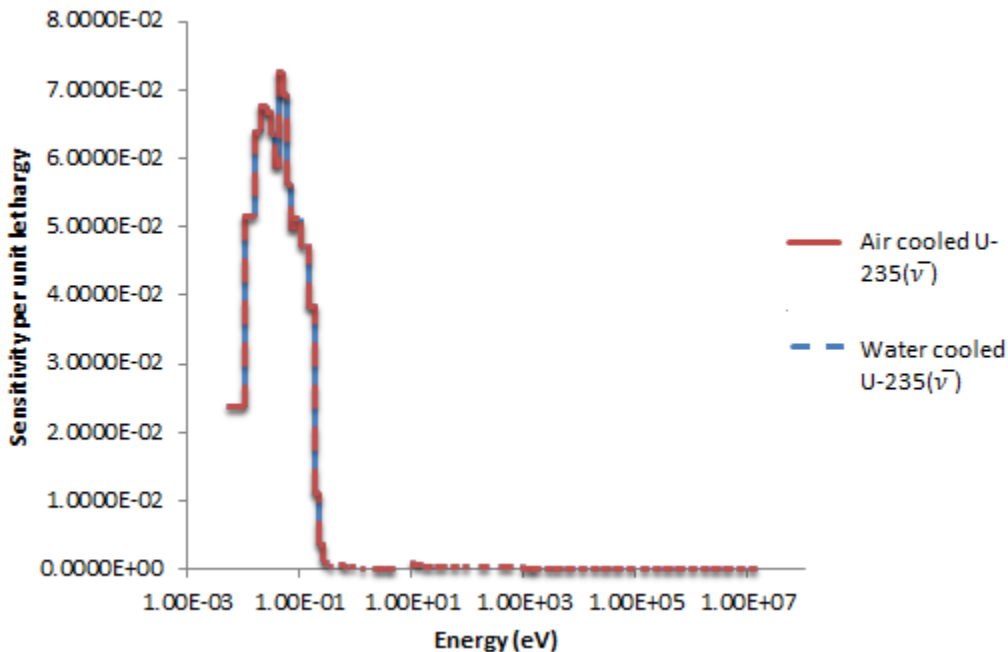


Figure 27: ²³⁵U ($\bar{\nu}$) group wise sensitivity profiles of K0 site with air cooled (Th,Pu)O₂ bundle ($S_I=0.808$) and K0 site with water cooled (Th,Pu)O₂ bundle ($S_I=0.808$)

The ²³⁵U fission integrated sensitivity coefficient is observed to have a larger value in the water cooled case. However, it is important to note that the fission reaction is not directly correlated to the sensitivity coefficient since the fission term appears in both the gain term and the loss term of the sensitivity coefficient formula. Thus a larger ²³⁵U sensitivity coefficient does not necessitate an overall increase of ²³⁵U fission in the core. The

leakage in the core increases upon voiding the central bundle and further leads to a decrease in the fission sensitivity coefficient in the voided case. The group-wise sensitivity plot (figure 28) shows a decrease in sensitivity in the thermal regions (below 0.2 eV) upon voiding the central bundle.

Contrary to ^{235}U fission, ^{238}U (n,γ) has a consistently higher sensitivity in all energy regions of the spectrum in the air cooled case. Consequently, the integrated sensitivity of ^{238}U (n,γ) is higher in the air cooled bundle case than the water cooled case.

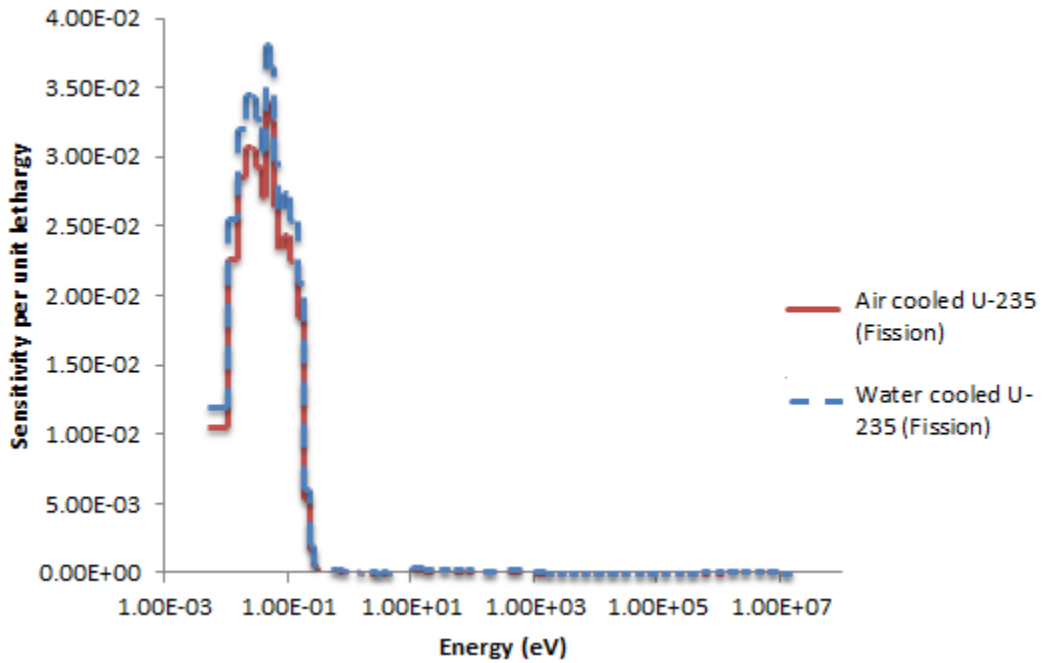


Figure 28: ^{235}U (Fiss) group wise sensitivity profiles of K0 site with air cooled $(\text{Th,Pu})\text{O}_2$ bundle ($S_I=0.403$) and K0 site with water cooled $(\text{Th,Pu})\text{O}_2$ bundle ($S_I=0.421$)

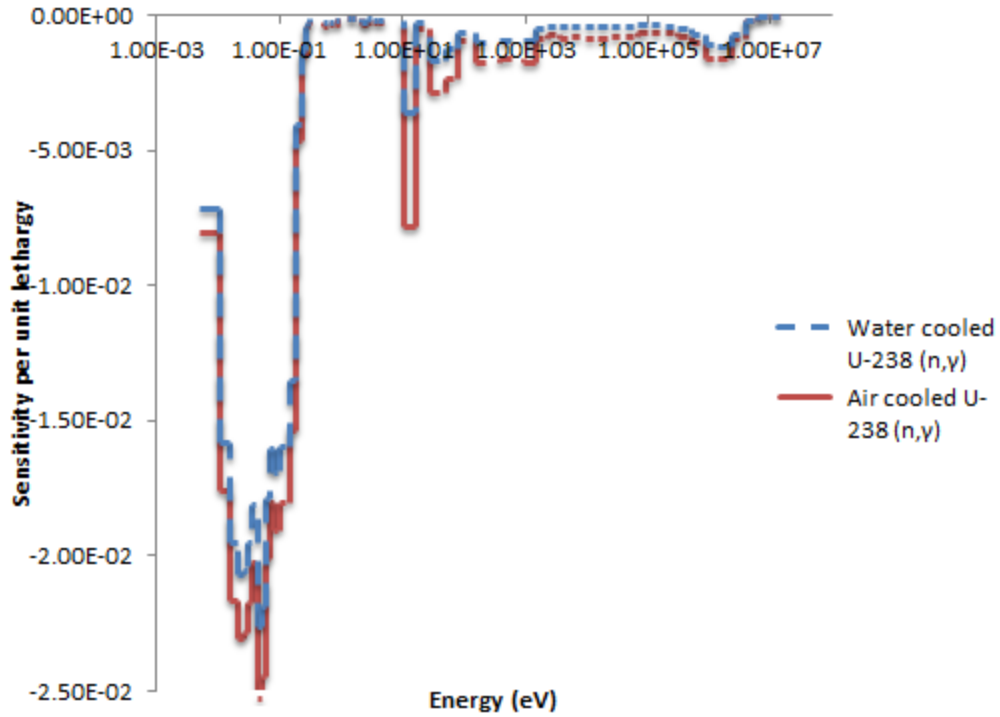


Figure 29: ^{238}U (n, γ) group wise sensitivity profiles of K0 site with air cooled (Th,Pu) O_2 bundle ($S_I=-0.319$) and K0 site with water cooled (Th,Pu) O_2 bundle ($S_I=-0.273$)

^{239}Pu fission plays an equally important role in both cases, as observed by their equal integrated sensitivities. As expected, the group-wise sensitivities of the two cases overlap extensively throughout the energy regions, where the highest sensitivities are observed in the thermal region due to the isotope's high fission cross section in this energy range.

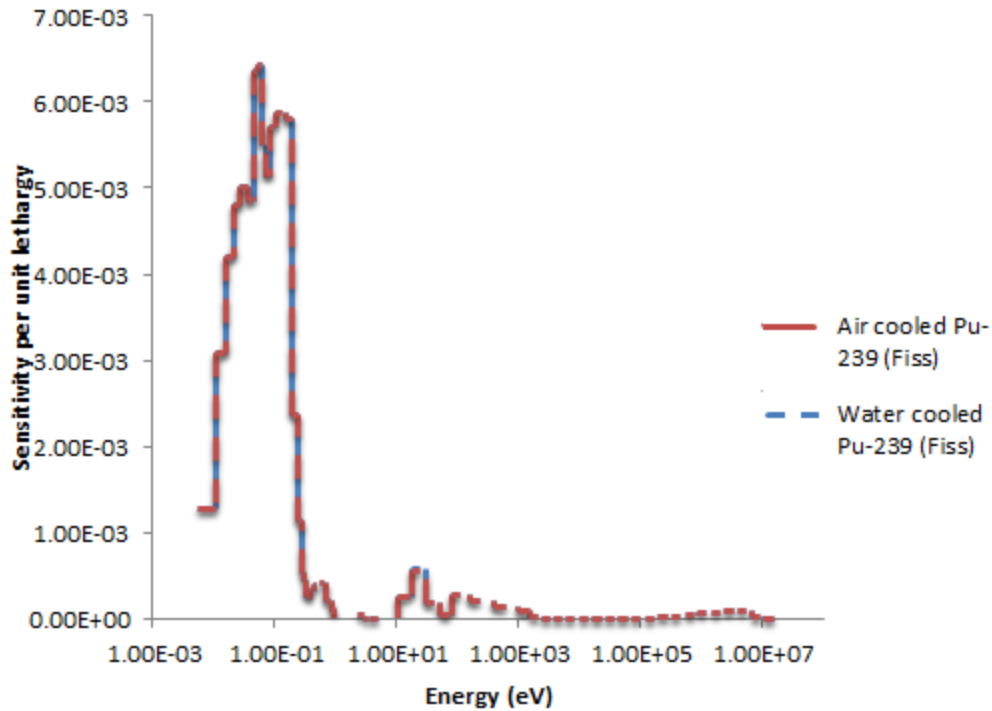


Figure 30: ^{239}Pu (fiss) group wise sensitivity profiles of K0 site with air cooled $(\text{Th,Pu})\text{O}_2$ bundle ($S_I=5.70 \times 10^{-2}$) and K0 site with water cooled $(\text{Th,Pu})\text{O}_2$ bundle ($S_I=5.70 \times 10^{-2}$)

The group-wise sensitivity plot of ^{232}Th (n,γ) (figure 31) portrays a decrease in the epithermal regions of the energy spectrum upon voiding the central bundle. This is due to the lowering of the cross sections in the resonance energy regions, $9.88 \text{ eV} - 9.12 \times 10^3 \text{ eV}$ (figure 32). Moreover, the integrated sensitivity of ^{232}Th (n,γ) is observed to be lower in the voided case.

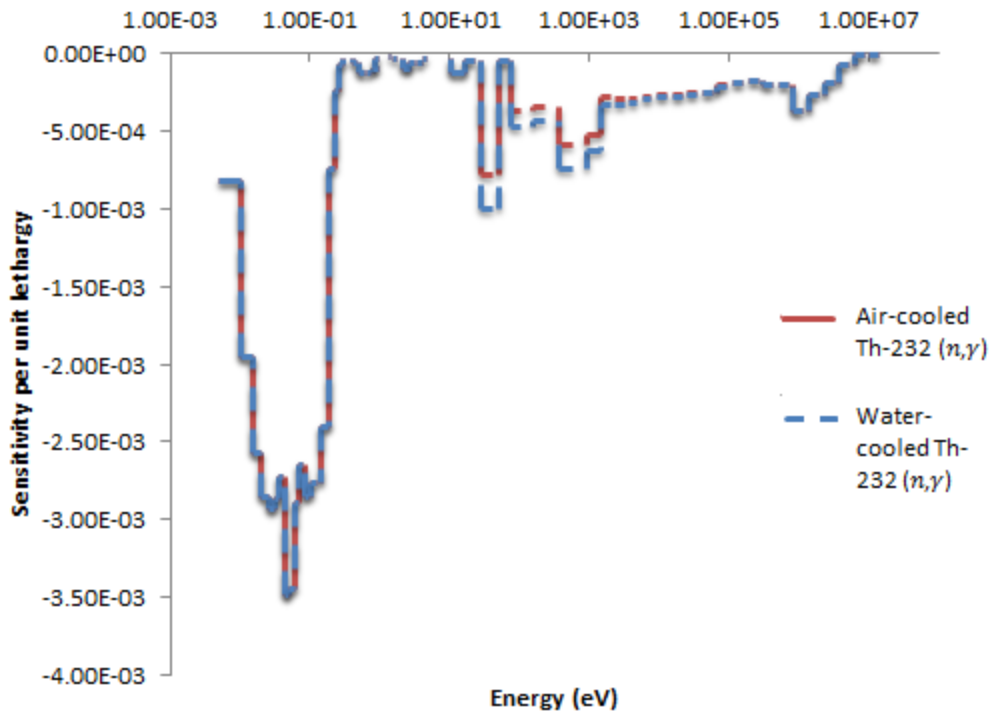


Figure 31: ^{232}Th (n,γ) group wise sensitivity profiles of K0 site with air cooled (Th,Pu) O_2 bundle and K0 site with water cooled (Th,Pu) O_2 bundle

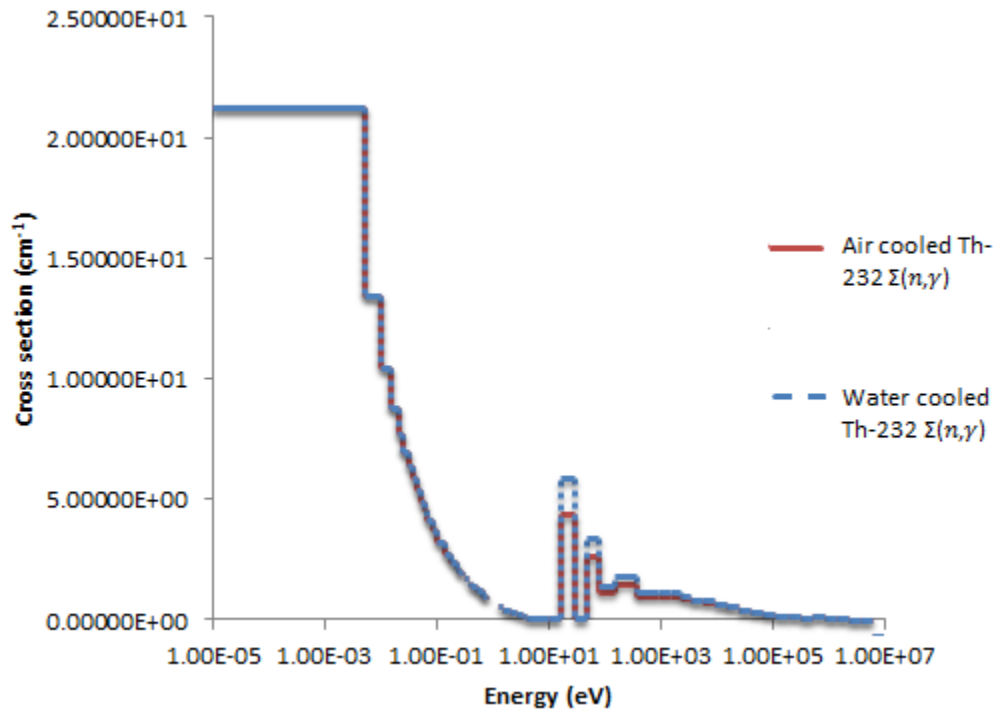


Figure 32: Self-shielding corrected ^{232}Th (n,γ) water-cooled and voided cross sections

Another important reaction to note is the ^1H scattering reaction. The reaction's integrated sensitivity coefficient shows an increase upon voiding the bundle. However, this does not prove an overall increase in the importance of ^1H scattering in the full core with a voided bundle, which only contains ^1H isotopes in the impurities of its moderator. The group-wise water-cooled ^1H sensitivity coefficients (figure 33) show large positive and negative peaks in the resonance regions of the energy spectrum, corresponding to fission and absorption resonances belonging to the fuel nuclides in the bundle. Furthermore, it is observed that in energy regions above 1×10^5 eV, the water-cooled ^1H elastic sensitivities are a negative value which is in contrast to the slightly positive air-cooled bundle sensitivities. This is due to the fact that these energy regions possess higher fission than absorption cross sections. Moreover, the light water coolant also acts a moderator which leads to a decrease in fast flux and hence fast fission, therefore the elastic sensitivity of ^1H (present chiefly in the coolant) leads to a decrease in reactivity in energy regions above 1×10^5 eV.

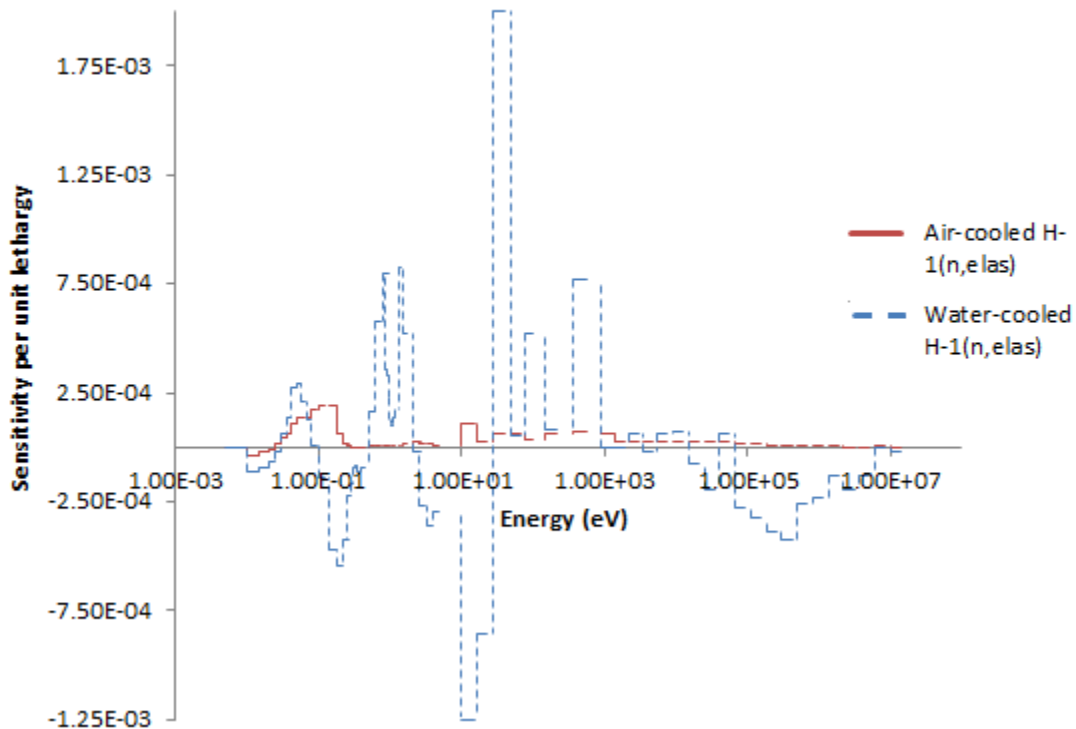


Figure 33: ^1H (n, elas) group wise sensitivity plots of K0 site with air cooled $(\text{Th,Pu})\text{O}_2$ bundle ($S_I=2.07 \times 10^{-3}$) and K0 site with water cooled $(\text{Th,Pu})\text{O}_2$ bundle ($S_I=1.15 \times 10^{-3}$)

| Air-cooled Bundle Case | | | | Water-cooled Bundle Case | | | |
|-------------------------|----------------|---------------------------|----------------|--------------------------|----------------|---------------------------|----------------|
| Reaction | S _I | Reaction | S _I | Reaction | S _I | Reaction | S _I |
| ²³⁵ U (ν̄) | 8.08E-01 | ²³⁸ U (Fis) | 2.30E-02 | ²³⁵ U (ν̄) | 8.08E-01 | ²³⁹ Pu (n,γ) | -2.63E-02 |
| ²³⁵ U (Fis) | 4.03E-01 | ¹⁶ O (n, elas) | 1.15E-02 | ²³⁵ U (Fis) | 4.21E-01 | ¹⁶ O (n, elas) | 1.12E-02 |
| ²³⁸ U (n,γ) | -3.19E-01 | ²⁴¹ Pu (ν̄) | 7.07E-03 | ²³⁸ U (n,γ) | -2.73E-01 | ²⁴¹ Pu (ν̄) | 7.07E-03 |
| ²³⁹ Pu (ν̄) | 1.10E-01 | ²⁴⁰ Pu (n,γ) | -6.37E-03 | ²³⁹ Pu (ν̄) | 1.10E-01 | ²⁴⁰ Pu (n,γ) | -6.39E-03 |
| ²³⁹ Pu (Fis) | 5.70E-02 | ¹⁶ O (n,γ) | -4.36E-03 | ²³⁹ Pu (Fis) | 5.70E-02 | ¹⁶ O (n,γ) | -4.36E-03 |
| ²³⁵ U (n,γ) | -7.50E-02 | ²⁴¹ Pu (Fis) | 4.05E-03 | ²³⁵ U (n,γ) | -6.63E-02 | ²⁴¹ Pu (Fis) | 4.05E-03 |
| ²³⁸ U (ν̄) | 4.51E-02 | ¹⁶ O (n,α) | -3.40E-03 | ¹ H (n,γ) | -4.77E-02 | ¹⁶ O (n,α) | -3.49E-03 |
| ¹ H (n,γ) | -4.22E-02 | ¹ H (n, elas) | 2.07E-03 | ²³⁸ U (ν̄) | 4.51E-02 | ¹ H (n, elas) | 1.15E-03 |
| ²³² Th (n,γ) | -3.31E-02 | ²⁴¹ Pu (n,γ) | -1.03E-03 | ²³² Th (n,γ) | -3.00E-02 | ²⁴¹ Pu (n,γ) | -1.03E-03 |
| ²³⁹ Pu (n,γ) | -2.62E-02 | | | ²³⁸ U (Fis) | 2.77E-02 | | |

Table 16: Integrated sensitivities of the isotopes in full cores where K0 site with air cooled (Th,Pu)O₂ bundle and K0 site with water cooled (Th,Pu)O₂ bundle

2.4.3.2 K0 Site – ZEEP Rod and No Fuel

Having an identical material composition, the two cases (K0 site containing a ZEEP rod and K0 site containing no fuel) are expected to have almost identical sensitivity coefficients. As observed in table 15, there is a large degree of similarity between the two cases, with the largest difference belonging to the sensitivity coefficient of ²³⁸U (n,γ), with a difference of 0.002 between the ZEEP rod case and the no fuel case. As expected, ²³⁵U (ν̄) is the most sensitive reaction in both cases, followed by ²³⁵U fission and ²³⁸U capture. The group-wise sensitivity plots further illustrate the similarities between these two cases.

| ZEEP rod | | No Fuel | |
|--|-----------|--|-----------|
| Reaction | S_I | Reaction | S_I |
| $^{235}\text{U} (\bar{\nu})$ | 9.47E-01 | $^{235}\text{U} (\bar{\nu})$ | 9.47E-01 |
| $^{235}\text{U} (\text{Fis})$ | 4.95E-01 | $^{235}\text{U} (\text{Fis})$ | 4.96E-01 |
| $^{238}\text{U} (\text{n},\gamma)$ | -3.18E-01 | $^{238}\text{U} (\text{n},\gamma)$ | -3.16E-01 |
| $^{235}\text{U} (\text{n},\gamma)$ | -7.75E-02 | $^{235}\text{U} (\text{n},\gamma)$ | -7.72E-02 |
| $^{238}\text{U} (\bar{\nu})$ | 5.29E-02 | $^{238}\text{U} (\bar{\nu})$ | 5.31E-02 |
| $^1\text{H} (\text{n},\gamma)$ | -4.11E-02 | $^1\text{H} (\text{n},\gamma)$ | -4.21E-02 |
| $^{238}\text{U} (\text{Fis})$ | 3.25E-02 | $^{238}\text{U} (\text{Fis})$ | 3.27E-02 |
| $^{16}\text{O} (\text{n},\text{elas})$ | 1.24E-02 | $^{16}\text{O} (\text{n}, \text{elas})$ | 1.25E-02 |
| $^{16}\text{O} (\text{n},\gamma)$ | -4.24E-03 | $^{16}\text{O} (\text{n},\gamma)$ | -4.35E-03 |
| $^{16}\text{O} (\text{n},\alpha)$ | -2.93E-03 | $^{16}\text{O} (\text{n},\alpha)$ | -2.93E-03 |
| $^1\text{H} (\text{n}, \text{elas})$ | 2.15E-03 | $^1\text{H} (\text{n}, \text{elas})$ | 2.16E-03 |
| $^{238}\text{U} (\text{n}, \text{elas})$ | -3.75E-04 | $^{238}\text{U} (\text{n}, \text{elas})$ | -3.80E-04 |
| $^{235}\text{U} (\text{n}, \text{elas})$ | 4.58E-06 | $^{235}\text{U} (\text{n}, \text{elas})$ | 4.63E-06 |

Table 17: Integrated sensitivities of the isotopes in full cores where K0 site with ZEEP rod bundle and K0 site with no fuel

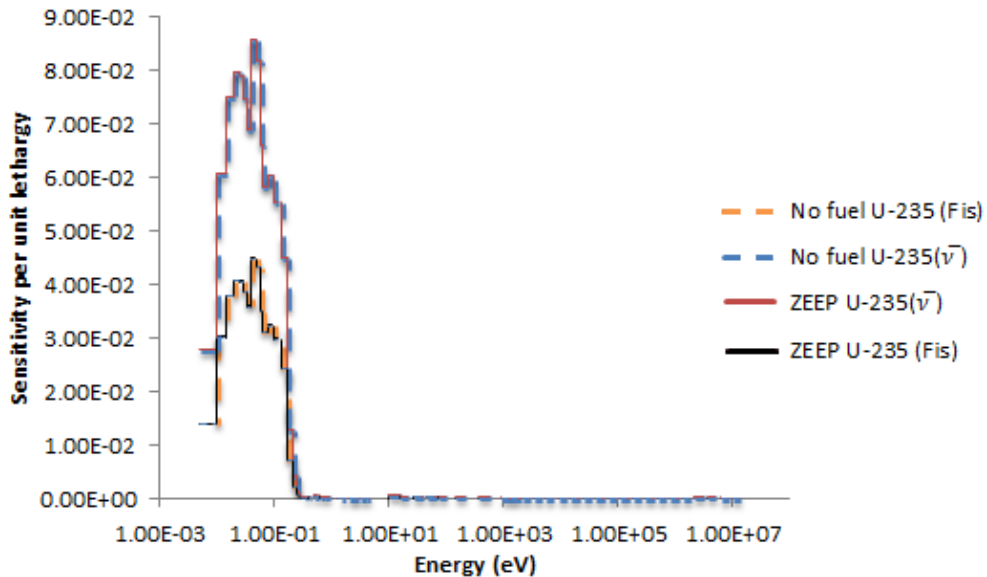


Figure 34: $^{235}\text{U} (\bar{\nu})$ and (fiss) group wise sensitivity plots of K0 site with ZEEP rod and K0 site with no fuel

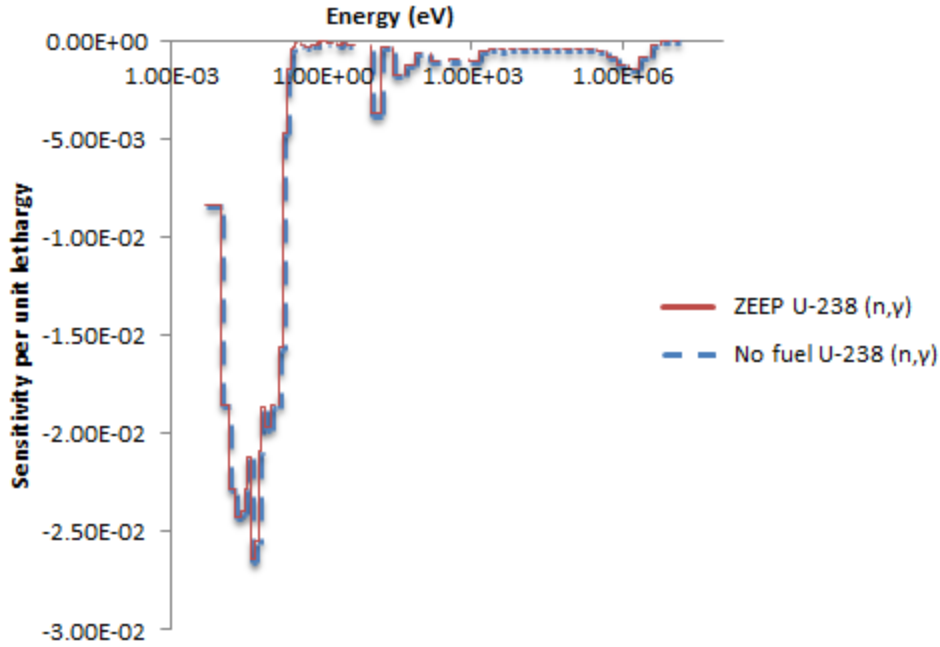


Figure 35: $^{238}\text{U}(n,\gamma)$ group wise sensitivity plots of K0 site with ZEEP rod and K0 site with no fuel

2.4.4 k_{eff} Uncertainty and Code to Code Comparison

Using the sensitivity results from the four full core cases, the uncertainty of various isotopes' nuclear data on the k_{eff} was calculated. The uncertainties were then compared to SCALE6 results, calculated using the SAMS module [31].

As observed from table 16, the integrated sensitivities calculated using the DRAGON/SUSD3D were generally within 5% of the results from SCALE 6. This compatibility proves that the differences in the uncertainties are due to the libraries used, and not the sensitivity calculations, further illustrating the fact that the direct and adjoint flux results by the two codes were similar and the DRAGON/ SUSD3D coupling was effective.

The first two cases containing a ZEEP rod in the K0 site and no fuel in the K0 site show almost identical uncertainties in their nuclear data. The two cases containing the (Th,Pu) O_2 bundle, however, show slight differences in their major uncertainty contributors. The majority of these differences arise from the change in the sensitivity vectors between the two cases. As observed, $^{238}\text{U}(n,\gamma)$ sensitivity increases upon voiding the central bundle, and subsequently, the uncertainty associated with the reaction also

increases. Furthermore, ^{235}U (Fission) is observed to decrease upon voiding, leading to a decrease in its uncertainty contribution to the reactor's k_{eff} .

| K0 Site | Reaction | SUSD3D | | SCALE 6 [31] | |
|--|--------------------------------|-------------------------|-------|-------------------------|-------|
| | | $\sigma_k^i(\text{mk})$ | S_I | $\sigma_k^i(\text{mk})$ | S_I |
| No Fuel SUSD3D σ_k : ± 7.1 mk SCALE6 σ_k : ± 7.5 mk | $^{238}\text{U} (n,\gamma)$ | 6.33 | -0.32 | 5.72 | -0.34 |
| | $^{235}\text{U} (\bar{\nu})$ | 2.93 | 0.95 | 2.86 | 0.93 |
| | $^{235}\text{U} (\text{Fis})$ | 0.97 | 0.49 | 1.65 | 0.48 |
| ZEEP rod SUSD3D σ_k : ± 7.1 mk SCALE6 σ_k : ± 7.5 mk | $^{238}\text{U} (n,\gamma)$ | 6.33 | -0.32 | 5.73 | -0.34 |
| | $^{235}\text{U} (\bar{\nu})$ | 2.93 | 0.95 | 2.86 | 0.93 |
| | $^{235}\text{U} (\text{Fis})$ | 0.97 | 0.49 | 1.65 | 0.47 |
| Water cooled (Th,Pu) O_2 bundle SUSD3D σ_k : ± 6.3 mk SCALE6 σ_k : ± 6.9 mk | $^{238}\text{U} (n,\gamma)$ | 5.45 | -0.27 | 5.17 | -0.30 |
| | $^{235}\text{U} (\bar{\nu})$ | 2.50 | 0.81 | 2.60 | 0.83 |
| | $^{235}\text{U} (\text{Fis})$ | 0.82 | 0.42 | 1.50 | 0.43 |
| | $^{239}\text{Pu} (\bar{\nu})$ | 1.44 | 0.11 | 0.94 | 0.09 |
| | $^{239}\text{Pu} (\text{Fis})$ | 0.49 | 0.06 | 0.49 | 0.05 |
| | $^{232}\text{Th}(n,\gamma)^*$ | 0.44 | -0.03 | 0.30 | -0.03 |
| Air cooled (Th,Pu) O_2 bundle SUSD3D σ_k : ± 6.5 mk SCALE6 σ_k : ± 6.9 mk | $^{238}\text{U} (n,\gamma)$ | 6.28 | -0.32 | 5.14 | -0.30 |
| | $^{235}\text{U} (\bar{\nu})$ | 2.50 | 0.81 | 2.57 | 0.83 |
| | $^{235}\text{U} (\text{Fis})$ | 0.73 | 0.40 | 1.49 | 0.42 |
| | $^{239}\text{Pu} (\bar{\nu})$ | 1.44 | 0.11 | 1.0 | 0.10 |
| | $^{239}\text{Pu}(\text{Fis})$ | 0.49 | 0.06 | 0.53 | 0.05 |
| | $^{232}\text{Th}(n,\gamma)^*$ | 0.46 | -0.03 | 0.34 | -0.03 |
| | $^1\text{H} (n,\gamma)$ | 0.24 | -0.05 | 0.28 | -0.05 |
| | $^1\text{H} (n,\gamma)$ | 0.21 | -0.04 | 0.26 | -0.05 |

Table 18: SUSD3D vs. SCALE6 uncertainty and integrated sensitivity results

* The $^{232}\text{Th} (n, \gamma)$ covariance data were not available in the covariance matrices used in this work. Thus, the group-wise diagonal covariance matrix values of the $^{232}\text{Th} (n, \gamma)$

listed in the reference [32] were used. The values listed in the reference are based on “educated guesses” and only represent the diagonal values of the full covariance, hence neglecting all types of correlation (among reactions, in energy, between different isotopes, etc.). Furthermore, the data is presented for 17 energy groups, thus the first step to calculating the total uncertainty contribution of $^{232}\text{Th}(n, \gamma)$ was to collapse the sensitivity data from 69 groups to 17, equation (2.67).

$$S_{\lambda,k}^{Th^{232}(n,\gamma)} = \sum_{g \in G_k} S_{\lambda,g}^{Th^{232}(n,\gamma)} \ln\left(\frac{E_g}{E_{g-1}}\right) \quad (2.67)$$

where for every index $k \in [1,17]$ there exists a set of indices $g \in [1,69] : G_k$

Since no off diagonal components existed in the covariance matrix, the condensed group-wise sensitivity coefficients were then squared and multiplied by the uncertainty in each energy group (equation 1.64).

The final uncertainty value obtained for the water cooled case was 0.44 mk, while the SCALE6 uncertainty result [3] was 0.303 mk. The reason for this discrepancy must lie in the uncertainty data used, since the integrated sensitivities between the two codes are almost identical.

The air cooled case shared a similar pattern; the uncertainty value calculated for this case was 0.46 mk while the SCALE6 result was 0.340 mk. The integrated sensitivities for the air cooled case were calculated as -0.033 with SUS3D and -0.0315 with SCALE 6.

Thus, the importance of a consistency in covariance libraries is emphasized, and the need for more uncertainty data is observed.

2.4.5 Air Cooled Bundle vs. Water Cooled Bundle Reaction Rates

Using equation (2.65), the group-wise reaction rates were calculated for all the fissile isotopes in the core, alongside with ^1H and ^{16}O . The rates of the most sensitive reactions in the core were then plotted to compare the case containing a water cooled (Th,Pu) O_2 bundle in the K0 site, and the case containing an air cooled bundle in the K0 site.

However, upon analyzing the group-wise relative differences between the case containing a cooled central bundle and the other containing a voided one, it is observed that there is a slight decrease in thermal fission upon voiding. This is due to the increase in fast flux and an increase in leakage in the central bundle, subsequently leading to an increase in

epithermal resonance capture by both ^{235}U and ^{238}U prior to thermalization. This effect is illustrated in the epithermal region of figure 37 where large positive peaks, corresponding to the resonant regions of the ^{235}U fission cross section, are observed. Furthermore, there is a consistent increase in fast fission upon voiding, corresponding to an increased leakage of fast neutrons from the central bundle.

The absorption rate of ^{238}U also plays an important role in the core reactivity. As shown in figure 38, the ^{238}U absorption rate, similar to the ^{235}U fission rate, decreases in the thermal region while increasing in the epithermal and fast regions. Being located outside the central bundle, the ^{238}U isotopes absorb the fast and epithermal neutrons, which leaked from the bundle, and the lower thermal flux caused by the voiding of the central bundle leads to the slight decrease in the thermal capture in ^{238}U upon voiding.

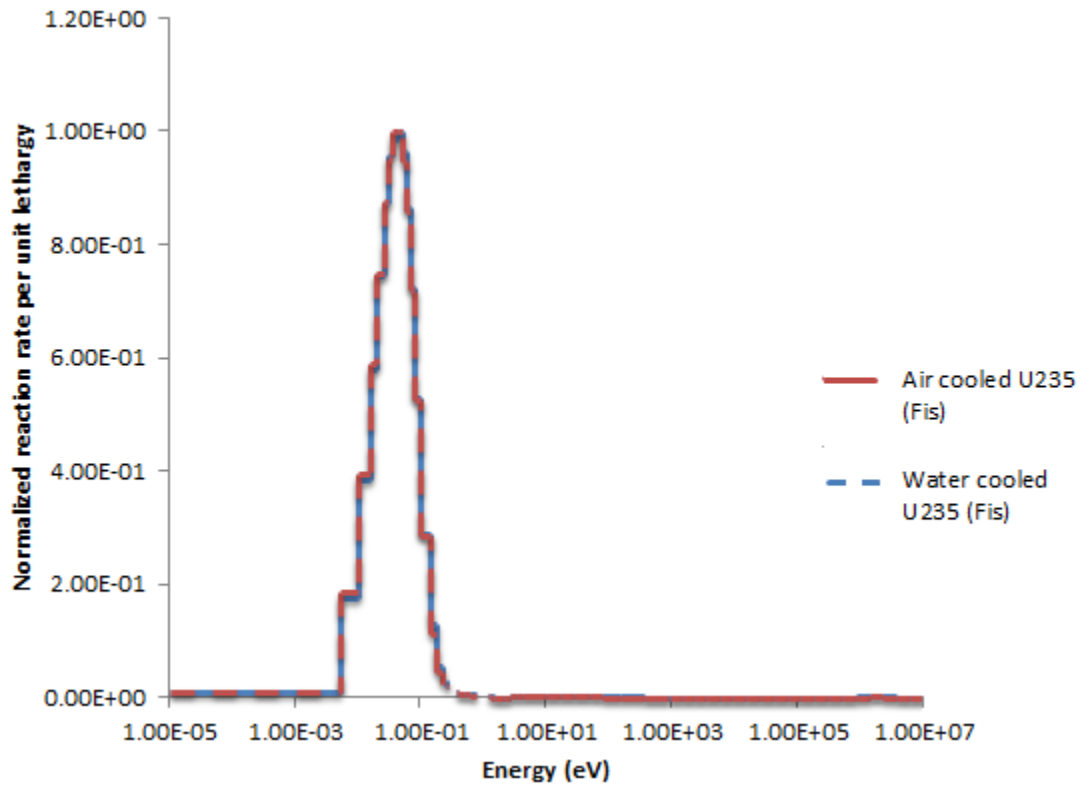


Figure 36: Full core ^{235}U fission rates of the cases where the K0 site with air cooled (Th,Pu) O_2 bundle and K0 site with water cooled (Th,Pu) O_2 bundle

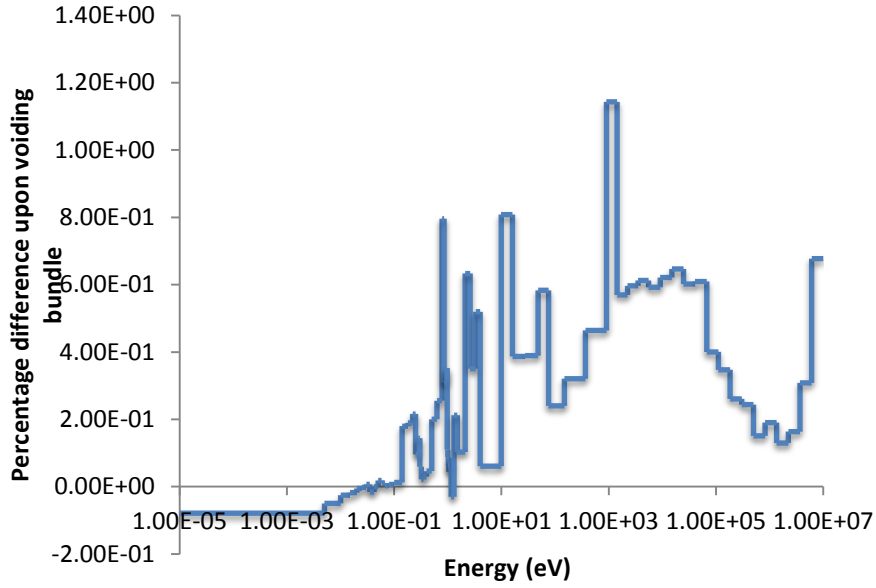


Figure 37: Group wise relative differences plot of ^{235}U fission rates - where the relative difference = $(\text{RX}_{\text{void}} - \text{RX}_{\text{cooled}}) / \text{RX}_{\text{cooled}}$

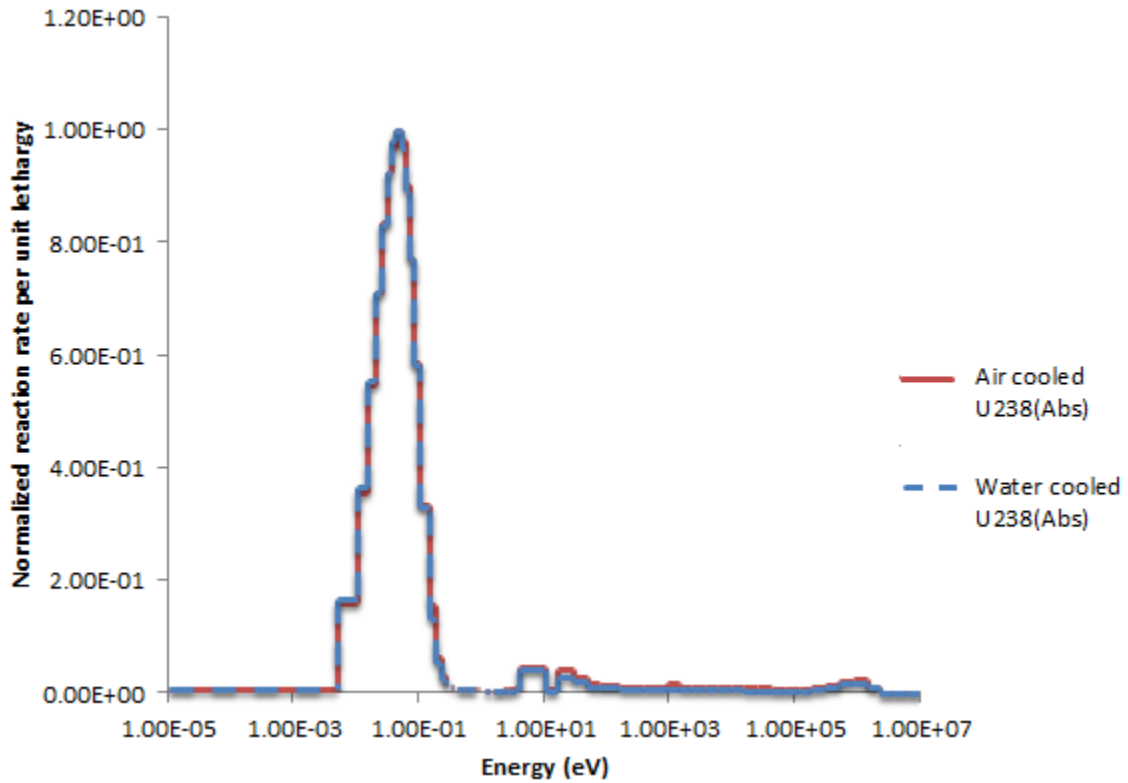


Figure 38: Full core ^{238}U absorption rates of the cases where the K0 site with air cooled $(\text{Th,Pu})\text{O}_2$ bundle and K0 site with water cooled $(\text{Th,Pu})\text{O}_2$ bundle

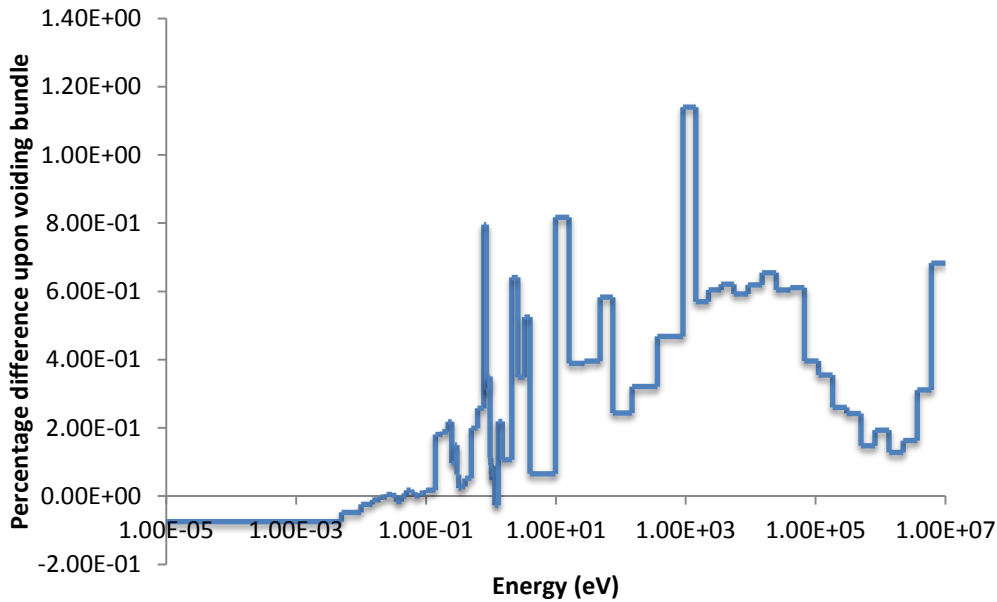


Figure 39: Group wise relative differences plot of ^{238}U absorption rates - where the relative difference = $(RX_{\text{void}} - RX_{\text{cooled}}) / RX_{\text{cooled}}$

^{239}Pu fission rates were also analyzed to study the rates occurring inside the bundle. ^{239}Pu plays a major role in perturbing the reactivity of the core and thus its reaction rates upon voiding are significant. Contrary to the uranium isotopes, ^{239}Pu fission shows a consistent decrease upon voiding the bundle. The slight decrease in the thermal region corresponds to the fact that there are less thermal neutrons available in the bundle, due to the coolant's moderating role. Furthermore, the leakage of fast neutrons produced upon fission inside the bundle, in addition to the missing coolant which leads to less neutrons slowing down to the epithermal region results in a decrease in ^{239}Pu in the epithermal and fast regions of the spectrum.

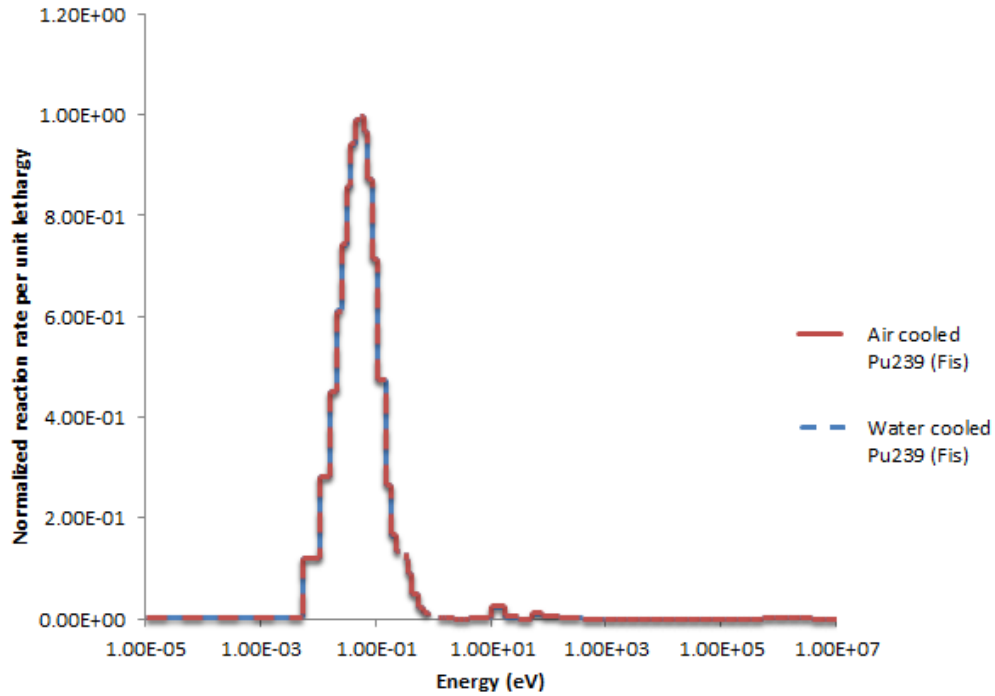


Figure 40: Full core ^{239}Pu fission rates of the cases where the K0 site with air cooled $(\text{Th},\text{Pu})\text{O}_2$ bundle and K0 site with water cooled $(\text{Th},\text{Pu})\text{O}_2$ bundle

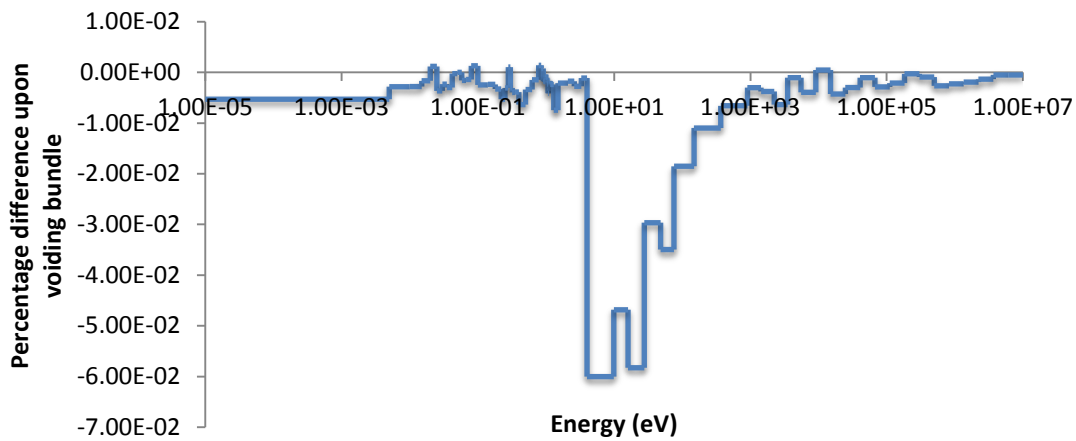


Figure 41: Group wise relative differences plot of ^{239}Pu fission

The absorption rate of ^{232}Th , another isotope present in the central bundle, displays a similar pattern as ^{239}Pu . The leakage of fast neutrons and lack of a coolant to thermalize the fast neutrons created in the bundle leads to a general decrease in ^{232}Th throughout the energy spectrum. The largest decreases are observed in the epithermal and fast regions.

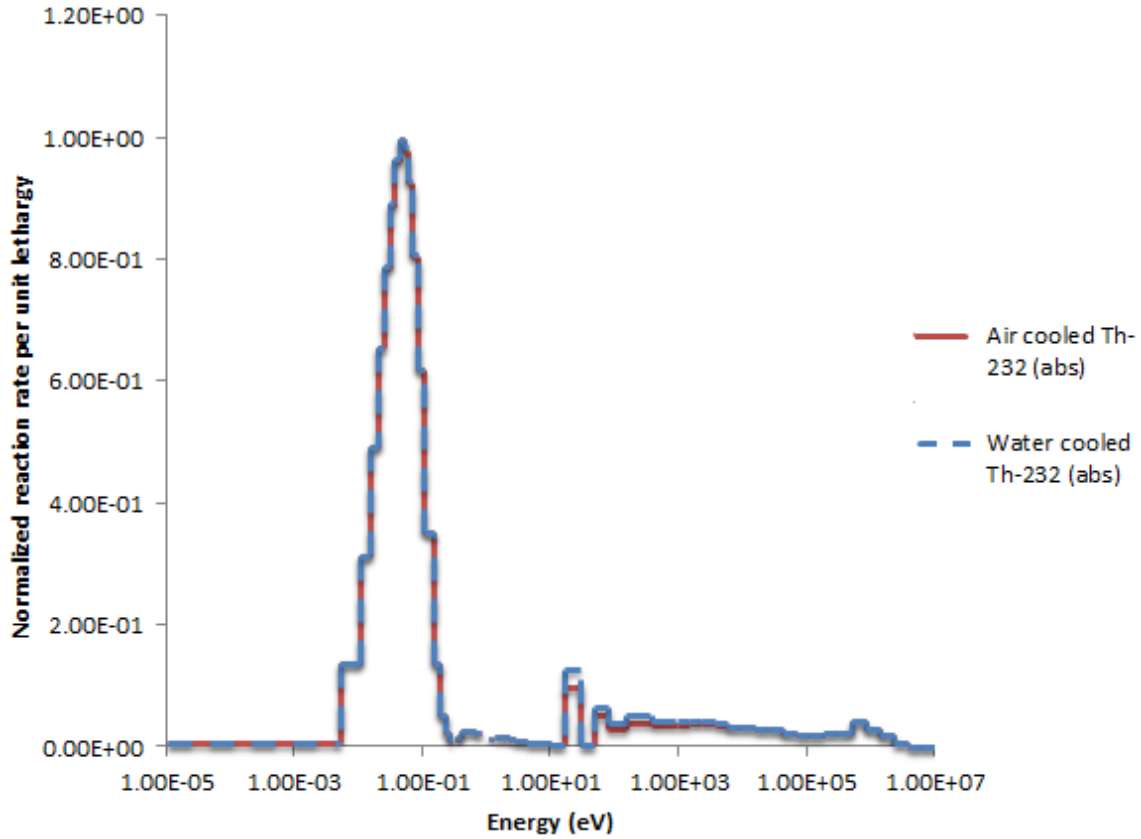


Figure 42: Full core ^{232}Th absorption rates

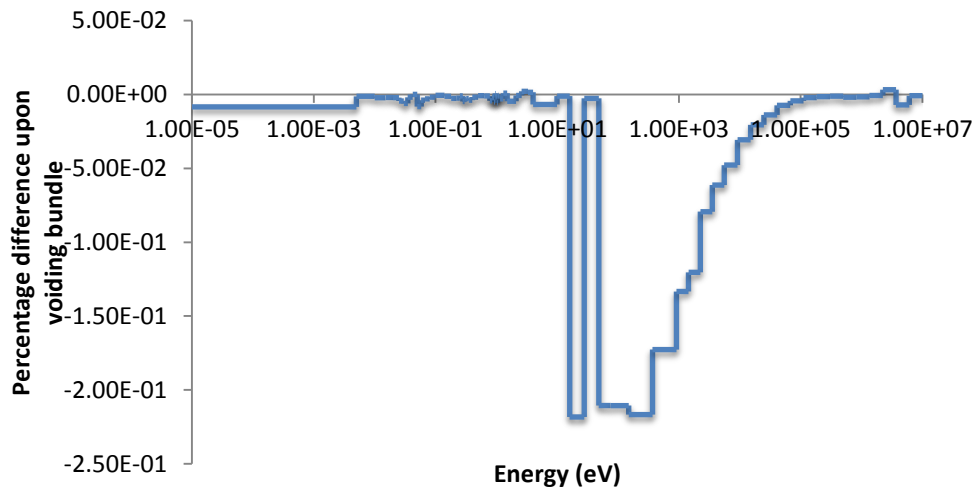


Figure 43: Group wise relative differences plot of ^{232}Th fission

The group-wise reaction rates were subsequently integrated over the energy groups to determine the total reaction rates in the full core as shown in equation (2.66). As observed in table 19, the reaction rates of the isotopes in the central bundle of the core decreased upon voiding. Upon voiding, the leakage in the central bundle increases and

thus leading to this decrease in rates. However, the isotopes outside the bundle are all observed to have an increase in their rates. This is again due to the increased flux in the regions outside the bundle, upon voiding.

Furthermore, the reaction rates were used to calculate the ratio of leakage of the full core in the case of the voided central bundle and case of the cooled bundle.

$$k_{eff} = \frac{\nu\Sigma_f\Phi}{\Sigma_a\Phi + L} \quad (2.68)$$

$$k_{inf} = \frac{\nu\Sigma_f\Phi}{\Sigma_a\Phi} \quad (2.69)$$

Rearranging (2.68) gives:

$$\frac{\nu\Sigma_f\Phi}{k_{eff}} - \Sigma_a\Phi = L \quad (2.70)$$

Substituting (2.69):

$$\nu\Sigma_f\Phi \left(\frac{1}{k_{eff}} - \frac{1}{k_{inf}} \right) = L \quad (2.71)$$

Thus

$$\frac{L_v}{L_c} = \frac{\nu_v\Sigma_{f,v}\Phi_v \left(\frac{1}{k_{eff,v}} - \frac{1}{k_{inf,v}} \right)}{\nu_c\Sigma_{f,c}\Phi_c \left(\frac{1}{k_{eff,c}} - \frac{1}{k_{eff,c}} \right)} = 1.7706 \quad (2.72)$$

It is observed that voiding the central bundle in the full core leads to an increase in total integrated leakage by a factor of 1.77. This was expected as the population of fast neutrons in the core increases upon voiding the central bundle. Having a longer mean free path relative to thermal neutrons, an increase in fast neutrons also leads to an increase in leakage.

| Reaction | Total rate-cooled | Total rate-void | Relative diff. | Thermal rate-cooled | Thermal rate-void | Relative diff. |
|------------------------------------|-------------------|-----------------|----------------|---------------------|-------------------|----------------|
| $^{239}\text{Pu}(\text{Fis})$ | 2.14E-06 | 2.03E-06 | -5.08E-02 | 5.91E-12 | 5.61E-12 | -5.14E-02 |
| $^{239}\text{Pu}(\text{n},\gamma)$ | 3.92E-08 | 3.73E-08 | -5.07E-02 | 2.91E-12 | 2.75E-12 | -5.26E-02 |
| $^{232}\text{Th}(\text{Fis})$ | 1.04E-05 | 9.82E-06 | -5.22E-02 | - | - | - |
| $^{232}\text{Th}(\text{n},\gamma)$ | 5.29E-06 | 5.02E-06 | -5.09E-02 | 3.25E-12 | 3.08E-12 | -5.14E-02 |
| $^{238}\text{Pu}(\text{Fis})$ | 4.22E-09 | 4.01E-09 | -4.90E-02 | 1.37E-16 | 1.30E-16 | -5.13E-02 |
| $^{238}\text{Pu}(\text{n},\gamma)$ | 1.30E-10 | 1.23E-10 | -5.25E-02 | 4.11E-15 | 3.90E-15 | -5.17E-02 |
| $^{240}\text{Pu}(\text{Fis})$ | 4.55E-07 | 4.32E-07 | -5.15E-02 | 1.56E-16 | 1.48E-16 | -5.23E-02 |
| $^{240}\text{Pu}(\text{n},\gamma)$ | 1.51E-08 | 1.42E-08 | -5.33E-02 | 6.87E-13 | 6.52E-13 | -5.23E-02 |
| $^{241}\text{Pu}(\text{Fis})$ | 7.17E-08 | 6.79E-08 | -5.17E-02 | 2.59E-13 | 2.46E-13 | -5.18E-02 |
| $^{241}\text{Pu}(\text{n},\gamma)$ | 3.46E-09 | 3.28E-09 | -5.11E-02 | 8.82E-14 | 8.36E-14 | -5.21E-02 |
| $^{242}\text{Pu}(\text{Fis})$ | 1.01E-08 | 9.63E-09 | -5.05E-02 | 1.08E-19 | 1.03E-19 | -5.27E-02 |
| $^{242}\text{Pu}(\text{n},\gamma)$ | 4.71E-10 | 4.47E-10 | -5.08E-02 | 8.29E-16 | 7.86E-16 | -5.22E-02 |
| $^{235}\text{U}(\text{Fis})$ | 5.45E-06 | 7.06E-06 | 2.95E-01 | 3.64E-11 | 3.81E-11 | 4.60E-02 |
| $^{235}\text{U}(\text{n},\gamma)$ | 2.19E-07 | 2.68E-07 | 2.24E-01 | 6.18E-12 | 6.47E-12 | 4.73E-02 |
| $^{238}\text{U}(\text{Fis})$ | 2.88E-04 | 3.82E-04 | 3.28E-01 | 2.53E-16 | 2.66E-16 | 5.25E-02 |
| $^{238}\text{U}(\text{n},\gamma)$ | 2.24E-05 | 2.71E-05 | 2.11E-01 | 2.57E-11 | 2.70E-11 | 5.04E-02 |
| $^1\text{H}(\text{n},\gamma)$ | 8.49E-09 | 1.01E-09 | -8.82E-01 | 5.56E-12 | 4.84E-12 | -1.29E-01 |
| $^{16}\text{O}(\text{n},\gamma)$ | 1.26E-10 | 1.18E-10 | -6.93E-02 | 5.27E-13 | 5.00E-13 | -5.17E-02 |
| Sum fission | 3.06E-04 | 4.01E-04 | 3.12E-01 | 4.26E-11 | 4.40E-11 | 3.19E-02 |
| Sum absorption | 2.79E-05 | 3.24E-05 | 1.61E-01 | 4.49E-11 | 4.54E-11 | 1.08E-02 |

Table 19: Integrated reaction rates in the fuel, ^1H and ^{16}O in the full core

2.4.6 Moderator and Graphite Homogenization

Unlike the ZEEP rod lattice and the (Th,Pu)O₂ bundle, the Flux-Volume Weighting (FVW) method was used to calculate homogenized graphite and moderator libraries in the 2D full-core model. This is due to the high levels of homogeneity existent in the final output geometry containing the homogenized and condensed nuclear data. This

uniformity in the output geometry of the moderator and graphite allows for the preservation of the reaction rates while using the FVW method.

Using the same energy meshing as the previous two lattices, all regions containing the graphite reflector were homogenized and subsequently condensed to 2 energy groups.

The same procedure was used for the reactor moderator. The energy limits chosen for the libraries were identical to those used for the ZEEP and bundle lattices to keep the consistency necessary for later usage in DONJON.

Chapter 3

ZED-2 Full Core Diffusion Calculations

3.1 ZED-2 Critical Facility

The full reactor core was modeled after an experiment done in the ZED-2 critical facility in Chalk River Laboratories operated by AECL. Using the Bruce pattern, five 36-element bundles containing (Th,Pu)O₂ fuel were designed. Each bundle consisted of concentric aluminum pressure and calandria tubes separated by an air gap. The 5 bundles were subsequently stacked vertically in the center of the reactor core, the K0 site, using an aluminum central support tube, which was a snug fit in the holes of their end plates. Each bundle had an approximate height of 49.7 cm and the 5 bundle-stack was suspended with a distance of 15.1 cm from the Calandria floor.

The K0 site was surrounded by 63 ZEEP rods, arranged in a non-uniform hexagonal array with an NRU pitch of 19.685 cm. Each ZEEP rod contained natural uranium metal cylinders with a diameter of 3.25 cm stacked in a 2S aluminum alloy. With a height of 285 cm, each ZEEP rod was also suspended with a distance of 15.1 cm from the Calandria floor.

The facility's criticality was controlled by its moderator height. Thus, the four distinct experiments conducted were characterized by a specific critical moderator height. The following table represents the four experiments and their respective critical moderator heights:

| K0 site | Critical moderator height (m) |
|--|-------------------------------|
| 1. ZEEP rod | 2.524 |
| 2. No fuel | 2.654 |
| 3. Light-water cooled (Th,Pu)O ₂ bundle | 2.562 |
| 4. Air-cooled (Th,Pu)O ₂ bundle | 2.439 |

Table 20: The recorded critical moderator heights for the four full core experiments

The DONJON models representing each specific experiment were designed to calculate the k_{eff} and flux values at each experiment's respective critical moderator height.

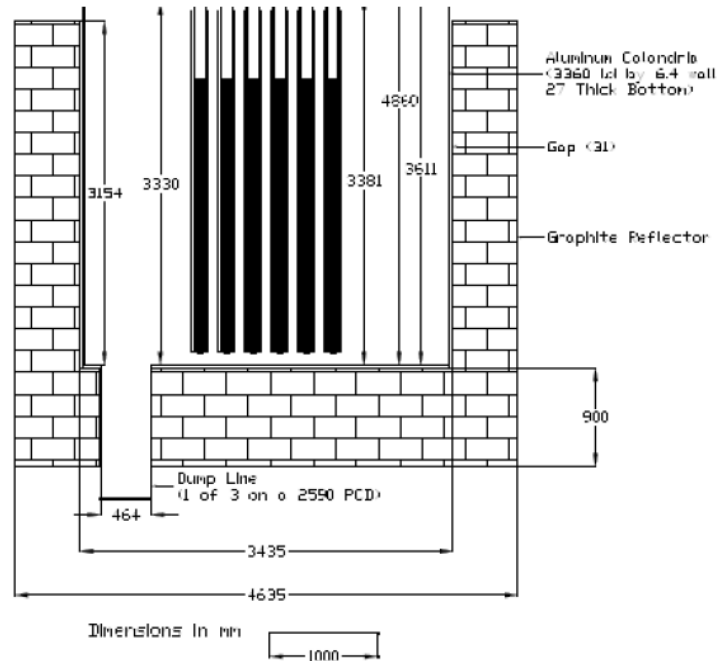


Figure 44: Cross section of the ZED-2 reactor

3.2 Macroscopic Cross Section Library

As discussed in chapter 2, the **COMPO:** module in DRAGON was used to create six distinct macroscopic cross section libraries. Subsequently, the **CRE:** module in DONJON is used to create one extended macroscopic cross section library containing the nuclear properties recovered from the 6 COMPO objects:

1. Homogenized macroscopic cross sections of the full ZEEP rod lattice
2. Homogenized macroscopic cross sections of the non-moderated ZEEP lattice
3. Homogenized macroscopic cross sections of the ZEEP rod lattice moderator
4. Super-homogenized macroscopic cross sections of the (Th,Pu)O₂ bundle lattice
5. Homogenized macroscopic cross sections of the graphite reflector
6. Homogenized macroscopic cross sections of the reactor moderator

3.3 K0 Site - ZEEP Rod

The effects of the various choices made, while choosing the optimal ZEEP rod lattice configurations, will be examined on the full core 3D model of the facility. Case 1 was only composed of ZEEP rods as a fuel source; the (Th,Pu)O₂ bundle configurations will be examined in the later sections.

3.3.1 Carcel Lattice Geometry

The Carcel geometry was determined as the most optimal choice for the geometry of the lattice, and further discretized to achieve more accurate results. The effects of the discretization were further observed in the macroscopic cross section libraries created from the lattice model, and subsequently led to different k_{eff} values in the full core 3D model as well.

| Discretization | Lattice k_{∞} (DRAGON) | DRAGON Computation Time (minutes) | Full-core k_{eff} (DONJON) |
|----------------|----------------------------------|---|--|
| 0 | 1.217555 | ~2 | 1.0329878330 |
| 10x 10 | 1.208477 | ~5 | 1.0092490912 |
| 15x 15 | 1.207128 | ~15 | 1.0059305429 |
| 20x 20 | 1.206517 | ~35 | 1.0043908358 |
| 25x 25 | 1.206193 | ~55 | 1.0035655499 |
| 30x 30 | 1.205981 | ~80 | 1.0030494928 |
| 35x 35 | 1.20584 | ~130 | 1.0026820898 |
| 50x 50 | 1.205651 | ~195 | 1.0021961927 |

Table 21: Effects of spatial discretization in a Carcel geometry on the lattice k_{∞} , computation time, and full core k_{eff}

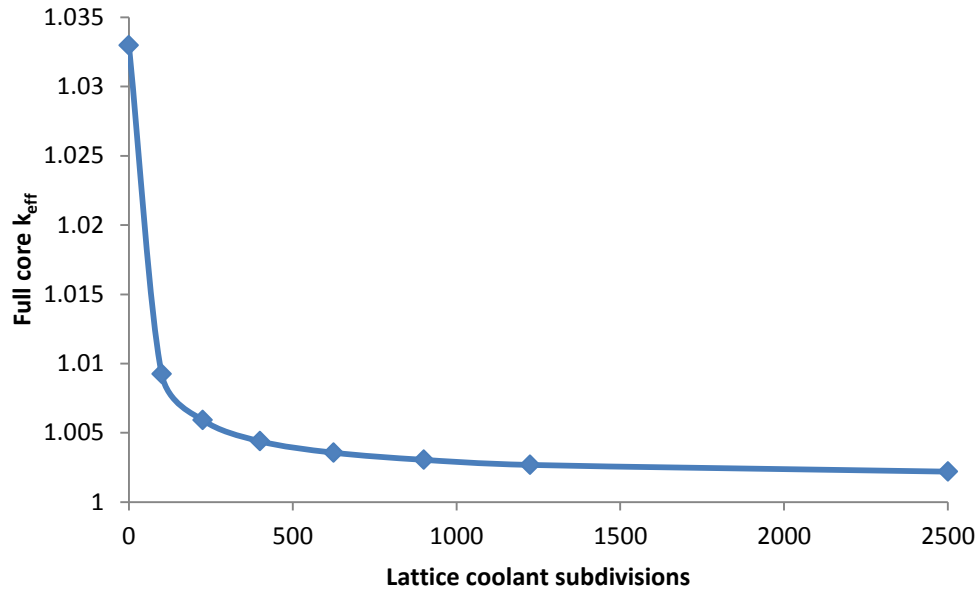


Figure 45: Spatial convergence of the Carcel geometry discretization

A spatial convergence is observed as the nodalization of the ZEEP rod lattice is increased to 25x 25, creating 625 subdivisions in the Carcel geometry. However, achieving the extensive accuracy of 3.56 mk for the full core calculation is computationally expensive. With almost 1 hour of computation time in DRAGON, the question of accuracy versus time efficiency becomes of importance. Thus, even though it was established, in the previous chapter, that the Carcel geometry is the model that is physically closest to reality, the annular model is also analyzed for its accuracy since it has proven to have much smaller computation times.

3.3.2 Annular Lattice Geometry

The annular geometry was tested in a similar manner as discussed in the previous chapter. The optimal fuel region discretization was initially determined by keeping the moderator subdivisions constant, and subsequently, the moderator discretization was examined while keeping the previously determined fuel discretization constant. The respective macroscopic cross section libraries were created for each case and the full core k_{eff} was then calculated.

As observed from table 20 the fuel region discretization did not yield a great change in the lattice k_{∞} , and its changes to the full core k_{eff} appear to have converged at 6 annular

subdivisions. The moderator subdivisions, however, led to significant changes to the k_{∞} of the lattice and the full core, and this was expected since the moderator's area in the lattice is much larger than the fuel's. Both lattice k_{∞} and full core k_{eff} values appear to have converged at approximately 18 subdivisions, not changing by more than 0.2 mk and 0.7 mk respectively as subdivisions increase to 42. However, due to the very small computation time the increase in nodalization continued to attain even higher accuracies. Upon comparing the two geometries, Carcel and annular, the optimal choice is determined to be the annular choice. This is due to the fact that the difference between the highest level of discretization for the Carcel geometry (50x 50), and that of the

| Using a constant moderator subdivision of 0 | | | | |
|--|------------------------|-------------------------------|-----------------------|-------------------------------------|
| Fuel subdivisions: | Number of subdivisions | Lattice k_{∞} (DRAGON) | DRAGON Comp. time (m) | Full core k_{eff} (DONJON) |
| | 1 | 1.218460 | <1 | 1.0353044271 |
| | 4 | 1.217500 | <1 | 1.0332068205 |
| | 6 | 1.217367 | <1 | 1.0329166651 |
| Using a constant fuel subdivision of 6 | | | | |
| Moderator subdivisions: | Number of subdivisions | Lattice k_{∞} (DRAGON) | DRAGON Comp. time (m) | Full core k_{eff} (DONJON) |
| | 1 | 1.217367 | <1 | 1.0329166651 |
| | 2 | 1.214391 | <1 | 1.0250188112 |
| | 4 | 1.210086 | <1 | 1.0137987137 |
| | 8 | 1.207434 | <1 | 1.0066967010 |
| | 18 | 1.206387 | <1 | 1.0037469864 |
| | 26 | 1.206332 | <1 | 1.0032868385 |
| | 30 | 1.206200 | <1 | 1.0031859875 |
| | 36 | 1.206167 | <1 | 1.0030915737 |
| | 42 | 1.206148 | <1 | 1.0030288696 |

Table 22: Effects of spatial discretization in an annular geometry on the lattice k_{∞} , computation time, and full core k_{eff}

annular geometry (6 fuel and 42 moderator subdivisions) only differ by 0.832 mk in reactivity. However, the annular geometry yields results approximately 3 hours faster than the Carcel one, and thus the annular geometry with 6 fuel and 42 moderator subdivisions is determined to be the best choice in the full core modeling of the ZED-2 facility.

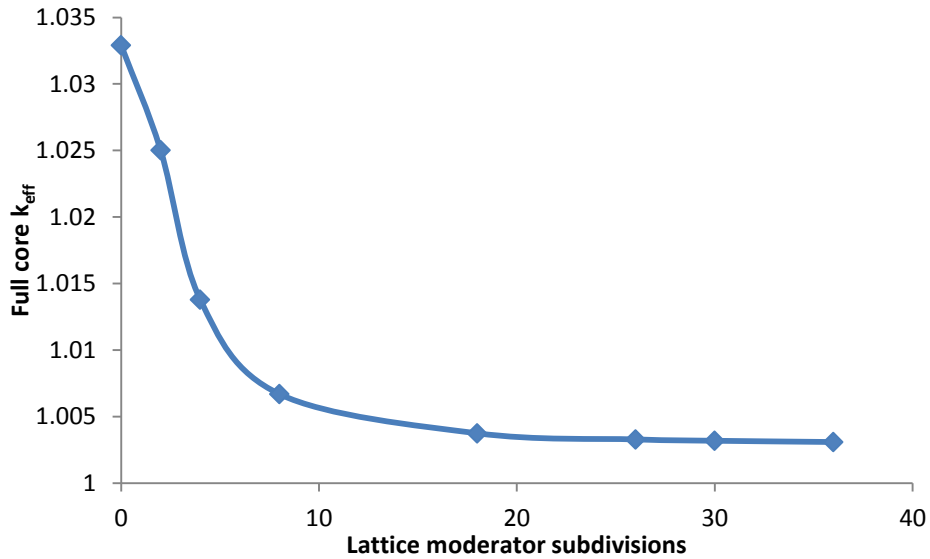


Figure 46: Spatial convergence of the annular geometry discretization

3.3.3 Self-shielding

As discussed in chapter 2.2.5, two options in the SHI: module in DRAGON were examined for their accuracy. The Livolant-Jeanpierre (LJ) normalization scheme is found to be less accurate for CANDU reactors, and thus the default option in DRAGON is not to apply the aforementioned scheme. However, due to the differences between a typical CANDU lattice and a ZED-2 lattice, both options (with LJ normalization scheme and without it) were examined to determine the more accurate choice.

| Normalization scheme | Lattice k_{∞} (DRAGON) | Full core k_{eff} (DONJON) |
|------------------------|-------------------------------|------------------------------|
| Livolant-Jeanpierre | 1.215659 | 1.0075160265 |
| No Livolant-Jeanpierre | 1.206167 | 1.0030288696 |

Table 23: Effects of the Livolant-Jeanpierre normalization on the lattice k_{∞} and full core k_{eff}

As observed, the self-shielding option plays a large role in the lattice and the full core criticality. However, a difference of almost 10 mk in lattice reactivity and 4 mk in full core reactivity illustrates that, much like CANDU lattices and reactors, the LJ normalization scheme proves to be less accurate for the ZED-2 facility.

3.3.4 Full-core Discretization

Upon determining the optimal ZEEP lattice configuration, the effects of discretization were observed in the full core. It is important to note that the results presented in the previous section were achieved using a 3x 3 splitting pattern on the x-y plane and various splitting on the z-axis to ensure a height of approximately 10 cm for all the bottom graphite boxes and an approximate height of 1 cm for all the boxes in the core.

| x-y plane discretization | Full-core k_{eff} |
|--------------------------|----------------------------|
| 1x 1 (no splitting) | 9.96375E-01 |
| 2x 2 | 1.00142 |
| 3x 3 | 1.00303 |
| 4x 4 | 1.00378 |
| 5x 5 | 1.00415 |
| 6x 6 | 1.00442 |
| 7x 7 | 1.00450 |

Table 24: Effect of full core x-y discretization on the k_{eff}

As observed from table 24 and figure 47, spatial convergence is seen at the 6x 6 x-y plane discretization. A difference of 0.1 mk between 6x 6 and 7x 7 proves any higher discretization unnecessary and inefficient.

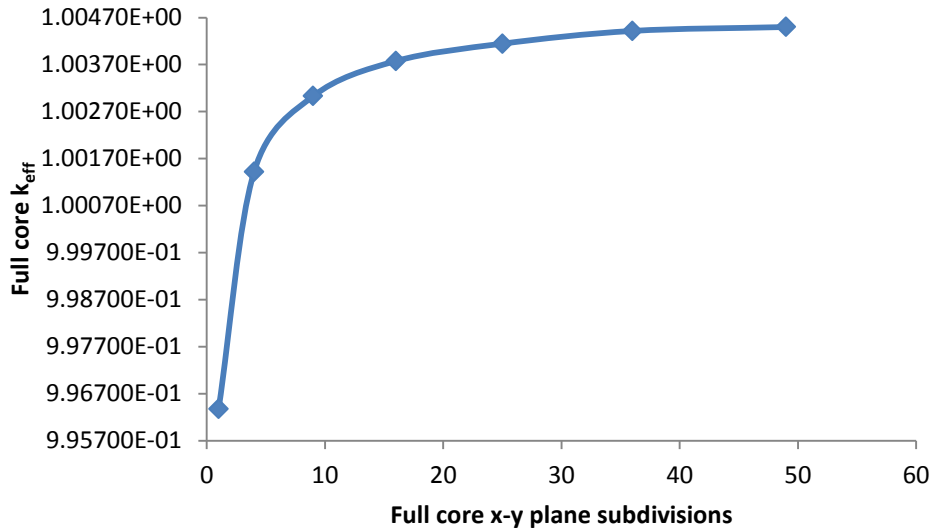


Figure 47: Spatial convergence in the full core

3.4 K0 Site - No Fuel

Similar to the previous case, ZEEP rods are the only fuel source within the core in this model. The difference in this case is that the K0 site does not contain any fuel. Due to having such a minor difference, the optimal lattice configurations chosen for the previous case will also apply in this case as well. Hence, using the specific critical height recorded for this experiment, 2.654 m, the DONJON model was constructed and the following table summarizes the results.

3.4.1 Full Core Discretization

Similar to the ZEEP case, the spatial discretization of the core was increased until a convergence pattern was observed, and the changes in the core reactivity became too small to sacrifice the extra computation time.

As observed from table 23 and figure 48, a converging pattern is observed after the 3x 3 subdivision. Furthermore, a difference of 0.03 mk between 6x 6 and 7x 7 discretization points to the fact that spatial convergence is achieved and any extra subdivisions will yield insignificant changes to the reactivity of the core.

| x-y plane discretization | Full-core k_{eff} |
|--------------------------|----------------------------|
| 1x 1 (no splitting) | 9.9472767115E-01 |
| 2x 2 | 9.9763441086E-01 |
| 3x 3 | 9.9856561422E-01 |
| 4x 4 | 9.9894422293E-01 |
| 5x 5 | 9.9910885096E-01 |
| 6x 6 | 9.9916986952E-01 |
| 7x 7 | 9.9920021040E-01 |

Table 25: Effects of full core x-y discretization on k_{eff}

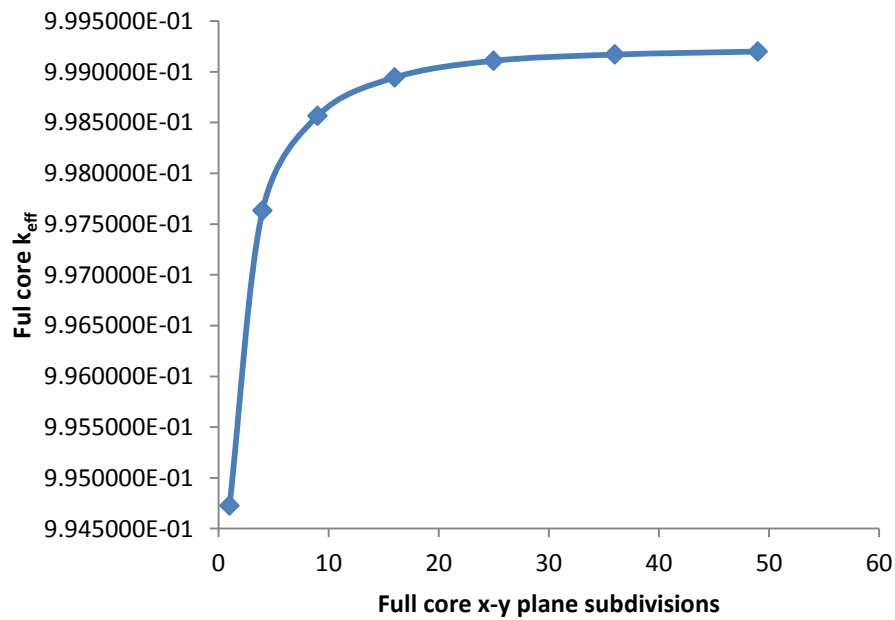


Figure 48: Spatial convergence in the full core

3.5 K0 Site – Water Cooled Bundle

3.5.1 Carcel Lattice Geometry

Due to the higher accuracy of the Carcel lattice, the nuclear data determined by DRAGON using this geometry was initially examined in DONJON. Three distinct discretization patterns were analyzed in the following order: annular coolant subdivisions, annular moderator subdivisions, and Cartesian lattice subdivisions. The

optimal number of subdivisions was determined for each type of discretization individually while keeping the others constant.

As observed in table 26, the effects of bundle discretization are not as significant as the ZEEP lattice discretization. This is justified by the fact that the full core is composed of 63 ZEEP rods and only 5 bundles. The bundle lattice discretization makes a total of approximately 3 mk difference in reactivity yet over 1 hour of difference in computation time.

The computation time does not increase drastically as annular subdivisions increase, however as soon as the Cartesian splitting is introduced there is a significant

| Using a constant moderator subdivision of 0 | | | | |
|--|------------------------|-------------------------------|-----------------------|-------------------------------------|
| Annular coolant subdivisions: | Number of subdivisions | Lattice k_{∞} (DRAGON) | DRAGON Comp. time (m) | Full core k_{eff} (DONJON) |
| | 1 | 1.055567 | 7 | 1.0051063299 |
| | 3 | 1.051913 | 7 | 1.0046843290 |
| | 6 | 1.037104 | 7 | 1.0030808449 |
| Using a constant coolant subdivision of 6 | | | | |
| Annular moderator subdivisions: | Number of subdivisions | Lattice k_{∞} (DRAGON) | DRAGON Comp. time (m) | Full core k_{eff} (DONJON) |
| | 1 | 1.037104 | 10 | 1.0030808449 |
| | 2 | 1.037105 | 10 | 1.0030813327 |
| | 5 | 1.037106 | 10 | 1.0030814409 |
| Using a constant coolant and moderator subdiv. of 6 and 5 | | | | |
| Cartesian subdivisions: | Number of subdivisions | Lattice k_{∞} (DRAGON) | DRAGON comp. time (m) | Full core k_{eff} (DONJON) |
| | 3x 3 | 1.037145 | 45 | 1.0029354095 |
| | 6x 6 | 1.037068 | 65 | 1.0029139519 |
| | 8x 8 | 1.035347 | 80 | 1.0027393103 |

Table 26: Effects of various discretization schemes in the Carcel geometry of the (Th,Pu)O₂ bundle

increase in computational time. The difference in reactivity once the Cartesian discretization is introduced is not very significant (< 0.3 mk). Thus, it is determined that if the Carcel geometry was to be used for the bundle lattice, the configuration with 6 annular coolant subdivisions, 5 annular moderator subdivisions, and no further Cartesian subdivisions would be the most optimal geometry.

3.5.2 Annular Lattice Geometry

Much like the ZEEP lattice, discussed in the previous chapter, the (Th,Pu)O₂ bundle lattice was initially modeled using the Carcel geometry due to its higher accuracy. However, the annular geometry was also analyzed for a comparison in its accuracy and computation time.

The coolant was initially subdivided while keeping the moderator subdivisions constant, and upon finding the optimal coolant nodalization, the moderator was discretized. The following table illustrates the k_{∞} of the bundle lattice alongside with the k_{eff} of the full core upon increasing the subdivisions in the (Th,Pu)O₂ bundle lattice.

It is interesting to note that, contrasting the ZEEP lattice, the majority of the reactivity change due to spatial discretization is due to the coolant subdivisions. This is because the bundle lattice has a much smaller volume of moderator than the ZEEP lattice, and thus the effects of its coolant discretization are much more emphasized.

The full core reactivity calculated in DONJON, using the annular bundle lattice data determined in DRAGON, appears to converge at approximately 3.01 mk. The k_{∞} achieved with the optimal Carcel bundle lattice geometry is 3.08 mk; while more accurate results were calculated with the Carcel geometry, the significant increase in its computation time deemed the extra accuracy inefficient. With approximately similar computation times between the Carcel bundle lattice geometry and the annular geometry, the annular geometry was found to be slightly more accurate. Therefore, the final geometry chosen for the (Th,Pu)O₂ bundle lattice is the annular geometry with 6 coolant and 10 moderator subdivisions.

| Using a constant moderator subdivision of 0 | | | | |
|--|------------------------|-------------------------------|-----------------------|-------------------------------------|
| Coolant subdivisions: | Number of subdivisions | Lattice k_{∞} (DRAGON) | DRAGON Comp. time (m) | Full core k_{eff} (DONJON) |
| | 1 | 1.055360 | <5 | 1.0051102638 |
| | 3 | 1.051727 | <5 | 1.0046858788 |
| | 5 | 1.038709 | <5 | 1.0032633543 |
| | 6 | 1.036927 | <5 | 1.0030812025 |
| Using a constant coolant subdivision of 6 | | | | |
| Moderator subdivisions: | Number of subdivisions | Lattice k_{∞} (DRAGON) | DRAGON Comp. time (m) | Full core k_{eff} (DONJON) |
| | 1 | 1.036927 | <5 | 1.0329166651 |
| | 2 | 1.037054 | <5 | 1.0030357838 |
| | 4 | 1.037261 | <5 | 1.0030158758 |
| | 6 | 1.037339 | <5 | 1.0030125380 |
| | 8 | 1.037374 | <5 | 1.0030115843 |
| | 10 | 1.037392 | <5 | 1.0030109882 |

Table 27: Effects of discretization in the annular geometry of the (Th,Pu)O₂ bundle

3.5.3 Full Core Discretization

The full core was also further discretized to ensure a spatial convergence. The following table illustrates the results.

| x-y plane discretization | Full-core k_{eff} |
|--------------------------|----------------------------|
| 1x 1 (no splitting) | 9.9775332212E-01 |
| 2x 2 | 1.0017950535 |
| 3x 3 | 1.0030109882 |
| 4x 4 | 1.0035067797 |
| 5x 5 | 1.0037012131 |
| 6x 6 | 1.0038523674 |
| 7x 7 | 1.0039054232 |

Table 28: Effects of full core x-y discretization on k_{eff}

3.6 K0 Site – Air Cooled Bundle

The full core case containing an air cooled (Th,Pu)O₂ bundle in the center is composed of the same fuel as the previously mentioned water cooled bundle. Hence, the optimal bundle lattice configuration chosen for the previous case (the annular geometry containing 6 and 10 subdivisions in its coolant and moderator respectively) will be used in this case as well.

| x-y plane discretization | Full-core k_{eff} |
|--------------------------|----------------------------|
| 1x 1 (no splitting) | 9.9481678009E-01 |
| 2x 2 | 1.0003066063 |
| 3x 3 | 1.0020912886 |
| 4x 4 | 1.0025769472 |
| 5x 5 | 1.0028507710 |
| 6x 6 | 1.0030174210 |
| 7x 7 | 1.0032054232 |

Table 29: Effects of full core x-y discretization on k_{eff}

3.7 Overview

Using the optimal configurations for the (Th,Pu)O₂ bundle and the ZEEP rod lattices, the four full core cases were simulated at their respective critical heights. The following table summarizes the k_{eff} values of the four cases.

| K0 site | Critical moderator height (m) | k_{eff} |
|---|----------------------------------|------------------|
| 1. ZEEP rod | 2.524 | 1.0045021330 |
| 2. No fuel | 2.654 | 0.9992002104 |
| 3. Light-water cooled (Th,Pu)O ₂ bundle | 2.562 | 1.0039054232 |
| 4. Air-cooled (Th,Pu)O ₂ bundle | 2.439 | 1.0032054232 |

Table 30: Summary of the four cases k_{eff} values

Conclusion

In this paper, deterministic methods were used to simulate four benchmark experiments done in the ZED-2 critical facility using (Th,Pu)O₂ fuel. The k_{eff} results of the DRAGON/DONJON code coupling were compared to the experimental data gathered by AECL [7]. These results illustrated the successful simulation of the 3D full core critical cases, modeled at specific moderator heights measured in the experiment. Furthermore, the full core 2D S/U results of the DRAGON/SUSD3D code coupling were compared to the full core 3D S/U results gathered by TSUNAMI, a code within the SCALE6 package [31]. This comparison showed less than a $\pm 5\%$ difference between the two code's results in the sensitivity calculations, and slightly higher discrepancies in the uncertainty calculations.

DRAGON was initially used to model a ZEEP rod unit lattice. To optimize the modeling, two geometries were analyzed, the annular geometry and the Cartesian (Carcel) geometry. Spatial convergence was reached at 25x 25 Cartesian subdivisions in the Carcel geometry, taking approximately 1 hour of computation time and leading to a k_{∞} of 1.2062; while convergence was reached after less than 1 minute for the annular model, using 6 annular subdivisions in the fuel region and 42 annular subdivisions in the moderator region and leading to a k_{∞} of 1.2061. The difference in k_{∞} values was considered negligible and the annular model was chosen due to its much faster computation time.

Subsequently, the ZEEP model was used to calculate the direct and adjoint flux values for the infinite lattice. These values were then used in SUS3D to perform the S/U analysis. The lattice k_{∞} was found to be most sensitive to perturbations in ^{235}U $\bar{\nu}$ and fission cross sections, however the largest source of uncertainty in the k_{∞} was due to the cross section uncertainty from ^{238}U (n, γ), which contributed 83% to the total variance. This was found to be due to the large uncertainty present in the ^{238}U (n, γ) cross section. The second DRAGON model was the (Th,Pu)O₂ bundle unit cell. Similar to the ZEEP lattice, the bundle lattice was found to have a much faster computation time in an annular geometry, with negligible differences in k_{∞} between the annular and Cartesian cases. To observe the effects of voiding in the bundle, a second bundle lattice cell was modeled

without any coolant present. The CVR was measured to be -31.17 mk, and upon observing the flux spectra of the cooled and voided bundle, it was clear that the coolant was also acting as a moderator in the bundle lattice cell. The reaction rates were subsequently determined, showing the fact that the fission rates in the bundle lattice had decreased significantly overall, and especially in the sensitive thermal region.

The S/U analysis of the (Th,Pu)O₂ bundle showed a decrease in the ²³⁹Pu $\bar{\nu}$ value upon voiding. Since the sensitivity coefficient is directly proportional to the $\bar{\nu}$ value, the decrease in the sensitivity coefficient illustrates a general decrease in the ²³⁹Pu $\bar{\nu}$ in the bundle upon voiding. Furthermore, an increase was seen in the integrated sensitivities of all fissile isotope's fission and capture sensitivity coefficients upon voiding. The uncertainties of the reactions followed equation (1.64) as the top 5 reactions with the highest contribution to uncertainty were also the most sensitive reactions to the lattice k_{∞} . The last DRAGON model was the simulation of the full core in 2 dimensions. The exact core geometry was replicated and two self-shielding methods were applied to the library: the sub-geometry self-shielding method and the global-geometry self-shielding method. The sub-geometry method was based on the core being segregated into 6 2x 2 geometries, self-shielding calculations were then carried out for each sub-geometry until the library was corrected for self-shielding and used in the full core calculations. The method was proven to be relatively fast computationally, however there existed a ± 3 mk difference in the results; a discrepancy which was too significant to neglect.

The global-geometry method was done by modeling the full core using reflective boundary conditions and subsequently correcting the library for self-shielding effects. The corrected library was then used to perform the full core calculations under void boundary conditions to evaluate the direct/adjoint flux and k_{eff} calculations.

Upon the analysis of the k_{eff} values of the four cases it was observed that the case where an air cooled bundle is inserted in the K0 site has the highest k_{eff} value. The CVR of the full core in 2D was determined to be approximately +8.00 mk, a dramatic increase from the (Th,Pu)O₂ infinite lattice CVR. The reaction rates in the core were then analyzed, which led to the conclusion that there was an overall increase in the fission rate of the fuel upon voiding the core. This was explained by the fact that without the coolant, there is an increase in the resonance escape probability of the neutrons in the bundle. With a

higher leakage rate as well, more neutrons leak out of the bundle and enter the surrounding moderator, where they thermalize and cause fission in the ZEEP rods. The 2D full core S/U results obtained by DRAGON/SUSD3D were then compared to the 3D full core S/U results obtained by TSUNAMI. The integrated sensitivities between the two methods showed a small difference of $\pm 5\%$ however the discrepancies between the uncertainty values were more significant. Since the integrated sensitivities had such a close agreement, it is concluded that the difference in the uncertainties is due to the covariance matrices of the two methods. Covariance matrices are difficult to produce and currently contain a large amount of discrepancy between different libraries. This leads to differences in uncertainty analyses and leads to less accurate measurements. Thus, more effort is needed to produce coherent and consistent covariance matrices to avoid such discrepancies.

Furthermore, it is concluded here that 2D S/U analysis would be sufficient for such experiments if the ^2H data is not significant. Due to the differences in the critical moderator height, the ^2H data is expected to differ between 2D S/U analysis and 3D S/U analysis, but all other isotopes illustrated little differences between the two geometric dimensions.

Every optimized DRAGON lattice and the 2D core produced a set of homogenized and condensed nuclear data in 2 energy groups. The ZEEP rod lattice data, alongside with the full core data produced the homogenized and condensed cross sections using the FVW method, chosen due to the homogeneity of the output geometry. The (Th,Pu) O_2 bundle lattice produced the homogenized data using the SPH method, since the final geometry was not fully homogeneous and contained moderator and fuel in it. These nuclear data were then used in the diffusion code, DONJON, to determine the full core 3D k_{eff} values. Characterized by specific critical moderator heights, the four experiments illustrated close to critical reactivity values (a maximum of ~ 4.5 mk) and proved the successful simulation of the benchmark experiments using the DRAGON/DONJON codes.

This research shows the ability to achieve accurate results using the free and open source IST codes DRAGON and DONJON, and obtain precise sensitivity and uncertainty data by coupling DRAGON with the modified version of SUD3D. Furthermore, 2D S/U analysis of the full core proves to have the needed accuracy for isotopes in the core except those that depend directly on the height of the core (in this case, ^2H existing in the

varying critical moderator height). Finally, this paper illustrates the important need for more consistency and accuracy between covariance matrices obtained for different libraries.

Future projects in this field include coupling DONJON and SUS3D to be able to obtain S/U data for large 3D geometries. This would require calculating sensitivity coefficients based on first order perturbation theory applied to the diffusion equation and propagating the uncertainties through the condensation and homogenization of the cross sections.

Furthermore, the results of this paper could be cross checked with results obtained by different libraries and covariance matrices, to further prove that the discrepancies in the results were due to the library uncertainties and not modeling errors.

Bibliography

- [1] M.S. Milgram, "Once-Through thorium cycles in CANDU reactors," AECL, Chalk River, Ontario, Technical AECL-7516, 1982.
- [2] R. T. Jones, "Experiments performed in ZED-2 in support of the irradiation of (Th, Pu)O₂ fuel (BDL-422) in NRU," Atomic Energy of Canada Limited, Chalk River Nuclear Laboratories, Technical report January 1984.
- [3] T. Zhu, "Sensitivity and uncertainty analysis of (Th,Pu)O₂ benchmark experiments in ZED-2 using TSUNAMI," McMaster University, Hamilton, MASC thesis 2011.
- [4] Division of Nuclear Fuel Cycle and Waste Technology, IAEA, "Thorium fuel cycle - Potential benefits and challenges," Vienna, Austria, May 2005.
- [5] P.S.W. Chan, R.J. Ellis, G.R. Dyck, J.D. Sullivan, P. Taylor, R.T. Jones P.G. Boczar, "A fresh look at thorium fuel cycles in CANDU reactors," in *11th Pacific Basin Nuclear Conference*, Banff, 1998.
- [6] D.J. Cameron, "A review of the potential for actinide redistribution in CANDU thorium cycle fuels," AECL, Pinawa, Manitoba, Technical AECL-5962, 1978.
- [7] M. Milgram, "Things you've always wanted to know about the physics of thorium-fuelled CANDU's," AECL, Chalk River, Ontario, Technical AECL- 5558, 1975.
- [8] S. Banjeree, A.D. Lane, H. Tamm, J.I. Veeder, S.R. Hatcher, "Thorium cycle in heavy water moderated pressure tube (CANDU) reactors," AECL, Pinawa, Manitoba, Technical report AECL-5398, 1976.
- [9] A. Hébert and R. Roy G. Marleau, "A User Guide for DRAGON 3.05F," Department de genie physique, École Polytechnique de Montréal, Montréal, Technical report 2008.
- [10] A. Hébert, R. Roy and J. Koclas E. Varin, "A User Guide for DONJON Version 3.01," Département de génie physique, École Polytechnique de Montréal, Montréal, Technical report 2005.
- [11] I. Kodeli, "Cross-section Data Uncertainty and how such Information is Used in Fusion Analysis," in *International Conference Nuclear Energy in Central Europe '99*, Portoroz, Slovenia, 1999, pp. 637 - 644.

- [12] J.W. Meadows and Y. Watanabe D. L. Smith, "Covariances for Measured Activation and Fission Ratios Data," in *IAEA Specialists' Meeting on Covariance Methods and Practices in the Field of Nuclear Data*, Rome, 1980.
- [13] P. Sabouri and A. Bidaud, "Critical Safety Assessment Using SUS3D and DRAGON," in *Nuclear Energy for New Europe 2011*, Bovec, Slovenia, 2011, pp. 322.1-322.8.
- [14] A. Hébert, *Applied Reactor Physics*. Montreal, Canada: Presses Internationales Polytechnique, 2009.
- [15] G. Marleau, "DRAGON Theory Manual- Part 1: Collision Probability Calculations," École Polytechnique de Montréal, Montréal, Technical report October 2001.
- [16] D. Rochman et al., "Nuclear data uncertainty propagation: Perturbation vs. Monte Carlo," *Annals of Nuclear Energy*, vol. 38, pp. 942-952, February 2011.
- [17] A. Hébert and G. Marleau, "Generalization of the Stamm'ler Method for the Self-Shielding of Resonant Isotopes in Arbitrary Geometries," *Nuclear Science and Engineering*, vol. 108, pp. 230-239, July 1991.
- [18] F. Jeanpierre M. Livolant, "Autoprotection des resonances dans les reacteurs nucleaires- Application aux isotopes lourds," Commissariat a l'Energie Atomique, Paris, Technical CEA-R-4533, 1974.
- [19] Y. Kitamura, Y. Yamane and A. Yamamoto, "Cell homogenization methods of pin-by-pin core calculations tested in slab geometry," *Annals of Nuclear Engineering*, vol. 31, pp. 824-847, 2004.
- [20] M. Ionescu-Bujor and D. G. Cacuci, "Sensitivity and Uncertainty Analysis, Data Assimilation, and Predictive Best-Estimate Model Calibration," in *Handbook of Nuclear Engineering*, Dan Gabriel Cacuci, Ed. Germany: Springer, 2010, ch. 17, pp. 1916-1950.
- [21] G. Aliberti et al., "Nuclear data sensitivity, uncertainty and target accuracy assessment for future nuclear systems," *Annals of Nuclear Energy*, vol. 33, no. 8, pp. 700-733, May 2006.
- [22] T. Courau and G. Marleau, "Perturbation Theory for Lattice Cell Calculations," *Nuclear Science and Engineering*, vol. 143, pp. 19-32, January 2003.

- [23] W. Stacey Jr., "Variational Estimates of Reactivity Worths and Reaction Rate Ratios in Critical Nuclear Reactors," *Nuclear Science and Engineering*, vol. 48, pp. 444-458, April 1972.
- [24] T. Courau and G. Marleau, "Calculating adjoint fluxes in the code DRAGON using the Collision Probability method," in *PHYSOR 2000 International Topical Meeting, Advances in Reactor Physics and Mathematics and Computation into the Next Millennium*, Pittsburgh, PA, 2000.
- [25] M. Sarroto, A. Stankovskiy, G. Van den Eynde and T. Sugawara, "Nuclear data sensitivity/uncertainty analysis for XT-ADS," *Annals of Nuclear Energy*, vol. 38, pp. 1098-1108, June 2011.
- [26] F. Fayers, P. Kemshell J. Askew, "A general description of the lattice code WIMS," *Journal of the British Nuclear Energy Society*, vol. 5, pp. 564-585, 1966.
- [27] R.E. Macfarlane, "TRANSX-CTR: A code for interfacing MATXS cross section libraries to nuclear transport codes for fusion system analysis," Los Alamos National Laboratory, Los Alamos, Technical report LA-9863-MS, 1984.
- [28] J. Donnelly, "WIMS-CRNL- A user manual for the chalk river version of WIMS," AECL, Chalk River, Technical report AECL-8955, 1986.
- [29] F. Jeanpierre, A. Kavenoky, M. Livolant, H. Lorain A. Hoffman, "APOLLO : Code multigroupe de résolution de l'équation du transport pour les neutrons thermiques et rapides," Commissariat à l'Énergie Atomique, Paris, Note CEA-N-1610, 1973.
- [30] I. Kodeli, "SUSD3D- A multi-dimensional, discrete ordinates based cross section sensitivity and uncertainty code," OECD/NEA Data Bank, Paris, Technical report 2008.
- [31] D.W. Muir and R.E. MacFarlane, "The NJOY nuclear data processing system, VOLUME IV: the ERRORR and COVR modules," Los Alamos National Laboratory, Los Alamos, Manual LA-9303-M, 1965.
- [32] J. Le Mer, "Simulations du comportement neutronique des REP en utilisant les codes DRAGON et DONJON," Département de génie physique, École Polytechnique de Montréal, Montréal, MASC Thesis 2007.
- [33] M. Salvatores G. Palmiotti, "Proposal for Nuclear Data Covariance Matrix," Nuclear

Energy Agency Report JEFDOC 1063 Rev.1, 2005.

[34] L.J. Hamilton J.J. Duderstadt, *Nuclear Reactor Analysis*. Ann Arbor, Michigan, United States of America: John Wiley & Sons, 1976.

[35] M.L. Williams, "Perturbation Theory for Nuclear Reactor Analysis," in *Handbook of nuclear reactor calculations: Vols I-III*, Yigal Ronen, Ed. West Palm Beach, Florida, United States of America: CRC Press, 1988, ch. Vol III, pp. 63-188.